Transverse momentum broadening of high-energy partons from 3D lattice EQCD simulations

Schlusser, Niels

(2020)

Transverse momentum broadening of high-energy partons from 3D lattice EQCD simulations

Berechnung der transversalen Impulsverbreiterung hochenergetischer Partonen mit Hilfe von dreidimensionalen Gitter-EQCD-Simulationen

Zur Erlangung des Grades eines Doktors der Naturwissenschaften (Dr. rer. nat.)
genehmigte Dissertation von Niels Vincent Lucca Schlusser aus Mannheim
Tag der Einreichung: 15.6.2020, Tag der Prüfung: 20.7.2020

1. Gutachten: Prof. Ph. D. Guy D. Moore
2. Gutachten: Prof. Dr. rer. nat. Jens Braun
Darmstadt

TECHNISCHE UNIVERSITÄT DARMSTADT

Fachbereich Physik
Institut für Kernphysik
Theoriezentrum - AG Moore

Transverse momentum broadening of high-energy partons from 3D lattice EQCD simulations
Berechnung der transversalen Impulsverbreiterung hochenergetischer Partonen mit Hilfe von dreidimensionalen Gitter-EQCD-Simulationen

Doctoral thesis by Niels Vincent Lucca Schlusser

1. Review: Prof. Ph. D. Guy D. Moore
2. Review: Prof. Dr. rer. nat. Jens Braun

Date of submission: 15.6.2020
Date of thesis defense: 20.7.2020

Darmstadt

“Alles Vergängliche ist nur ein Gleichnis”
J. W. von Goethe: *Faust. Der Tragödie zweiter Teil*

Erklärungen laut Promotionsordnung

§8 Abs. 1 lit. c PromO

Ich versichere hiermit, dass die elektronische Version meiner Dissertation mit der schriftlichen Version übereinstimmt.

§8 Abs. 1 lit. d PromO

Ich versichere hiermit, dass zu einem vorherigen Zeitpunkt noch keine Promotion versucht wurde. In diesem Fall sind nähere Angaben über Zeitpunkt, Hochschule, Dissertationsthema und Ergebnis dieses Versuchs mitzuteilen.

§9 Abs. 1 PromO

Ich versichere hiermit, dass die vorliegende Dissertation selbstständig und nur unter Verwendung der angegebenen Quellen verfasst wurde.

§9 Abs. 2 PromO

Die Arbeit hat bisher noch nicht zu Prüfungszwecken gedient.

Darmstadt, 15.6.2020

N. Schlusser

Abstract

Heavy-ion collision experiments and related theoretical efforts of understanding the strong interaction constitute key endeavors in the modern pursuit of understanding nature. A central field of comparison for experiment and theory are the interactions of high-energy particles with a strongly interacting medium. The transverse momentum distribution of a high-energy particle broadens in crossing that very medium, quantified by the transverse collision kernel, $C(b_\perp)$. It receives dominant infrared corrections which cannot be tackled perturbatively, even at weak coupling. In the present thesis, we calculated this contribution on the lattice in Electrostatic QCD as proposed by Caron-Huot and pioneered by Panero, Rummukainen, and Schäfer. In order to put us into the position of extrapolating the discretization errors away, we developed a procedure to entirely remove discretization errors linear in the lattice spacing. Our data, provided at four different temperatures, render the common approximations of $C(b_\perp)$ redundant.

Zusammenfassung

Streuexperimente mit Schwerionen und damit verbundene theoretische Bemühungen, die starke Wechselwirkung zu verstehen, stellen zentrale Forschungsunterfangen im modernen Streben nach Verständnis der Natur dar. Ein wichtiges Feld, auf dem Experiment mit Theorie verglichen werden kann, ist die Wechselwirkung eines hochenergetischen Teilchens mit einem stark wechselwirkenden Medium. Die Verteilung des transversalen Impulses hochenergetischer Teilchen verbreitert sich, während diese ebenjenes Medium durchqueren, quantifiziert durch den transversalen Kollisionskern $C(b_\perp)$. Er erhält dominante Infrarot-Korrekturen, deren Berechnung auch bei kleiner Kopplungskonstante nicht störungstheoretisch angegangen werden kann. In der vorliegenden Arbeit wurde dieser Beitrag mit Hilfe von Gittersimulationen in Elektrostatischer QCD berechnet, wie bereits von Caron-Huot vorgeschlagen und von Panero, Rummukainen und Schäfer wegweisend untersucht. Um uns zu erlauben, den Diskretisierungsfehler zu null zu extrapolieren, wurde eine Prozedur entwickelt, die ein vollständiges Beseitigen von Diskretisierungsfehlern linear im Gitterabstand erlaubt. Unsere Daten bei vier verschiedenen Temperaturen machen gebräuchliche Näherungen von $C(b_\perp)$ überflüssig.

Contents

1. Introduction

1.1. The Standard Model: fundamental vs. effective theory

Natural sciences have always pursued finding the most elementary units of matter. An idea that already emerged in ancient Greece were indivisible smallest units, “átomos”. As opposed to today’s perception of atoms as units of chemical elements that has been born in the late 18th century [1], the “atoms” of the Greeks were geometric objects like spheres, cubes and cones. Bernoulli’s kinetic gas theory in 1738 was rooted in the picture that gases were made of small balls flying around and bumping into each other [2]. About 170 years after this progress, it was found by Rutherford that atoms must have a substructure themselves [3]; they consist of a nucleus that makes up almost all of their mass, accumulated in a very small volume, and an electron shell. In a comment to Bohr’s model of an atom [4], Rutherford also hypothesized that the core of a nitrogen atom consists of hydrogen nuclei, the “protons”. Later, he suggested that also electrically uncharged particles, later called “neutrons”, can be found in the nucleus. Protons and neutrons, in turn, consist of quarks and gluons, as it will be discussed in greater detail in the following chapter.

While the negatively charged electrons and the positively charged protons in the nucleus interact via the electromagnetic force, this cannot be the reason for the nuclear constituents holding together; neutrons are electrically uncharged, and protons carry positive charge, so there must be a force that surpasses the electrostatic repulsion of the protons and glues the nuclear constituents together. This is done by the strong interaction. Radioactive decays of nuclei are induced by a third fundamental interaction, the weak nuclear force. These three interactions are theoretically expressed in the Standard Model of Particle Physics. Gravity is the fourth fundamental interaction. However, the nature of its theoretical description differs from the other three ones so fundamentally that they could not be unified in a joint theory of everything to date.

The standard model is an up-to-date compendium of the three former, known fundamental interactions. As such, it is formulated in the framework of Quantum Field Theory (QFT). Forces, for instance the electromagnetic force, are best described as field theories. Physically, a field quantifies how much a test charge would be affected by a particular interaction if it were at a given point in space-time. Loosely speaking, Quantum Field Theories are the promotion of standard, classical field theories to the quantum world, where energies of particles *and* fields appear only in multiples of some fundamental quanta. QFTs also explicitly impose Poincaré-invariance, that is the invariance of physical observations under a constant shift in space-time, a rotation or a transformation into a frame of reference under uniform motion relative to the original one. To give a generic example: the quantized version of electrodynamics is Quantum Electrodynamics (QED). Similarly, one can proceed with the strong and weak nuclear forces. While the former is promoted to Quantum Chromodynamics, a theory that is unambiguous by itself, the latter suffers from bigger conceptual problems. These were finally resolved by the unification of electromagnetic and weak nuclear force into the Glashow-Salam-Weinberg model of the electroweak interaction [5–7]. Iterating this unorthodox step once more promised a full unification of strong and electroweak interaction, but so far, there has not been any experimental evidence for that [8]. Therefore, the standard model consists of two distinct QFTs describing three out of four fundamental interactions, which seems very unsatisfying at first glance.

Every physical theory is just valid on a certain scale. Newtonian gravity, for instance, is not expected to describe atomic physics, but works impressively well for the determination of the motion of planets around our sun. A field theory that is not valid at arbitrary scales, in particular not at arbitrary small length scales, is referred to as an "Effective Field Theory" (EFT). An EFT predicts well what is observed experimentally in a certain window of validity, although we know that at a higher resolution, the theory fails to work. For Newtonian gravity, this is the case at large field strengths, where finally general relativistic effects kick in. In this example, Newtonian gravity is an effective field theory for general relativity, which is more fundamental, as it can predict physics at higher resolutions. However, it is still beneficial to rely on Newtonian gravity in its range of validity, because it is conceptually far simpler and practical calculations are way more feasible than in full general relativity.

In QFT, dealing with the resolution of a theory is formalized by the renormalization group (RG), developed in its contemporary form by Kenneth G. Wilson [9]. The RG also gives a conceptual handle for understanding effective theories that live at lower resolutions, i.e. smaller energy scales, from more fundamental theories. The notion of a "fundamental" theory refers to the fact that no further substructures of their degrees of freedom are

known. “Effective” means we know that the degrees of freedom in that theory are not fundamental, but assumed to be the effective degrees of freedom in the desired range of validity of the effective theory. Just as in the case of Newtonian gravity, these effective field theories often come with huge conceptual advantages. The RG also implies that the standard model itself, the most fundamental, experimentally confirmed theory of all forces except gravity, is an effective field theory. In science history, this is unique: Modern physics admits that the current state-of-the-art theory is not the end of it.

Despite the conceptual issues with the standard model, one should bear in mind that it is tremendously successful. It predicts many observables with pinpoint accuracy, like for example the electron magnetic moment up to ten digits [10, 11]. Other EFTs, for instance chiral perturbation theory, the quark meson model, or EQCD in the context of the present thesis also show astonishing predictivity. Since it has a certain tradition to begin theses in Germany with a quote from Goethe’s Faust, the initial quote of this thesis should highlight the success of effective theories (“Gleichnis”), which allow us to understand everything that surrounds us (“alles Vergängliche”). At the same time, the quote expresses the limitations of today’s theoretical state-of-the-art, always remaining an effective description and not recognizing the fundamental nature of things (“nur ein Gleichnis”).

1.2. What can we learn about QCD from collider experiments?

The youngest part of the standard model is Quantum Chromodynamics (QCD), the QFT of the strong nuclear interaction. In contrast to Quantum Electrodynamics (QED), QCD is a part of the standard model on its own, without being married to another theory. As the name of the strong interaction already suggests, QCD interactions are literally strong, at least at larger length scales than the radius of a proton. This makes QCD a confining theory, it is trapped in length scales below the proton radius, which we do not explore in our everyday life. Nonetheless, the strong interaction makes up for crucial features of matter, as the binding of quarks and gluons to nucleons and the binding of multiple nucleons to nuclei.

If we want to gather insights into how the strong interaction works and how well, if at all, it is described by QCD, we will have to free the QCD degrees of freedom from confinement. We know that this can be well achieved in scattering experiments at particle collider facilities, where a lot of energy can be concentrated in a very small volume. Collider

experiments also deliver important evidence about the other interactions, but these are not subject to this thesis.

Different types of colliders are specialized in exploring different features of a particular interaction. Some colliders smash together comparatively simple particles with just one or a few constituents, like electrons and positrons or protons with each other. In colliding, they produce a shower of new particles and the focus is on determining their properties like electric charge, spin, quark content, and so on. If stable, these particles fly away from the collision spot and appear in the variety of detectors surrounding the intended collision spots at collider facilities. All particles result in different characteristic signals, often one has to combine the signals of several different kinds of detectors in order to identify a given particle. Unstable particles, in turn, decay characteristically into stable ones and can therefore be detected indirectly, as for instance the Higgs boson was detected via its characteristic decays, predominantly into photons and leptons [12].

Other setups use more complicated particles initially, heavy ions with a lot more constituents. These experiments focus more on collective properties of nuclear matter under extreme conditions. For instance, major research efforts, both in theoretical and experimental physics, are put into the determination and prediction of a phase diagram of nuclear matter. A phase diagram contains two types of information: which phases exist, and under which circumstances they are realized. In particular, one hopes to create a bit of nuclear matter from a part of the phase diagram that differs entirely from confined nuclear matter as we know it: the Quark-Gluon-Plasma (QGP). As one can already tell from its name, the QGP consists mainly of quarks and gluons, the fundamental degrees of freedom in nuclei according to Quantum Chromodynamics. Nuclear matter at room temperature features confinement, neither quarks nor gluons can be observed as separate degrees of freedom at length scales that are larger than a proton radius. At much higher temperatures, even exceeding the temperatures in the core of the sun by orders of magnitude, confinement can be overcome and the QGP is created. These conditions can be reached in heavy-ion collision experiments and mimic the state of the early universe shortly after the Big Bang, whose explanation is certainly one of the major goals in the human quest for knowledge.

Proving that this exotic state of matter can in fact be realized, however, is conceptually even more complicated than the indirect detection of a single particle. Finding observables that show a specific behavior hinting towards the former existence of a QGP is highly non-trivial. Nevertheless, the existence of the QGP was indirectly proven via elliptic flow, a quantity that expresses the angular anisotropy of the final decay products' momentum distribution [13, 14]. Other indirect proofs are for instance the decays of the QGP into

two photons [15], or a pair of leptons [16], or the characteristic breakup of bound states of two quarks in the QGP [17].

Once the existence of the QGP was confirmed, new questions arose about the nature of this new, exotic state of matter. It was found experimentally that the QGP is not really a plasma but merely an almost perfect fluid [18–21]. This opened the gate for effective theoretical modeling using hydrodynamics, but some more ingredients for the corresponding calculations were needed: an equation of state that relates the pressure of the QGP to its temperature, the value of the shear viscosity and possibly also higher order transport coefficients just to name a few of them. Neither theoretical predictions from QCD directly nor direct experimental determinations of these "material properties", called "transport properties" in jargon, are trivial, in fact, they have kept big branches of both theoretical and experimental high-energy physics busy for the last three decades, and nobody has succeeded so far.

1.3. Understanding jet modification in QCD plasmas

Another source of experimental evidence for the QGP are so-called "jets". Jets are products of particle collisions, move at (almost) the speed of light, and, for our purpose, participate in the strong interaction. They are not only created in "simpler" collisions like proton-proton or electron-positron, but also in heavy-ion collisions. However, heavy-ion-collisions also produce the Quark-Gluon-Plasma in contrast to the former type of collisions. These two kinds of collision products interact nontrivially with each other. Their interaction can be pictured as the jet being bumped around by the thermally moving medium constituents and eventually leads to a broadening of the transverse momentum distribution of jets. Considering and understanding jet-medium interactions is not only another possible source of confirmation of the existence of the QGP, but also is a transport property of the QGP by itself.

One way of phrasing this property mathematically is the transverse collision kernel $C(\boldsymbol{q}_\perp)$. It measures the probability Γ of a jet to acquire the transverse momentum $q_\perp$ per length t

$$\frac{\mathrm{d}\Gamma}{\mathrm{d}^2 q_\perp \mathrm{d}t} = \frac{C(\boldsymbol{q}_\perp)}{(2\pi)^2}\,, \tag{1.1}$$

where lengths and times t are equivalent because the jet moves at (almost) the speed of light, i.e. the distance covered in time t equals t if the speed of light is set to 1. Another,

equivalent definition is that the transverse collision kernel measures how likely a particle at infite three-momentum $\boldsymbol{p}$ is to acquire transverse momentum $q_\perp$

$$\lim_{p\to\infty} \frac{\mathrm{d}\Gamma(\boldsymbol{p}, \boldsymbol{p}+\boldsymbol{q}_\perp)}{\mathrm{d}^2 q_\perp} = \frac{C(\boldsymbol{q}_\perp)}{(2\pi)^2}\,. \tag{1.2}$$

Strictly speaking, $\boldsymbol{q}_\perp$ is a two-vector in the transverse plane whereas $\boldsymbol{p}$ is a spatial three-vector, which cannot be added rigorously. As a three-vector, $\boldsymbol{p}$ has a momentum along the jet propagation direction p_z. Throughout this thesis, we set the jet velocity to the speed of light, which is true to very good approximation at the energies reached at modern collider facilities. Therefore p_z is infinite for our purposes due to relativistic kinematics, all transverse components of $\boldsymbol{p}$ can be made 0 by an appropriate choice of a coordinate system. In (1.2), $\Gamma(\boldsymbol{p}, \boldsymbol{p}+\boldsymbol{q}_\perp)$ denotes a particle moving at infinite p_z gathering transverse momentum $\boldsymbol{q}_\perp$.

Initial theoretical work about jet-modification was due to Bjorken [22]. Later on Zakharov built up a coherent quantum mechanical picture [23–25]. Specific expressions for $C(\boldsymbol{q}_\perp)$ were firstly found by Aurenche, Gelis, and Zaraket [26] and generalized by Arnold and Xiao [27]. A Fourier transform

$$C(\boldsymbol{q}_\perp) = \int \mathrm{d}^2 b_\perp \, \mathrm{e}^{i\boldsymbol{b}_\perp\cdot\boldsymbol{q}_\perp} C(\boldsymbol{b}_\perp) \tag{1.3}$$

relates $C(\boldsymbol{q}_\perp)$ to its position-space equivalent $C(\boldsymbol{b}_\perp)$. Casalderrey-Solana and Teaney found a way to compute $C(\boldsymbol{b}_\perp)$ in position space from an observable called "Wilson loop" [28]. Their calculation was carried out in $\mathcal{N}=4$ Super Yang-Mills theory, a supersymmetric theory that resembles QCD, but also has fundamental differences. In contrast to QCD, $\mathcal{N}=4$ Super Yang-Mills theory allows the application of holography, a method that maps a strongly coupled supersymmetric Quantum Field Theory in four-dimensional space-time to weakly-coupled gravity in five space-time dimensions. Caron-Huot made this connection of $C(\boldsymbol{q}_\perp)$ or $C(\boldsymbol{b}_\perp)$ to a modified version of the Wilson loop in position space for QCD [29]. Unfortunately, he found that an expansion in powers of the strong coupling g, so-called "perturbation theory", did not work out in his particular case, due to large contributions from the low-momentum region spoiling the convergence of the series. A first, rather qualitative, non-perturbative study of $C(\boldsymbol{b}_\perp)$ was set up by Rummukainen, Panero, and Schäfer [30], directly simulating the corresponding QFT path-integral discretized on a spatial grid. Due to the exploratory nature of this study, no attempt was made of extrapolating away the finite lattice spacing, which is necessary for the complete removal of discretization effects from the result, though.

The goal of the present work is to connect here and deliver more reliable final results for $C(\boldsymbol{b}_\perp)$. Almost all phenomenological calculations rely on the leading-order perturbative expression for $C(\boldsymbol{b}_\perp)$ at most, if not making even cruder approximations. Measuring the transverse momentum distribution of jets, though, one finds considerably less jets at large transverse momentum than naively expected [31]. Furthermore, we know from Caron-Huot's work that neither the leading-order nor the next-to-leading-order in g^2 results for $C(\boldsymbol{b}_\perp)$ can be trusted, so the impact of a complete first-principles prediction of $C(\boldsymbol{b}_\perp)$ on jet phenomenology should be quite drastic. Moreover, $C(\boldsymbol{b}_\perp)$ plays a key role in the perturbative determination of other transport coefficients like the shear viscosity or the thermal photon rate, which both lack convergence even at unexpectedly high temperatures [32, 33], where perturbation theory should work.

The thesis is organized as follows. Chapter 2 lays the theoretical foundations, reviews calculation techniques used in this thesis, and gives the bigger picture around the progress achieved by this thesis. Chap. 3 reviews key achievements in the field of jet-medium interactions of the recent past that prepared the ground for the research which this thesis is subject to, presented Chap. 4 and Chap. 5. The work in the former chapter completes a procedure for numerical error reduction until the key quantity for jet-medium-interactions, $C(\boldsymbol{b}_\perp)$, is computed in the latter chapter. The thesis is closed by concluding remarks in Chap. 6 and an outlook into future research questions raised by this thesis.

In the present work, we use units where Planck's reduced constant, the speed of light in vacuum, and Boltzmann's constant are all set to 1:

$$\hbar = k_\mathrm{B} = c = 1 \tag{1.4}$$

Events in space-time are characterized by a space-time four-vector x^μ. Two of these vectors can be combined to a scalar product using the version of the Minkowski metric with the negative sign in the time component

$$(\eta^{\mu\nu}) = \mathrm{diag}\,(-1, 1, 1, 1)\ . \tag{1.5}$$

According to the Einstein sum convention, indices that occur twice indicate a summation over the respective indices if not stated differently.

2. Theoretical background

This chapter serves as an introduction to three methodological branches of Quantum Chromodynamics (QCD) at whose interface the present work was conducted, lattice QCD, “Effective Field Theories” (EFTs), and kinetic theory.

To start with, we will explain the basic features of Quantum Chromodynamics, the theory of the strong nuclear force in Section 2.1. QCD can be discretized on a space-time lattice and simulated with Monte Carlo methods, as described in Section 2.2. We provide insight into different algorithms that are commonly used for that purpose.

Furthermore, at large temperatures, QCD can be reduced to an effective field theory called “Electrostatic Quantum Chromodynamics” (EQCD), as elaborated in Section 2.3. Aside from perturbative EFT-treatment, it is also possible to solve EQCD on the lattice, just as full QCD.

Transport phenomena like collective hydrodynamic behavior of nuclear matter under extreme conditions or the broadening of high-energetic particles crossing that very state of matter, and a way of theoretically describing them in kinetic theory are discussed in Sections 2.4 and 2.5.

2.1. Continuum Quantum Chromodynamics

The current theoretical understanding of particle physics roots in the “Standard Model of Particle Physics” a theory that combines nearly all fundamental forces. The four fundamental forces are electromagnetism, gravity and the strong and weak nuclear force.

We encounter the former two in everyday life, for instance if we jump off of the earth, ie. use the electromagnetic repulsion between our feet and the ground to overcome the gravitational force between us and the earth for a moment. This already tells us something

about the strength-hierarchy of these two forces: our feet and the ground under them contain comparatively little electric charge, but this amount of charge is sufficient to temporarily overcome the gravitational force of the entire planet on us. Electromagnetism is far stronger in everyday life than gravity.

The latter two are less common in everyday life, they are predominantly found in nuclei, where the weak force allows radioactive decays, and the strong force accounts for the formation of nucleons such as protons and neutrons and eventually binding them together in nuclei.

Three of these four forces, the electromagnetic, strong and weak nuclear force, can be modeled with the help of a class of theories called "Quantum Field Theories" (QFTs). Only gravity still resists against a comprehensive description in the framework of QFTs, although some aspects of gravity can be described using QFTs. The Standard Model of Particle Physics encompasses the former three of the fundamental forces: the theory of electromagnetic and weak nuclear force combined in the Glashow-Salam-Weinberg model [5–7] and the theory of the strong nuclear force, "Quantum Chromodynamics" (QCD).

In the following section, we will give a compendium of the development of QCD and some of its features. More extensive reviews of the standard model in general [34] and QCD in particular [35] exist.

2.1.1. The history of QCD

In the middle of the last century, QFTs were established as the best-suited theoretical language for fundamental physics. This was accompanied by the discovery of a vast amount of new particles in collider experiments in the second half of the last century.

In order to categorize these new particles, Murray Gell-Mann developed the "eightfold way", ordering pions and kaons into a meson octet and singlet [36], and some baryons in a similar fashion, into octet and decuplet, as in Fig. 2.1. Octet, decuplet and singlet are to be understood in the context of a postulated $SU(3)$ symmetry in the space of the quantum numbers isospin, electric charge and strangeness. It was realized later that this symmetry corresponds to an approximate symmetry in quark flavor space. Apart from the electric charge, these quantum numbers were new, it was not yet known that they originate from the strange-quark and approximate interchangeability of up- and down-quarks. Quarks were postulated by Gell-Mann and Zweig as substructures of the known

particles [37], organized in decuplets, octets and singlets. This was the first occurrence of the group $SU(3)$ in elementary particle physics, although not yet as a gauge group.

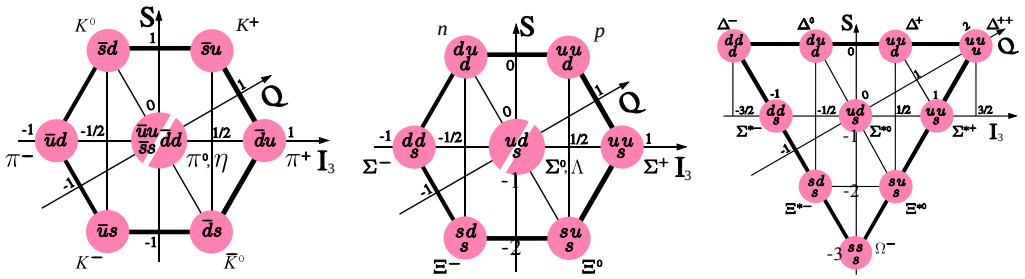

(a) Meson octet and singlet. (b) Spin-$1/2$ baryon octet and singlet. (c) Spin-$3/2$ baryon decuplet.

Figure 2.1.: Organization of new particles in octets and decuplets of the $SU(3)$-flavor symmetry. Pictures taken from [38], released to public domain by the creator.

Another milestone in the development of Quantum Chromodynamics were the Deep Inelastic Scattering (DIS) experiments [39, 40], where electrons (and later muons) were scattered off protons. If protons had been fundamental particles, they would have no substructure and the scattering would have been elastic. However, it was found that the scattering is deeply inelastic, kinetic energy is lost. Therefore, the proton must have a substructure which can be excited and account for the energy loss. Bjorken constructed structure functions of the (point-like) substructure, that he hypothesized in the proton [41]. This substructures were postulated to be the Gell-Mann's and Zweig's quarks and so-called "gluons", that mediate the strong nuclear force between the quarks, leading to the first formulation of QCD on the Lagrangian level in [42], see Eq. (2.1). The intermediators of the force, the gluons, are charged under the gauge group $SU(3)$ and are described by a generalization of gauge theories to non-Abelian gauge groups by Yang and Mills [43].

A decade later, gluons were first measured as planar three-jet events in particle collisions by the TASSO collaboration at the PETRA collider at the "Deutsches Elektronen Synchrotron" (DESY) in Hamburg [44]. As conjectured, the gluon was a spin-1 massless vector boson [45].

2.1.2. Lagrangian formulation of QCD

In the following, we will dive deeper into the theoretical formulation of QCD and its consequences. We do not elaborate on the group theory of the $SU(3)$ non-Abelian Lie-group and its corresponding Lie-algebra. For the details, we refer to the respective literature, e.g. [46] for a thorough introduction and [47] for a comprehensive compendium of specific $SU(3)$-relations.

The action of Quantum Chromodynamics in Euclidean space-time reads [42, 43, 48]

$$\begin{aligned} S^{\mathrm{E}}_{\mathrm{QCD}}\left[\overline{\Psi},\,\Psi,\,A\right] &= S_{\mathrm{F}}\left[\overline{\Psi},\,\Psi,\,A\right] + S_{\mathrm{G}}\left[\overline{\Psi},\,\Psi,\,A\right] \\ &= \int \mathrm{d}^4x\; \overline{\Psi}(x)\left(\gamma_\mu D_\mu + m\right)\Psi(x) + \frac{1}{2g^2}\int \mathrm{d}^4x\; \mathrm{Tr}\, F_{\mu\nu}F_{\mu\nu}\,, \end{aligned} \tag{2.1}$$

where $F_{\mu\nu} = \partial_\mu A_\nu - \partial_\mu A_\nu - f^{abc}A^a_\mu A^b_\nu T^c$ is the field strength tensor, containing the gluon field $A_\mu = A^a_\mu T^a$, charged under $SU(3)$, with T^a the generators and f^{abc} the structure constants of $SU(3)$. Space-time indices μ can take the values $\mu = 1, 2, 3, 4$, where $\mu = 4$ refers to the Euclidean time direction. The strength of the interaction is measured by the strong coupling constant g, the Dirac fermion fields $\overline{\Psi}$ and Ψ have mass m and couple to the gauge field via the covariant derivative $D_\mu = \partial_\mu + iA_\mu$. Note that the fermion fields have an implicit quark flavor index f and the mass is a (diagonal) matrix in flavor space. We omitted these indices for simplicity. Usually, one considers QCD with the three or four lightest quark flavors in the standard model, which have masses below typical scales for QCD and can therefore contribute considerably to the dynamics.

The canonical partition function is given by [48]

$$\mathcal{Z}(T) = \int \mathcal{D}A_\mu\, \mathcal{D}\overline{\Psi}\, \mathcal{D}\Psi\; \mathrm{e}^{-\frac{1}{T}S^{\mathrm{E}}_{\mathrm{QCD}}\left[\overline{\Psi},\,\Psi,\,A\right]}\,, \tag{2.2}$$

with the temperature T marking the inverse extent of the Euclidean time direction. Since the extent of the time direction is finite, we have to specify the boundary conditions. For bosons, as the gauge field A_μ, we impose periodic boundary conditions $A_\mu(0, \boldsymbol{x}) = A_\mu(1/T, \boldsymbol{x})$, whereas fermions fulfill anti-periodic boundary conditions $\Psi(0, \boldsymbol{x}) = -\Psi(1/T, \boldsymbol{x})$ and for $\overline{\Psi}$, respectively. At this point, let us get a short glimpse at what kind of integration we are dealing with and what the integration measure $\mathcal{D}A_\mu$ is. Loosely speaking, $\mathcal{D}A_\mu$ encodes an integration over all A_μ at every point in space-time:

$$\int \mathcal{D}A_\mu = \prod_{\mu,\,x}\left(\int \mathrm{d}A_\mu(x)\right)$$

Continuous space-time consists of uncountably infinite points so this statement is mathematically not exact. For a more rigorous explanation of what that measure is, we ask the reader for patience until Sec. 2.2. In this section, we explain how rendering the number of points to countably infinite or even finite through a space-time lattice makes this measure well-defined. The situation for the fermionic counterparts of (2.3) is conceptually similar, although fermions cannot be represented by functions of common real vectors since they fulfill anti-commutation relations instead of commutation relations. Therefore, we do not explain the details of fermionic path integration and just content ourselves with knowing that it exists.

The canonical partition function relates to the free energy via

$$\mathcal{F}(T) = -T \ln \mathcal{Z}(T)\,, \tag{2.3}$$

from which the other thermodynamic potentials and derived observables can be obtained with the standard methodology of Legendre transformations.

An expectation value of an operator $\hat{\mathcal{O}}$ can be calculated through

$$\langle \hat{\mathcal{O}} \rangle = \frac{1}{\mathcal{Z}(T)} \int \mathcal{D}A_\mu \, \mathcal{D}\overline{\Psi} \, \mathcal{D}\Psi \; \hat{\mathcal{O}} \left[A_\mu,\, \overline{\Psi},\, \Psi\right] \; \mathrm{e}^{-\frac{1}{T} S^{\mathrm{E}}_{\mathrm{QCD}}\left[\overline{\Psi},\, \Psi,\, A\right]}\,. \tag{2.4}$$

At this point, let us stress that the Euclidean-time formalism restricts us to thermal equilibrium. Thermal equilibrium, in turn, is a time-translation invariant state, which means that it behaves equal at all times t and the real-time direction does not play a role here. From the Euclidean-time formalism, it is not always possible to reconstruct Minkowski-time behavior, for instance how a system reacts to a small perturbation off of equilibrium. Unfortunately, this is precisely the scenario which is of particular interest for transport theory, c.f. Sec. 2.4. Eqs. (2.1) and (2.2) can be re-formulated in Minkowski space-time, which makes it inaccessible for the lattice methods presented in Sec. 2.2 since the probability weight becomes complex, implying a severe sign problem in the numerical evaluation of the path integral.

2.1.3. The QCD running coupling

QCD is built in an analogous manner to Quantum Electrodynamics (QED), the quantum theory of the electromagnetic interaction. Positive and negative electric charges are conceptually substituted by color (“chromo-”) charges and anti-charges. Instead of just

one charge, say the positive one, and its anti-charge, the negative one, in QCD there are three charges and their respective anticharges. One can label them red, green, and blue, because the three of them combined give white, i.e. are uncharged. The non-Abelian nature of QCD has some more, drastic consequences, best visualized in the potential between color charge and anti-charge, and the momentum-dependent running coupling of QCD.

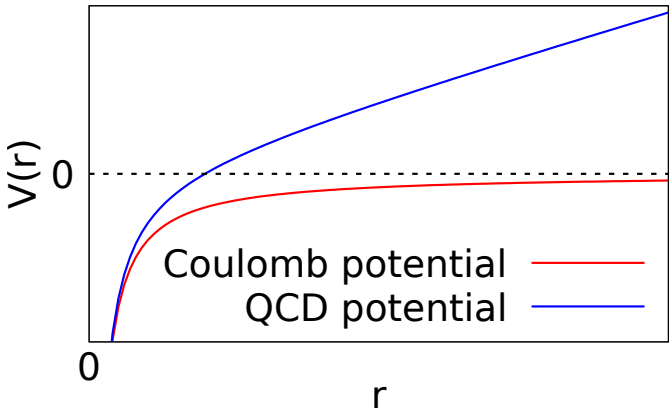

Figure 2.2.: Sketch of the electromagnetic potential as opposed to the potential between a colored object and an object with opposite color charge.

The shape of the potential between two electrically charged particles in QED is very well known, we encounter it frequently in everyday life. Under the assumption of a non-relativistic and small coupling setup, it is to first approximation given by the Coulomb potential, as shown in Fig. 2.2. Crucially, it is proportional to

$$V_{\mathrm{QED}} \propto \frac{1}{r}\,, \tag{2.5}$$

where r is the spatial separation of the two electric charges. If both charges have the same sign, the potential will be positive and the charges will repel each other. If they have opposite sign, the potential will be negative and they will attract each other. A last important feature is that if the two charges are infinitely widely separated, they will not feel each other any more.

The situation for the QCD potential between a color-charge and its anti-charge is partly different. At small separations of the two respective charges, the two potentials in Fig. 2.3

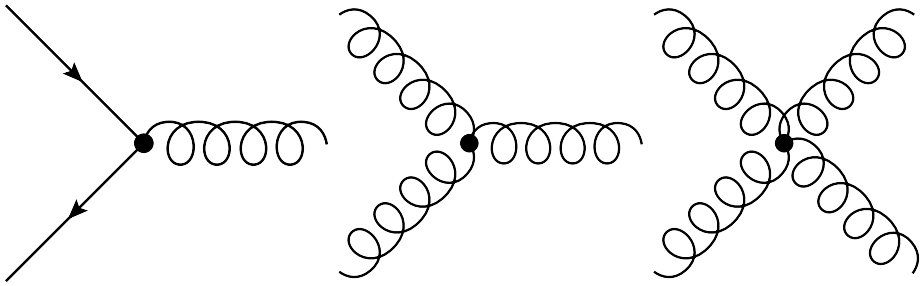

(a) Quark-gluon vertex (b) Three-gluon vertex (c) Four-gluon vertex

Figure 2.3.: QCD interaction vertices. Feynman diagrams made with [49].

are of similar functional form, whereas at growing distance, the QCD potential rises linearly in contrast to the $1/r$ asymptotic behavior of the QED potential. The reason is that the QCD action (2.1) does not only give rise to interactions of gauge bosons with fermions as in Fig. 2.3(a), but also to interactions of the gauge bosons, the gluons, with themselves as displayed in Fig. 2.3(b) and (c). These self-interactions are due to the non-Abelian nature of the gauge fields A_μ, living in the algebra $su(3)$. Since the A_μ-fields do not commute, the field strength tensor $F_{\mu\nu} \equiv -i\,[\mathrm{D}_\mu,\, \mathrm{D}_\nu]$ also has a $[A_\mu,\, A_\nu]$-contribution, which leads to three- and four gluon interactions on the level of the action, in which $F_{\mu\nu}$ appears quadratically.

The self-interaction of the gluons leads to an amplification of the potential energy between a quark and an anti-quark as you increase the distance between them [50, 51]

$$V_{\mathrm{QCD}} = -\frac{4}{3}\,\frac{\alpha_{\mathrm{s}}}{r} + \sigma_{\mathrm{QCD}}\, r\,. \tag{2.6}$$

This relation involves two fundamental quantities: the "string tension" of QCD σ_{QCD} and the strong coupling constant squared $\alpha_{\mathrm{s}} = \frac{g^2}{4\pi}$. Eq. (2.6) also explains why strongly interacting matter cannot be observed in everyday life. If you keep increasing the distance between two color charges, at some point it will be energetically more favorable to create another quark-anti-quark pair between the two initial charges than to keep increasing the potential energy stored in the gauge field. This scale is approximately the radius of a nucleon, beyond which we do not observe color charged objects under normal conditions. Colored objects are trapped to scales below the nucleon radius, they encounter "confinement".

As usual in Quantum Field Theory, the coupling constant depends on the momentum

scale Q. Another famous consequence of the self-interactions of the gluons is the shape of the running coupling of QCD. The one-loop result for $\beta(\mu) = \frac{\partial g}{\partial(\ln \mu)}$ (with a scale μ), and consequently α_s has first been derived by David J. Gross, Frank Wilczek and David Politzer in 1973 [52, 53]

$$\alpha_\mathrm{s}(Q^2) = \frac{12\pi}{(33 - 2N_\mathrm{f})\,\ln(-Q^2/\Lambda^2)}\,, \tag{2.7}$$

where $-Q^2$ is the square of the transferred momentum, Λ is an internal QCD scale [1] and N_f is the number of dynamical quarks. It implies that at large momentum scales $-Q^2$, the coupling diminishes until the theory eventually becomes asymptotically free, i.e. uncoupled in the UV. In turn, the coupling in the infrared, at small momenta and consequently large separation scales, is large, which explains the linear increase of the static quark-anti-quark potential in Fig. 2.2. It also means that infrared physics in QCD, such as thermodynamics, is generically non-perturbative.

Politzer, Wilczek and Gross were jointly awarded the 2004 Nobel prize for their result.

2.1.4. The QCD phase diagram

There are multiple hints that QCD has a nontrivial phase structure. In everyday live, neither quarks nor gluons can be observed separately due to confinement [52, 53]. They only occur in bound states, protons and neutrons, which are the proper degrees of freedom to talk about at normal conditions. We will refer to this phase from now on as the "confined phase".

In the 1970s, it has been conjectured that another phase exists, the "Quark-Gluon Plasma" [56,57]. In this phase, quarks and gluons are the proper degrees of freedom, they occur as separate entities and move around. This can only happen at comparatively small couplings, which correspond to large temperatures according to the QCD running coupling (2.7). Experiments at Brookhaven National Laboratory's Relativistic Heavy Ion Collider (RHIC) firstly confirmed experimentally the existence of the QGP [58–61] and that it indeed features collective phenomena, on which we will elaborate more in Sec. 2.4.

Since then, both experimental evidence from the observation of neutron stars and theoretical evidence from models related to QCD have lead to a conjectured phase diagram in Fig. 2.4 in plane of the temperature T and the quark chemical potential μ. Fig. 2.4

[1] In fact, Λ depends on the regularization scheme. In this work, we will use the $\overline{\mathrm{MS}}$ value from [54], $\Lambda_{\overline{\mathrm{MS}}} = 341 \pm 12$ MeV

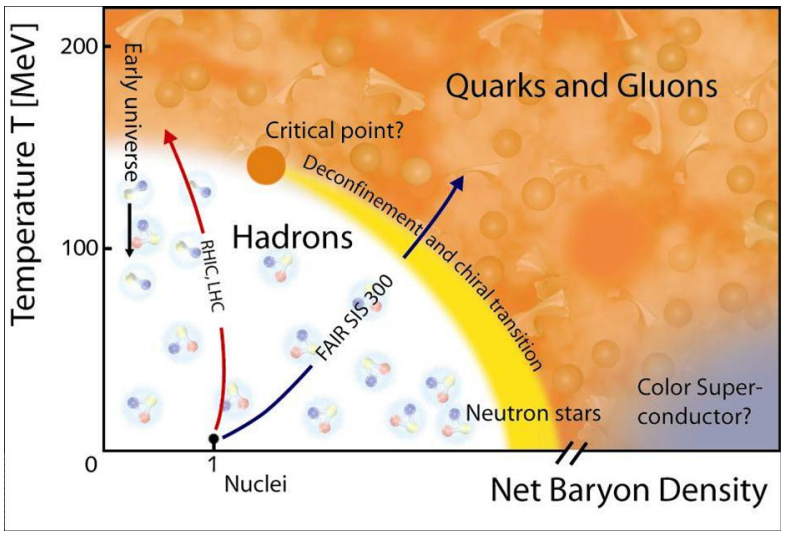

Figure 2.4.: The conjectured T-μ phase diagram of QCD, taken from [55], re-use permitted according to the CC-BY license.

contains even more conjectured phases of nuclear matter, which are experimentally not as well investigated as the two mentioned ones and are of no particular relevance in the context of the present research.

The presence of a non-vanishing μ demands the promotion of the canonical partition function (2.2) to the grand-canonical one. If we had a good order parameter for QCD and if there were a generic way of computing its expectation value in the grand-canonical ensemble, we could theoretically predict the phase diagram of QCD, a phase diagram in the $T - \mu$-plane being equivalent to a common pressure-temperature phase diagram.

Without making too much of a disclosure, it turns out that neither a reliable order parameter nor a generic computation technique exist, which we will elaborate further in Sec. 2.2. For instance, the quark chemical potential μ was firstly implemented in lattice calculations by Frithjof Karsch and Peter Hasenfratz [62]. Unfortunately, it was found that $\mu \neq 0$ calculations on the lattice are prohibited by a severe sign problem due to a complex probability weight, just like in the case of Minkowski time calculations on the lattice as mentioned in subsection 2.1.2. Other methods suffer from comparable conceptual problems. Perturbation theory is only applicable in regions where either T or μ is large, let alone the vicinity of the conjectured phase transition. Functional methods fail to describe gauge theories in a gauge invariant way, and holographic computations produce results in

$\mathcal{N} = 4$ Super-Yang-Mills-Theory which exhibits crucial differences to QCD.

Thankfully, our domain of interest of the phase diagram is the large T, well above the phase transition, and $\mu = 0$ region that is accessible at today's collider facilities like RHIC and the Large Hadron Collider (LHC) at CERN. Therefore, we do not have to deal with all the issues at nonvanishing chemical potential.

2.2. Lattice Quantum Chromodynamics

A wide-spread tool to investigate Quantum Chromodynamics is the discretization on a space-time lattice with a subsequent simulation of the path-integral by Monte-Carlo methods. This is the only known method that directly computes the path integral from first principles. Systematic uncertainties due to the cutoff can be extrapolated to 0, statistical uncertainties can be diminished to an in principle arbitrarily small value, given the respective computation power. Lattice simulations do not rely on any expansion in a small parameter and are therefore ideally suited for exploring physics in the vicinity of the QCD crossover, where correlation lengths diverge and the dynamics is governed by infrared contributions. Beyond such thermodynamic behavior, lattice simulations have found increasing application to QCD transport properties, c.f. Sec. 2.4, over the past two decades.

In the following, we will re-derive the Wilson gauge-action, a discretized version of the continuum gauge action, and discuss some simulation algorithms that found their application in the author's research. Furthermore, we discuss how to extract a sensible statistical error from our Monte-Carlo data and conclude by giving an example for an observable of specific interest in the context of this work.

For further, more extensive discussions of lattice gauge theories and respective simulation techniques we refer to well-established books of Rothe [63] and Gattringer, Lang [48], on whose formulations of the subsequent standard derivations we based the following explanations.

2.2.1. The Wilson discretization of gauge fields

As opposed to other fields of physics, for instance classical mechanics, interacting quantum field theories are in general not analytically solvable, with very few exceptions. Just as in

quantum mechanics, the first natural thing to do is a perturbative expansion, in the case of QCD in the coupling strength g. However, this is only possible at small g (and small thermal occupation numbers of all states, as we will see in Sec. 2.3).

Another idea is to attempt at numerically computing (2.2) in discretized space-time, going back to Kenneth G. Wilson [50] in today's form, but originally proposed by Franz Wegner for a discrete gauge group [64] in 1971, three years earlier. The lattice serves as a regulator here, comparable to e.g. continuum dimensional regularization. All fluctuations with too small wavelengths to be resolved on the lattice are suppressed by the introduction of a finite lattice spacing a. Similar to continuum regularization schemes, the introduction of a lattice cutoff violates some of the symmetries of the problem. The hypercubic space-time lattice violates Poincaré symmetry in the sense that continuous translation symmetry is replaced by a discrete translation symmetry. Thus, one can only shift the reference system by integer multiples of the lattice spacing a and only along the spatial axes xyz, given either an infinite extent of the lattice or a periodic boundary conditions in the spatial directions. In thermal field theory, the Poincaré symmetry along the time axis is broken by the heat-bath, i.e. the breaking is physically desired. Similarly, the continuous rotational symmetry is replaced by a discrete rotational symmetry, meaning that only rotations from one axis to another (rotations by integer multiples of $\pi/2$) are permitted.

As a warm-up, let us consider the action of a (free and massless) one-component scalar ϕ in the continuum

$$S^{\text{cont}}_{\text{scalar}} = \frac{1}{2}\int \mathrm{d}^4x\, \partial_\mu\phi(x)\, \partial_\mu\phi(x)\,. \tag{2.8}$$

This can be straight-forwardly discretized by standard finite-difference expressions for the derivatives

$$S^{\text{latt}}_{\text{scalar}} = \frac{a^4}{2}\sum_x \sum_{\mu=1}^{4} \left(\frac{\phi(x+\hat{\mu}a)-\phi(x)}{a}\right)^2 = a^2 \sum_{x\in\Lambda}\sum_{\mu=1}^{4} \phi(x)\left(\phi(x)-\phi(x+\hat{\mu}a)\right)\,, \tag{2.9}$$

where

$$x = (x_1,\, x_2,\, x_3,\, x_4)\ \ ,\ \ \ x_1, x_2, x_3, x_4 \in \mathbb{N}_0 \text{ and } x_4 < \frac{1}{Ta}$$

is the set of possible coordinates, we made the sum over directions μ explicit and $\hat{\mu}$ signifies the unit vector in μ-direction. Unfortunately, this strategy does not generalize so easily to gauge fields due to gauge freedom. Let us first revisit Eq. 2.1.

If we discretized the fermionic part of the QCD action S_{F} naively, we would end up with

terms like $\overline{\Psi}(x)\gamma_\mu D_\mu(x)\Psi(x+\hat{\mu}a)$, which under a gauge transformation

$$\begin{aligned}\overline{\Psi}(x) &\to \overline{\Psi}(x)\Omega^\dagger(x)\\ \Psi(x) &\to \Omega(x)\Psi(x)\\ D_\mu(x) &\to \Omega(x)D_\mu(x)\Omega^\dagger(x)\end{aligned}$$

behaves as

$$\overline{\Psi}(x)\gamma_\mu D_\mu(x)\Psi(x+\hat{\mu}a) \to \overline{\Psi}(x)\gamma_\mu D_\mu(x)\Omega^\dagger(x)\Omega(x+\hat{\mu}a)\Psi(x+\hat{\mu}a)\,,$$

thus it is clearly not invariant under a general, local gauge transformation Ω. Since we want our lattice implementation to be manifestly gauge invariant, we have to come up with something different.

One possible approach are so-called "link variables" $U_\mu(x)$. They live on the connection of two neighboring lattice sites x and $x+\hat{\mu}a$, are objects of the gauge group and can be thought of as "comparators" or "parallel transporters" of the gauge configurations on these two lattice sites. Therefore, they transform as

$$U_\mu(x) \to \Omega(x)U_\mu(x)\Omega^\dagger(x+\hat{\mu}) \tag{2.10}$$

under a gauge transformation Ω, which makes the combination $\overline{\Psi}(x)\gamma_\mu U_\mu(x)\Psi(x+\hat{\mu}a)$ clearly gauge invariant, as desired.

As opposed to the gauge fields $A_\mu(x)$, which are elements of the Lie-algebra of the gauge group, in our case $su(3)$, gauge links are elements of the gauge group itself and are therefore related to the original fields via

$$U_\mu(x) = \mathrm{e}^{iaA_\mu(x)}\,, \tag{2.11}$$

where the lattice spacing a has to enter in order to balance the mass dimension 1 of the A_μ-field in the exponent.

Still, one question remains: How can we construct a lattice-equivalent to S_G in (2.1)?

This can be done using the "plaquette"

$$\Box_{\mu\nu}(x) = U_\mu(x)U_\nu(x+\hat{\mu}a)U_\mu^\dagger(x+\hat{\mu}a+\hat{\nu}a)U_\nu^\dagger(x+\hat{\nu}a)\,, \tag{2.12}$$

the easiest closed path of parallel transporters of links on a lattice. As one can straightforwardly verify using (2.10), the plaquette behaves under gauge transformations as

$$\Box_{\mu\nu}(x) \to \Omega(x)\Box_{\mu\nu}(x)\Omega^\dagger(x)\,, \tag{2.13}$$

and therefore its trace is gauge-invariant. Moreover, the Baker-Campbell-Hausdorff-formula

$$\mathrm{e}^{A}\mathrm{e}^{B} = \mathrm{e}^{A+B+\frac{1}{2}[A,\,B]+\ldots}\,, \tag{2.14}$$

allows one to identify

$$\Box_{\mu\nu}(x) = \mathrm{e}^{ia^2 F_{\mu\nu}(x)+\mathcal{O}(a^4)} = \mathbb{1} + ia^2 F_{\mu\nu}(x) - \frac{a^4}{2} F_{\mu\nu}(x)F_{\mu\nu}(x) + \mathcal{O}(a^6)\,, \tag{2.15}$$

and finally set up the "Wilson action" for $SU(N)$ gauge fields

$$S_{\mathrm{W}}\,[U] = \frac{2N}{g^2}\sum_{x}\sum_{\mu>\nu}\left(1 - \frac{1}{N}\mathrm{Tr}_c\,\Box_{\mu\nu}(x)\right)\,, \tag{2.16}$$

where the subscript c for the trace stresses that it is a trace in color space. The prefactor in front of the sum is sometimes called $\beta = \frac{2N}{g^2}$. Due to the cutoff dependence of the coupling, as reviewed in Subsec. 2.1.3, β is a function of the UV cutoff and consequently a function of the lattice spacing a.

The Wilson action constitutes the main result of this section. Let us briefly recapitulate what we have done. We saw that the presence of fermions in the full QCD action implies using the link variables U_μ, as fundamental objects on the lattice. They can be combined to a plaquette, which serves as the main ingredient to the Wilson gauge action.

What remains to show is that the Wilson gauge action (2.16) indeed reproduces the continuum gauge action in the $a \to 0$ limit. Plugging (2.15) into (2.16), we firstly see that the constant term cancels. This term is insignificant, anyway, since operator expectation values are ratios of partition sums, and constants cancel that way. The second term vanishes due to the tracelessness of the generators of $SU(N)$ Lie groups

$$\mathrm{Tr}_c\,F_{\mu\nu} = F^a_{\mu\nu}\mathrm{Tr}_c\,T^a = 0\,. \tag{2.17}$$

Therefore the leading two terms cancel, and the remaining term

$$\frac{a^4}{2}\sum_{x}\sum_{\mu,\nu=1}^{4} F_{\mu\nu}(x)F_{\mu\nu}(x) \to \int \mathrm{d}^4x \sum_{\mu,\nu=1}^{4}\frac{1}{2}F_{\mu\nu}(x)F_{\mu\nu}(x) \tag{2.18}$$

is precisely the desired continuum action S_{G} in (2.1).

We have now seen how the action can be discretized. Computing observables with the path-integral (2.2) further involves the construction of the corresponding integration

measure. Our degrees of freedom are by the lattice rendered to be countably infinite at most. However, the integration is not over the gauge fields A_μ any more, but over the link variables U_μ, the integration measure is now promoted to the "Haar measure"

$$\mathcal{D}A_\mu(x) \to \prod_{\mu,\,x} \mathrm{d}U_\mu(x) \tag{2.19}$$

and corresponds (possibly) countably infinitely many, but ordinary integrals. Since one now integrates over the entire gauge group, gauge fixing is not necessary any more.

Note that (2.16) just describes pure $SU(3)$ Yang-Mills theory without fermions. This is often called the "quenched approximation". There are multiple ways to discretize fermions on the lattice, but they are complex and subtle objects and the derivation does not provide the reader with any new insights for understanding this thesis, so we omit this part of lattice gauge theory.

Also, we want to render the number of lattice points finite for all practical purposes. Eventually, one can compute the result at different volumes and choose the volume large enough such that it does not influence the results significantly. This procedure is often referred to as the "infinite volume limit".

As already mentioned a few paragraphs before, the introduction of a finite lattice spacing a introduces a natural cutoff in the ultraviolet (UV) regime, breaking a row of fundamental symmetries like continuous rotational and translational symmetry. These symmetries need to be restored if we want to make any physically relevant statements because the world as we perceive it features full Poincaré symmetry. Thus, to obtain meaningful results, we need to extrapolate to the continuum $a \to 0$. In fact, all observables $\mathcal{O}_a$ are functions of the lattice spacing a. If our a is sufficiently small, the assumption of $\mathcal{O}_a$ to be a polynomial is safe, and we can polynomially extrapolate to the physically meaningful continuum value $\mathcal{O}_{a=0}$. Here comes asymptotic freedom into play, meaning that the ignored interactions beyond the momentum cutoff $p_{\max} \sim \frac{1}{a}$ become smaller and smaller the closer one comes to the continuum, a feature that makes this treatment better-behaved in QCD than in other theories without asymptotic freedom. This entire procedure is often summarized as "taking the continuum limit".

2.2.2. Simulation algorithms and detailed balance

Even on a tiny lattice of 10 points in each direction, the partition sum (2.2) involves integrals over 10^4 gluon (and possibly quark) degrees of freedom that are mutually

coupled in a highly non-trivial way. A direct analytical computation is hopeless in realistic scenarios. What saves the day is that one can approximate the result in principle arbitrarily close by Monte-Carlo integration.

The strategy is to draw the field-theoretical degrees of freedom, for instance the link variables, directly as randomly distributed elements of $SU(3)$ following the distribution

$$P(U) \propto \mathrm{e}^{-S_{\mathrm{W}}[U]} \,. \tag{2.20}$$

The conceptually easiest way of achieving (2.20) would be drawing a random link configuration and see if it satisfies (2.20) by chance. However, this would be highly unlikely and therefore inefficient. Consequently, we need a more sophisticated way of building configurations satisfying (2.20) and to "renew" them, such that we can compute an expectation value. This "Markov-chain" can be created with the help of so-called "update algorithms", one of which we will introduce in the following.

All update algorithms have to maintain "detailed balance", meaning that the probability $T(U|U')$ to transition from a lattice configuration U to U' has to fulfill

$$T(U'|U)P(U) = T(U|U')P(U') \,, \tag{2.21}$$

where $P(U)$ is the total probability for a lattice configuration U to occur. Some algorithms maintain (2.21) naturally because they draw the new configuration according to rules that implement detailed balance from scratch, others have to fulfill detailed balance by a rejecting lattice configuration every now and then, the "Metropolis step" [65].

There is a comprehensive toolbox of algorithms to generate a random walk of successive lattice configurations. Some of them, like the cluster and worm algorithms, are highly efficient but not applicable to theories beyond scalar field theories. HMC, Langevin, Metropolis are algorithms that have been developed for the applications to gauge theories and fermions.

2.2.3. The hybrid overrelaxation algorithm

In the following, we will discuss two algorithms that can only be applied to pure gauge theories and scalar field theories. As we will see in Sec. 2.3, these are the only kinds of fields in which we are interested, anyway. On the gauge side, these algorithms were originally developed for $SU(2)$ gauge theory. For the reasons of simplicity, let us recapitulate the

derivation for two very common update algorithms for $SU(2)$ gauge theory. In these derivations, we closely follow the original papers [66, 67] and [48].

The "heatbath" algorithm was originally developed by Michael Creutz in 1979 [66]. The strategy is to generate random configurations of $SU(2)$ gauge fields that automatically occur with the correct probability weight and do not require a Metropolis step. Firstly, we notice that the fraction of the action of one specific link only depends on the 6 neighboring plaquettes (6 cases for $\mu > \nu$ if $\mu, \nu = 1, 2, 3, 4$)

$$\begin{aligned} S_{\text{loc}}\left[U_\mu(x)\right] =& \frac{\beta}{2}\text{Tr}\Bigg[6\cdot\mathbb{1} - U_\mu(x)\sum_{\mu\neq\nu}\Big(U_\nu(x+\hat{\mu}a)U_\mu^\dagger(x+\hat{\mu}a+\hat{\nu}a)U_\nu^\dagger(x+\hat{\nu}a) \\ &+ U_\nu^\dagger(x+\hat{\mu}a)U_\mu^\dagger(x+\hat{\mu}a-\hat{\nu}a)U_\nu(x-\hat{\nu}a)\Big)\Bigg] \\ \equiv& \frac{\beta}{N}\text{Tr}\left[6\cdot\mathbb{1} - U_\mu(x)\tilde{U}\right], \end{aligned} \tag{2.22}$$

where we call $\tilde{U}$ the sum of "staples" and strictly set $N = 2$ for now and in the following.

Secondly, we can parametrize each element of $U \in SU(2)$ as a 4-vector of real numbers with unit length c:

$$U = c_0\mathbb{1} + i\boldsymbol{c}\cdot\boldsymbol{\sigma}\,, \tag{2.23}$$

where $\boldsymbol{\sigma}$ is the vector of the Pauli matrices with their standard properties. This is a special feature of $SU(2)$ and does unfortunately not generalize to $SU(N)$ theories with $N \geq 3$.

With this in hand, we can rewrite the Haar measure as

$$\mathrm{d}U = \frac{1}{2\pi^2}\delta(c^2-1)\mathrm{d}^4c\,,$$

and thus the probability weight

$$\mathrm{d}P(U) \propto \mathrm{d}U\mathrm{e}^{\frac{\beta}{2}\mathrm{Tr}\,U\tilde{U}}\,,$$

where we drop constant factors and instead normalize the probability weight in the end.

Here, we can exploit that each sum of elements (like $\tilde{U}$) of $SU(2)$ is proportional to another element of $\overline{U} \in SU(2)$

$$\tilde{U} = \det\left(\tilde{U}\right)^{1/2}\bar{U} \equiv k\bar{U}\,.$$

Instead of $\mathrm{d}P(U)$, we can now consider $\mathrm{d}P(U\bar{U}^{-1})$, which is something like multiplying the integration variable with a constant, that, again, does not bother us. Hence,

$$\mathrm{d}P(U\bar{U}^{-1}) \propto \mathrm{d}U \mathrm{e}^{\frac{\beta k}{2}\mathrm{Tr}\, U} = \mathrm{d}^4 c \frac{1}{2\pi^2}\delta(c^2-1)\,\mathrm{e}^{\beta k c_0}\,,$$

using that all matrices in (2.23) are traceless except from the unity matrix. We perform the integration over $|\boldsymbol{c}|$ with the δ-distribution

$$\delta(c^2-1)\,e^{\beta k c_0}\,\mathrm{d}^4 c = \frac{1}{2}\sqrt{1-c_0^2}\,\mathrm{e}^{\beta k c_0}\,\mathrm{d}c_0 \mathrm{d}\Omega\,, \tag{2.24}$$

where $\mathrm{d}\Omega$ is the angular part of the $\boldsymbol{c}$-integration (usually parametrized by two angles φ and ϑ) and the length $|\boldsymbol{c}| = \sqrt{1-a_0^2}$.

Finally, this means we have to draw a value for c_0 according to the distribution

$$P(c_0) \propto \sqrt{1-c_0^2}\,\mathrm{e}^{\beta k c_0}\,,$$

which can be implemented for instance via the parametrization

$$c_0 = 1 + \frac{1}{\beta k}\ln(x)\,,$$

where x must be uniformly distributed in the interval $\mathrm{e}^{-2\beta k} < x < 1$ and is only accepted with probability $1-\sqrt{1-c_0^2}$ to account for the $\sqrt{1-c_0^2}$ in (2.25) [2]. For $\boldsymbol{c}$, one has to draw two angles $0 \le \varphi < 2\pi$ and $0 \le \theta < \pi$, such that

$$\begin{aligned} c_1 &= \sqrt{1-c_0^2}\cos\varphi\sin\vartheta \\ c_2 &= \sqrt{1-c_0^2}\sin\varphi\sin\vartheta \\ c_3 &= \sqrt{1-c_0^2}\cos\vartheta\,. \end{aligned}$$

This we can plug into (2.23) and obtain our updated link. Applying this procedure to each single link on the lattice is called an “update sweep”.

One advantage of the heatbath algorithm is that it is ergodic, i.e. after the initialization of a lattice configuration with random numbers, it relaxes to thermal equilibrium. Out of the algorithms with that same feature, it is the most efficient one. The decorrelation

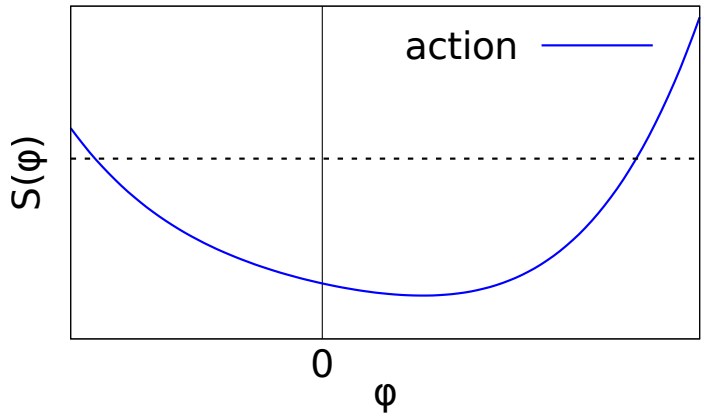

Figure 2.5.: Sketch of how the overrelaxation algorithm acts in the case of a scalar φ with action $S[\varphi]$. A configuration with a certain value for the action is reflected (along the dashed line) to another one with the same value for the action.

properties of the heatbath are pretty poor, though. That means that the heatbath fails to quickly "renew" the current lattice configuration, it is very similar to its predecessor.

An algorithm that does this very well is the "overrelaxation" algorithm. Its strategy is to construct a field configuration with the very same probability weight, i.e. the same action. This procedure applied to scalars can be pictured as in Fig. 2.5. It was first proposed by Stephen Adler in [67].

Let us derive how the overrelaxation algorithm works for $SU(2)$, again guided by [48]. From (2.24), we know that the sum of staples is proportional to an element of $SU(2)$. This means that the action is invariant under a transformation

$$U \to U' = \bar{U}^\dagger U^\dagger \bar{U}^\dagger \,, \tag{2.25}$$

as one can easily verify by evaluating

$$\mathrm{Tr}\left(U'\tilde{U}\right) = \mathrm{Tr}\left(\bar{U}^\dagger U^\dagger \bar{U}^\dagger \tilde{U}\right) = \mathrm{Tr}\left(k\bar{U}^\dagger U^\dagger\right) = \mathrm{Tr}\left(\tilde{U}^\dagger U^\dagger\right) = \mathrm{Tr}\left(U\tilde{U}\right) \,,$$

where we used that $\tilde{U}^\dagger = \tilde{U}^{-1}$, $\mathrm{Tr}\left(A^\dagger B^\dagger\right) = \mathrm{Tr}\,(BA)$ and (2.24). (2.25) constitutes the $SU(2)$ overrelaxation update.

[2]Note that although one accepts or declines random numbers in that step, it formally is not a Metropolis step because it is related to a suboptimal choice of random variables to draw. The heatbath algorithm for pure $SU(2)$ copes without a Metropolis step

The overrelaxation algorithm is numerically very cheap and features good decorrelation properties. However, it is non-ergodic by itself, meaning that it does not know about thermal equilibrium and that it necessarily has to be combined with another, ergodic algorithm.

The two algorithms we introduced in this section have quite complementary decorrelation and ergodicity properties. This is why we combine both algorithms to benefit from both their advantages while the disadvantages are compensated by each other. The married algorithm is often referred to as the "hybrid overrelaxation algorithm" (HOR).

Moreover, Cabbibo and Marinari found a generalization to $SU(3)$ in [68] by decomposing $SU(3)$ gauge links into their $SU(2)$-subgroups, so we can apply the HOR to pure $SU(3)$ gauge theories on the lattice. Also, applications of the same algorithm to scalar theories have been worked out, which we bear in mind for Sec. 2.3.

2.2.4. Error estimation

The update procedure is a Markovian procedure, it only depends on the immediate past. Since it depends on the past, though, our data suffers from autocorrelation effects. The most straight-forward way to get rid of this problem would be to measure the autocorrelation time τ for the different variables of interest and cut out multiple τ trajectories between two measurements.

The normalized autocorrelation function of an operator $\mathcal{O}$ is given by [69, 70]

$$\rho_{\mathcal{O}}(\Delta t) = \sum_t \frac{\langle \mathcal{O}(t+\Delta t)\mathcal{O}(t)\rangle - \langle \mathcal{O}(t)\rangle^2}{\langle \mathcal{O}(t)^2\rangle - \langle \mathcal{O}(t)\rangle^2} \equiv \mathrm{e}^{-\Delta t/\tau} \,. \tag{2.26}$$

The variables t and τ are Monte-Carlo times, i.e. they should be thought of as a time variable but do not carry any unit.

However, this is not the cleanest possible way to handle the autocorrelation. Firstly, the cut-out data still contains valuable, statistically relevant information. Secondly, the decorrelation is exponential, so for a sufficient suppression of autocorrelation effects one would have to cut out 3 to 4 multiples of τ, which even amplifies the first mentioned disadvantage.

One way of mathematically rigorously treating autocorrelations would be to determine the correlation matrix between the points and take that into account in averaging. Since

we want to perform high-precision studies with averages that often involve more than $N_{\text{ens}} = 10^5$, the correlation matrix would be $10^5 \times 10^5$, which is difficult to handle.

Another, more feasible possibility is binning the data and determining the error via a Jackknife analysis of the bins. Binning means that one divides the data into N_{bins} bins of equal size $N_{\text{binsize}} = \frac{N_{\text{ens}}}{N_{\text{bins}}}$. If one bin contains significantly more trajectories than the autocorrelation time τ, the autocorrelations will average, such that the bins themselves are not correlated with each other any more.

We estimate errors to the expectation value $\langle \mathcal{O} \rangle$ via the Jackknife method [69, 70]

$$\langle \mathcal{O} \rangle = \frac{1}{N_{\text{ens}}} \sum_{i=1}^{N_{\text{ens}}} \mathcal{O}_i \tag{2.27}$$

$$\overline{\mathcal{O}}_n = \frac{1}{N_{\text{ens}} - N_{\text{binsize}}} \left(\sum_{i=1,\, i \notin n\text{th bin}}^{N_{\text{ens}}} \mathcal{O}_i \right) \tag{2.28}$$

$$(\Delta \mathcal{O})^2 = \frac{N_{\text{bins}} - 1}{N_{\text{bins}}} \sum_{n=1}^{N_{\text{bins}}} \left(\overline{\mathcal{O}}_n - \langle \mathcal{O} \rangle \right) \left(\overline{\mathcal{O}}_n - \langle \mathcal{O} \rangle \right) , \tag{2.29}$$

where (2.27) is the usual way how to compute an average, (2.28) are the averages with one bin omitted, the so-called "Jackknives" and (2.29) shows how to extract an error estimate from the former two. The Jackknife method got its name because it can be applied universally and always gives a reliable error estimate without having to keep track of every single correlation.

To ensure a sensible error estimate, one has to vary N_{bins} and therefore N_{binsize} until one reaches a plateau. Typically, this plateau is reached at $N_{\text{bins}} \approx 20$. At larger N_{bins}, the size of the bin becomes too small and autocorrelation effects are still present. At smaller N_{bins}, there are too few bins to provide a sensible error estimate, i.e. the error of the error is too large.

2.2.5. Wilson loops

At this point it is natural to talk about which observables we investigate. Gauge invariance should be maintained by all our observables, which drastically limits the number of possibilities in pure gauge theories. One option is the space- and direction averaged

plaquette as introduced in Section 2.2. As we also saw in that section, the plaquette is closely related to the global and local action.

Another observable, that is somewhat related to the average plaquette is the "Wilson loop" [50]. It was introduced in its popular form in 1974 by Kenneth G. Wilson, and by Wegner in the condensed matter context three years earlier [64].

A Wilson loop $W(a;b;c;d)$ on the lattice consists of four Wilson line edges (comparable to 3.1)

$$W(a;b;c;d) = W(a,b)W(b,c)W(c,d)W(d,a)\,. \tag{2.30}$$

A single Wilson line $W(x;y)$ from x to y, in turn, is defined as

$$W(x;y) = \exp\left(i\int_x^y \mathrm{d}x'_\mu A_\mu(x')\right)\,. \tag{2.31}$$

Wilson found that the behavior of this Wilson loop differs between the confined phase and the (deconfined) QGP [50]. In the confined phase, the Wilson loop follows the "area law". If a, b, c, d form a rectangle of length l and width r, then

$$-\ln W(a;b;c;d) \propto r \times l\,, \tag{2.32}$$

as opposed to the QGP phase, where it is supposed to follow the "perimeter law"

$$-\ln W(a;b;c;d) \propto r + l\,. \tag{2.33}$$

This distinctive behavior of the Wilson loops allows us to use them as an order parameter for the confinement-deconfinement phase transition. Unfortunately, it is just a good order parameter if we consider pure $SU(3)$-Yang-Mills theory. As soon as we add (light) fermions, the Wilson loop becomes a less good order parameter, and one has to take the fermions into account via the chiral condensate $\langle\overline{\psi}\psi\rangle$, a better order parameter in this case. We will use the Wilson loop in a slightly modified form in our research, not primarily as an order parameter, but exploiting the connection to transport quantities made in Sec. 3.1.

2.3. Electrostatic Quantum Chromodynamics

Quantum Chromodynamics at high temperatures can be described by an effective field theory called "Electrostatic Quantum Chromodynamics" (EQCD). The central feature of hot QCD is that it effectively requires only three spatial dimensions, so Appelquist and

Pisarski [71], and Nadkarni [72] were the first to propose a threedimensional effective field theory for hot QCD. A systematic connection between this effective field theory and full QCD was developed by Braaten and Nieto [73]. Another comprehensive derivation and discussion of EQCD can be found in [74].

2.3.1. Separation of scales

As usually, the possibility of modeling a fundamental theory by an effective theory is indicated by a separation of scales. In our case, this is the separation of the hard thermal scale p_{hard} from the soft scale p_{soft} and the ultra-soft scale $p_{\mathrm{ultrasoft}}$

$$p_{\mathrm{ultrasoft}} = \frac{g^2 T}{\pi} \ll p_{\mathrm{soft}} = gT \ll p_{\mathrm{hard}} = \pi T \,. \tag{2.34}$$

Revisiting the running coupling of QCD (2.7), it is easy to see that this separation of scales only holds if g is sufficiently small, i.e. at sufficiently large scales Q. Due to the logarithmic dependence of (2.7) on Q, it is safe to say that the typical momentum scale is $Q \sim T$.

In EQCD, one integrates out the hard scale p_{hard} and hides the influence of that scale into the effective field theory parameters. Further integrating out the soft scale p_{soft} leads to another effective field theory called "Magnetostatic Quantum Chromodynamics" (MQCD), which we will not discuss explicitly in this work.

One feature of high-temperature QCD is that the theory behaves as effectively three-dimensional. One can motivate that by considering the Bose-Einstein distribution in a large-T expansion

$$n_{\mathrm{B}}(T;E) = \frac{1}{\mathrm{e}^{E/T}-1} \approx \frac{T}{E} - \frac{1}{2} + \mathcal{O}\left(\frac{E}{T}\right) , \tag{2.35}$$

where we see that this is dominated by the lowest lying energy state. In the Matsubara formalism[3], this would be the Matsubara-0-mode. Fermions do not have a 0-mode, so their contribution is neither dominant. In fact, one can imagine EQCD as just keeping the dynamics of the gluon-0-mode and wrapping the dynamics of all other modes into the effective field theory parameters.

Nevertheless, setting up an effective field theory always comes with some additional assumptions which further narrow the window in which the results are predictive. So

[3] For a thorough introduction of the Matsubara formalism, the basic tool of thermal field theory computations, see e.g. [74].

why is the effective field theory treatment necessary at all? The answer lies in (2.35), too. For a massless particle like the gluon $E \sim p$ holds. According to our initial separation of scales in hot QCD (2.34), we know that the some momenta are $p_{\text{soft}} \sim gT$,[4] so we obtain

$$n_{\text{B}}(T; E) \sim \frac{T}{p_{\text{soft}}} \sim \frac{1}{g} \,. \tag{2.36}$$

Since gluon loop propagators are proportional to that factor, the power counting in hot QCD is modified. Therefore, an expansion in loops does not involve powers of the coupling squared like in QED but only powers of g due to the $1/g$ factor from the internal propagator. Compared to the QED coupling, which is typically $e \sim 0.3$, the typical QCD coupling $g \sim 1$ is large, anyway. Combined with the worse power counting, it is really hard to obtain reliable results from purely perturbative expansions in hot QCD, a problem that was first observed by A. D. Linde [75]. This explains the necessity of an effective treatment as incorporated by EQCD.

2.3.2. The EQCD action

After discussing the motivation and necessity for an effective treatment of hot QCD, let us now write down the effective field theory Lagrangian. To start with, we assess the symmetries of hot QCD, which we would like to see reflected in EQCD, too. Hot QCD features gauge symmetry in all spatial directions. Since the distance between Matsubara modes $\Delta\tau = 2\pi T$ scales with temperature, we expect any derivatives in this direction to be negligible, $\partial_\tau A_\mu \sim 0$. Therefore, gauge freedom in the 0-direction is lost, meaning that nothing prevents A_0 any more from acquiring a mass and turning into a scalar particle (in the adjoint representation of $SU(3)$). Moreover, we expect Poincaré symmetry in all three spatial directions. Poincaré symmetry in the 0-direction is broken by the presence of the heatbath, anyway. Along these two demands of fundamental symmetries, one can write down the (continuum) EQCD action

$$S_{\text{EQCD}} = \int \mathrm{d}^3x \, \frac{1}{g_{\text{3d}}^2} \mathrm{Tr}\, F_{ij} F_{ij} + \mathrm{Tr}\, D_i \Phi \, D_i \Phi + m_{\text{D}}^2 \mathrm{Tr}\, \Phi^2 + \lambda \left(\mathrm{Tr}\, \Phi^2 \right)^2 \,, \tag{2.37}$$

where Φ is the foreseen adjoint scalar-remnant of A_0, g_{3d}^2 is the three-dimensional gauge coupling which now carries mass dimension 1, m_{D}^2 is the acquired screening mass that coincides with the Debye mass and λ is the scalar self-coupling that emerges from the 4-gluon interaction.

[4] Some momenta are even $\sim g^2/\pi T$ for which the power counting is even worse.

There are a couple of remarks to make on this effective action. In principle, also higher-dimension operators like $D_i F_{ij} D_k F_{kj}$ are allowed, but they correspond to higher order terms in the high-temperature expansion, which we truncate at mass dimension 4. Also, there is another operator that we omitted in (2.37), $\mu \mathrm{Tr}\, \Phi^3$. This operator explicitly violates the otherwise present $\mathbb{Z}^3$-symmetry and corresponds to a non-vanishing quark chemical potential. Since we do not consider cases with $\mu \neq 0$ in this work, we dropped this term. Moreover, $SU(N)$ groups with $N > 3$, there are actually two quartic scalar self-interactions, $\lambda_1 \left(\mathrm{Tr}\, \Phi^2\right)^2$ and $\lambda_2 \mathrm{Tr}\, \Phi^4$. In $SU(2)$ and $SU(3)$, the two terms are related to each other via $\left(\mathrm{Tr}\, \Phi^2\right)^2 = \frac{1}{2} \mathrm{Tr}\, \Phi^4$, so without loss of generality, we only considered the (numerically easier) former kind of self-coupling. A relation of the EQCD parameters g_{3d}^2,m_{D}^2 and λ to temperature T and the number of dynamical, massless quark flavors N_{f} in 4D-full QCD has been worked out up to at least two loops in [76, 77]. In 4D full QCD, the four-A_0-vertex is actually 0 at tree level due to the Lorentz structure and firstly enters at $\mathcal{O}(g^4)$. This explains why the values of λ are so small in EQCD. Along similar lines, the three-A_0 vertex is also forbidden. However, the $A_0 A_0 A_i$-interaction still persists in the $(D_i F_{ij})^2$-term in (2.37).

At this point, let us comment on the notion of EQCD being an effective field theory. Although very common, this statement might be a little bit too convservative, in fact. The spatial gluon degrees of freedom A^i are still explicitly present with their full dynamics, the temporal gluon A^0 as a scalar, which is strictly justified as discussed in the previous subsection. The fermions do contribute perturbatively through the EFT-parameters. So as an alternative to considering EQCD and effective field theory, one could also perceive it as a resummation scheme of full-QCD perturbation theory. In a sense, it preserves the original degrees of freedom more clearly than other effective field theories, the connection to full QCD via the perturbative matching procedure is rigorous and well-defined. Gauge freedom is still explicitly present, although in the temporal direction, it does not play a role any more as discussed. Other effective field theories like the Quark-Meson Model hide the gauge theory in their effective degrees of freedom [78]. Since QCD is strongly interacting length-scales that are characteristic for the Quark-Meson Model, the matching cannot be conducted perturbatively and is typically determined by fitting to experimental data. However, it has been established to call EQCD an effective field theory, therefore we will keep referring to EQCD in that sense.

2.3.3. EQCD predictions

EQCD has had a row of big successes in predicting thermodynamical properties of hot QCD.

The latest, $\mathcal{O}(g^6 \ln g)$ contribution to the perturbative determination of the QCD pressure required an EQCD treatment of the infrared physics, see Fig. 2.6 and [79]. This spectacularly shows how a perturbative expansion in EQCD overcomes some of the problems of full QCD perturbation theory, the tool of choice for the lower orders. The perturbative matching would suggest that EQCD results can never be better than the order of the perturbative matching. However, EQCD has the asset of resumming the 0-mode contributions with bad convergence behavior.

On the one hand, one can see the effective field theory treatment breaking down at small temperatures in Fig. 2.6, where the lattice data are certainly correct. On the other hand, we see that there are no lattice data at temperatures $T \gtrsim 4\Lambda_{\overline{\mathrm{MS}}}$, because simulations at such high temperatures involve a shrinking, but still finite extent of the 0 direction. In contrast, once we know that EQCD works reliably, i.e. it agrees well with lattice data at a certain temperature, the agreement must hold at all temperatures above that temperature of first agreement as we have seen in Subsec. 2.3.1. Therefore, one rather switches the framework from hot, full QCD lattice simulations to either EQCD perturbation theory or lattice EQCD. Due to EQCD being threedimensional, or, in lattice language, just having one time-slice, and the implicit treatment of the fermions, one still saves a lot of computation power by reducing to EQCD and carrying out lattice simulations there compared to $4D$-lattice QCD.

Eq. (2.7) gives the hint that the central assumption for dimensional reduction from full QCD to EQCD, the separation of scales (2.34), becomes more valid as T increases and g decreases as a consequence.

The range of validity of EQCD was predicted by Mikko Laine [80] to reach down to temperatures of $T \gtrsim 2T_\mathrm{c}$, where T_c is the transition temperature of the full QCD crossover [81] at $\mu = 0$. This crossover connects the confined phase with the deconfined, QGP phase, as we saw in Figure 2.4. Below $2T_\mathrm{c}$, the ultra-soft, soft and hard scales overlap each other so badly that integrating out only fluctuations at one of these scales is not justified any more.

Furthermore, EQCD can be solved on the lattice with considerably less numerical effort than full 4D QCD, due to its three-dimensional nature. In particular, the incorporation of quarks via EFT parameters instead of having to treat them dynamically is a huge advantage. Note that EQCD has a sign problem at nonvanishing quark chemical potential

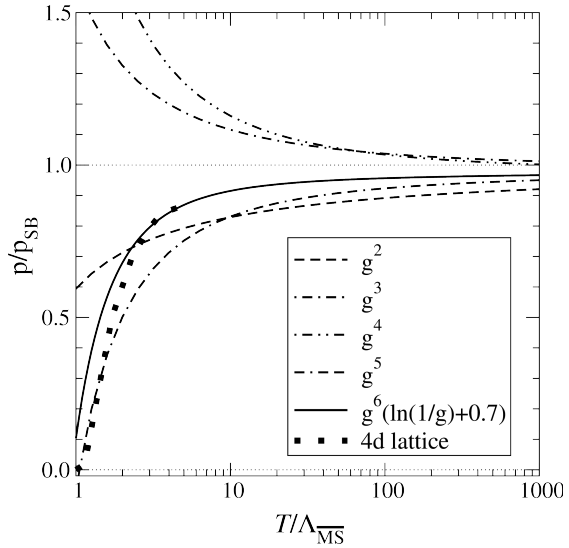

Figure 2.6.: The state-of-the-art perturbative prediction of the pressure of hot QCD. The last order involved a numerical stochastic perturbation theory treatment of infrared contributions to full QCD, evaluated in EQCD. Figure from [79], publication authorized by the copyright holder.

μ, too. However, the authors of [82] explain that it is easier to get rid of using analytical continuation.

The quark number susceptibility in the presence of a μ is simulated in the same reference, see Fig. 2.7. It is defined as

$$\chi_{ij} = \frac{1}{V} \frac{\partial^2}{\partial \mu_i \partial \mu_j} \ln \mathcal{Z} \,, \tag{2.38}$$

with the volume V, the chemical potential μ_i for the i-th quark flavor and the grand-canonical partition sum $\mathcal{Z}$. It is a measure for the "softness" of the equation of state, and an important measure for charge fluctuations in the QGP and influences a lot of observables in heavy ion collisions.

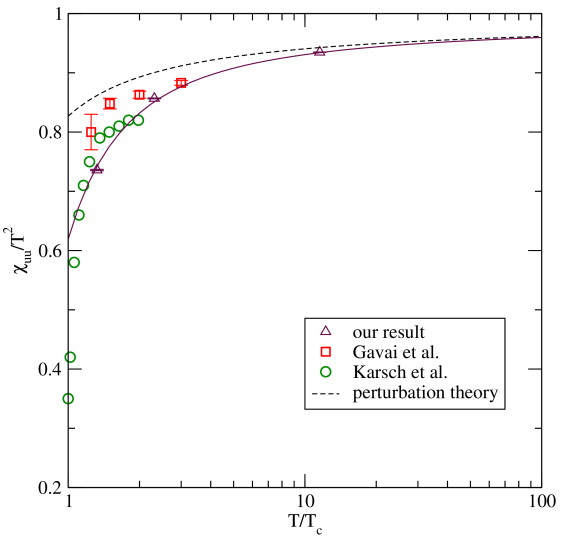

Figure 2.7.: Enabling a quark chemical potential via the $\mu \mathrm{Tr}\,\Phi^3$-term, one also has access to fermionic observables in EQCD, e.g. the diagonal quark number susceptibility. Figure from [82], publication authorized by the copyright holder.

2.4. Transport phenomena in QCD

2.4.1. Generic examples

Soon after the experimental confirmation of the existence of the quark-gluon plasma [58–61], there was a big effort underway to measure properties of that new state of matter and compare them to theoretical expectations.

For instance, it was found that the quark-gluon plasma comes surprisingly close to a perfect fluid at RHIC [13, 14] and at LHC [18–21]. In order to describe the QGP hydrodynamically, an equation of state is needed, i.e. the pressure p as a function of the temperature T (and possibly the baryon chemical potential μ). This is available directly from lattice calculations, for example in [83] or [84].

However, the dynamics of the QGP show small deviations from an ideal fluid, though still fluid-like. Consequently, it obeys higher-order transport equations, and in particular the coefficients therein are necessary to model the dynamics of the QGP correctly. For the covariant Navier-Stokes equation, these would be the shear-viscosity η as well as the

bulk viscosity ξ [85, 86]. In order to make a self-consistent theoretical prediction, there must be a way of determining transport coefficients from the underlying microscopic theory, QCD in the present case. This is done by so-called "Kubo formulae" [87] and requires an analytic continuation from Euclidean time to Minkowski time, which is in general underdetermined but can nevertheless be carried out with sophisticated statistical tools in some cases. Huge effort is put in determining η directly from the lattice, for instance in [88]. A perturbative determination was provided in [32], indicating that the perturbation theory does not converge well for η/s, even at very high temperatures. The situation for the bulk viscosity is even more complicated [89].

Another interesting feature of the QGP is that it radiates off photons. Photons interact only electromagnetically, meaning that they are influenced very little by the QGP after their production, making them a very clean and easy to detect probe of the properties of the QGP. The process of photon emission is encoded in the thermal photon production rate, calculated perturbatively in [33]. Photon production is the case, in which the convergence of the perturbative series works the best of all transport phenomena. Nevertheless, the convergence is still poor and one would preferably rely on a lattice result like [90]. Unfortunately, lattice data are only available at comparatively small temperatures due to the very same reasons explained in Subsec. 2.3.3.

Moreover, there are diffusion coefficients for light and heavy quark diffusion, both calculated perturbatively [32] and on the lattice [91–93].

These are some generic examples for "material properties" of the QGP that are attempted to calculate from the fundamental theory, QCD.

2.4.2. Jet broadening

Heavy-ion collisions do not only produce the QGP, but along with that also high-energy colored objects, the "jets" [94]. These fly through the medium and obtain modifications by the medium [95]. Since jets are objects that can be finally measured in detectors, they deliver important and direct insights into the nature of the QGP. Together with photons emitted by the QGP, one refers to them as "hard probes", where hard means that the exchanged momentum is larger than the medium scale, $q_\perp \gg T$, and therefore, the coupling g is comparably small due to asymptotic freedom. In this particular context, this explicitly does not mean that an expansion in loops works here, the application of resummation schemes or effective field theories like EQCD may very well be still necessary for precisely the reasons discussed in Sec. 2.3.

It was found pretty early that in passing the medium, the jets do lose energy and acquire transverse momentum [94], which can be pictured by the jet receiving bumps from the plasma constituents while passing the medium.

An important observable is the spectrum of particles that are emitted from a jet, for example a quark or a gluon. We will discuss a theoretical framework for this type of phenomena in Sec. 2.5.

2.5. Kinetic descriptions

In contrast to the lattice description, kinetic theory generically makes Minkowski-time information accessible. This is an important feature for describing transport processes which can be defined as how the system reacts to a (local) departure from the global equilibrium. Therefore, (global) thermal equilibrium is not a given and different, real-time techniques are needed.

2.5.1. The Boltzmann equation

One very common tool to describe transport phenomena is the Boltzmann equation. There are multiple ways to derive the Boltzmann equation, via the Liouville equation [85] or directly from field theory via the 2PI formalism [96]. The final result can be phrased as [97]

$$\left(\frac{\partial}{\partial t} + \boldsymbol{v}\cdot\nabla_{\boldsymbol{x}}\right) f^a(\boldsymbol{p},\boldsymbol{x},t) = -C^a\left[f\right] \tag{2.39}$$

in the absence of external forces. A few remarks on that equation: $f^a(\boldsymbol{p},\boldsymbol{x},t)$ is the (not necessarily equilibrium-) distribution function of a particle of species a, it is modified by interactions according to the collision kernel $C^a\left[f\right]$. Gluons, for instance, should have a fixed point at $f^{\mathrm{g}}(\boldsymbol{p},\boldsymbol{x},t) = n_{\mathrm{B}}(\boldsymbol{p})$, i.e. (2.39) should turn into $\partial_{\mathrm{t}} n_{\mathrm{B}}(\boldsymbol{p}) = 0$, and for fermions the Fermi-Dirac distribution, respectively. The collision kernel $C^a\left[f\right]$, in turn, contains all information about the interaction. Usually, one has to plug some (possibly resummed) perturbative result in here. Moreover, distribution functions

$$f^a(\boldsymbol{p},\boldsymbol{x},t) \equiv \frac{\mathrm{d}N^a}{\mathrm{d}^3x\,\mathrm{d}^3p} \tag{2.40}$$

include the particle number N^a of particles of species a. For that, a definition of the particle number is required. One has to define a way to count particles in a phase space cell $\Delta^3 x\, \Delta^3 p$. Last but not least, derivations of the Boltzmann equation involve an expansion in gradients, so the system should be far away from continuous phase transitions, where the correlation length ξ and thus the gradients diverge.

Aside from the perturbative matrix element, $C^a[f]$ typically contains a delta function that ensures overall energy-momentum conservation and a combination of the distribution functions f^a of all particles involved in the scattering process. For instance, a $2 \leftrightarrow 2$-process has the collision operator

$$C^{2\leftrightarrow 2}[f](\boldsymbol{p}) = \frac{1}{2}\int_{\boldsymbol{k},b_\perp{}',\boldsymbol{k}'} \frac{|\mathcal{M}(p,k,p'k')|^2}{(2p_0)(2k_0)(2p_0')(2k_0')}(2\pi)^4\delta^4(p+k-p'-k') \tag{2.41}$$
$$\times \left\{ f(\boldsymbol{p}) f(\boldsymbol{k}) \left[1 \pm f(\boldsymbol{p}')\right]\left[1 \pm f(\boldsymbol{k}')\right] - f(\boldsymbol{p}')f(\boldsymbol{k}')\left[1 \pm f(\boldsymbol{p})\right]\left[1 \pm f(\boldsymbol{k})\right]\right\},$$

where we assumed for simplicity that there is only one species of particles so that we can drop the subscript a, the "$+$" in the expressions with the distribution is to be taken if the particles are bosons and the "$-$" if the particles are fermions, the integration $\int_{\boldsymbol{k}} \cdots = \int \frac{\mathrm{d}^3 k}{(2\pi)^3} \ldots$ and $\mathcal{M}^2$ is a matrix element consisting of a cross-section and a dynamical weight.

Eq. (2.41) is a pedagogical example, but for QCD the situation is different. There are multiple species of particles involved over which one has to sum, there is a nontrivial Lorentz- and gauge group-structure, and there are also inelastic, $1 \leftrightarrow 2$-scattering processes involved.

2.5.2. AMY and its applications to jet broadening

So far, there have not been any requirements for the distribution function f except diluteness for f to be well-defined. There are numerous different transport philosophies of how to construct and simplify the Boltzmann equation, in particular its collision kernel. Some examples are BAMPS ("Boltzmann Approach to Multi-Particle Scattering") [98] or, more recently, SMASH ("Simulating Many Accelerated Strongly-interacting Hadrons") [99]. We will work in an extension of the AMY framework, proposed by Peter Arnold, Guy D. Moore and Laurence G. Yaffe in the early 2000's [100–105].

Their work was applied to jet-quenching and extended to next-to-leading order in the coupling α_s [97]. To start with, one splits the distribution function into two parts [97]

$$f^a(\boldsymbol{p},\boldsymbol{x},t) = n^a(\boldsymbol{p}, T(\boldsymbol{x},t), \boldsymbol{u}(\boldsymbol{x},t)) + \delta f^a(\boldsymbol{p},\boldsymbol{x},t)\,, \tag{2.42}$$

with the local temperature $T(\boldsymbol{x},t)$ and the local flow velocity $\boldsymbol{u}(\boldsymbol{x},t)$. n^a is the local equilibrium distribution around which one expands, containing all the soft, thermal physics, whereas δf^a are the hard perturbations (the jets) around that local equilibrium. They are very dilute, so it suffices to consider only single interactions of δf^a with the thermal medium described by n^a. Thence we rewrite (2.39) into

$$\left(\frac{\partial}{\partial t}+\boldsymbol{v}\cdot\nabla\right)\delta f^a(\boldsymbol{p},\boldsymbol{x},t)=-C^a\left[\delta f\right]\,. \tag{2.43}$$

In turn, $C^a\left[\delta f\right]$ can be decomposed into

$$C^a\left[\delta f\right]=C^a_{\text{large}}\left[\delta f\right]+C^a_{\text{coll}}\left[\delta f\right]+C^a_{\text{diff}}\left[\delta f\right]+C^a_{\text{conv}}\left[\delta f\right]\,, \tag{2.44}$$

at leading order. The different contributions originate from large-angle scattering, collinear scattering, diffusive processes and processes that convert the nature of the jet (e.g. from a quark to a gluon). At NLO, all C^a's except from C^a_{large} receive corrections. Additionally, a semi-collinear collision operator $\delta C^a_{\text{semi}-\text{coll}}$ is introduced.

A kinetic approach like AMY is highly eligible to be implemented into a Monte Carlo event generator that mimics the evolution of jets according to the theoretical approach. For AMY, this has been done in MARTINI [106].

We will not dive into the details of what processes make up all these contributions and at which scales they are most relevant here. One quantity that enters almost all parts of the decomposed collision operator is $C(\boldsymbol{b}_\perp)$. It is a rate that describes how likely it is for a particle at the speed of light to undergo an elastic scattering with (transversal) impact parameter $\boldsymbol{b}_\perp$.

Therefore, it is a key ingredient into transport descriptions of the QGP, from which transport coefficients like the shear viscosity or the thermal photon emission rate can be derived. In the context of jets, it delivers important insights into a jet undergoing multiple scatterings with the medium and in so acquiring transverse momentum $q_\perp$ ("jet-broadening"). In momentum space, it is defined as the transverse scattering rate $\mathrm{d}\Gamma/\mathrm{d}^2q_\perp$ at large momentum $\boldsymbol{p}$

$$\lim_{p\to\infty}\frac{\mathrm{d}\Gamma(\boldsymbol{p},\boldsymbol{p}+\boldsymbol{q}_\perp)}{\mathrm{d}^2q_\perp}=\frac{C(\boldsymbol{q}_\perp)}{(2\pi)^2}\,, \tag{2.45}$$

and can be converted to position space with the modified Fourier transform

$$C(\boldsymbol{b}_\perp)=\int\frac{\mathrm{d}^2q_\perp}{(2\pi)^2}\left(1-\mathrm{e}^{i\boldsymbol{q}_\perp\cdot\boldsymbol{b}_\perp}\right)C(\boldsymbol{q}_\perp)\,, \tag{2.46}$$

where we stress once more that this is *not* a common Fourier transform. Usually, there is rotational symmetry in the transverse plane, therefore all the information is encoded in $C(b_\perp)$ as a function of the absolute value of the impact-parameter-2-vector $\boldsymbol{b}_\perp$.

Beyond just making the jet change its direction, $C(b_\perp)$ has influence on C^a_{diff} via the "jet-broadening parameter" $\hat{q}$ [95]. It is defined as

$$\hat{q} \equiv \langle (\Delta q_\perp)^2 \rangle = \int_0^{q_{\max}} \frac{\mathrm{d}^2 \mathrm{q}_\perp}{(2\pi)^2} {q_\perp}^2 C(q_\perp)\,, \tag{2.47}$$

the second moment of the transverse collision kernel $C(q_\perp)$. This parameter describes how much the distribution of transversal momentum of the jet broadens while crossing the medium. $\hat{q}$ has to be regulated in the UV since $C(q_\perp) \sim g^4 T^3 / {q_\perp}^4$ at large $q_\perp$ [29], leading to a logarithmic divergence in the cutoff $q_{\max}$ that has to be customized to appropriate values for different set-ups.

2.5.3. Radiation spectra off of jets

As a second application beyond jet-broadening, $C(b_\perp)$ plays a crucial role in the description of collinear radiation, encoded into C^a_{coll} [103]. Collinear radiation was understood to be the main reason for "jet-quenching" [107], the jet's loss of energy in traversing the medium, not to be confused with jet-broadening. $C(b_\perp)$ goes into C^a_{coll} via the differential probability $\mathrm{d}P^a_{bc}/\mathrm{d}k$ of a parton of kind a to emit (collinear) particles of species b and c. The full formalism for the treatment of $\mathrm{d}P^a_{bc}/\mathrm{d}k$ was worked out in [107] and embedded into the AMY-framework in [97].

It was originally found by Zakharov in [24] that these emission spectra of particles with transverse momentum can be described by quantum mechanics. For our purpose, we will refer to the more recent nomenclature similar to [107–109].

The probability P^a_{bc} for a parton of kind a, produced at the time origin $t = 0$, to emit particles of kind b and c with longitudinal momenta (i.e. energies) k and $p - k$ follows the differential equation

$$\frac{\mathrm{d}P^a_{bc}}{\mathrm{d}k} = \frac{P^{a(0)}_{bc}(x)}{\pi p} \cdot \mathrm{Re} \int_0^\infty \mathrm{d}t' \int_{t'}^\infty \mathrm{d}t\ \nabla_{\boldsymbol{x}_\perp} \cdot \nabla_{\boldsymbol{y}_\perp} \left[\mathcal{K}(t, \boldsymbol{x}_\perp; t', \boldsymbol{y}_\perp; p, k) - (\text{vacuum}) \right] \big|_{\boldsymbol{x}_\perp = \boldsymbol{y}_\perp = 0}\,, \tag{2.48}$$

where $x = \frac{k}{p}$ and $\mathcal{K}(t, \boldsymbol{x}_\perp; t', \boldsymbol{y}_\perp; p, k)$ is a propagator in time and the transversal plane.

Each kind of possible scattering in QCD has different prefactors in that differential equation:

$$P_{bc}^{a(0)}(x) = \begin{cases} \frac{4}{3}g^2 \frac{1+(1-x)^2}{x}\,, & q \to gq \\ 3g^2 \frac{1+x+(1-x)^4}{x(1-x)}\,, & g \to gg \\ g^2\, N_{\mathrm{f}}(x^2+(1-x)^2)\,, & g \to q\overline{q} \end{cases} \tag{2.49}$$

The propagator $\mathcal{K}(t, \boldsymbol{x}_\perp; t', \boldsymbol{y}_\perp, p, k)$ follows a Schrödinger-like equation with the Hamilton-operator

$$H(\boldsymbol{b}_\perp) = -\frac{p\nabla^2_{\boldsymbol{b}_\perp}}{2k(p-k)} + \frac{m_b^2}{2k} + \frac{m_c^2}{2(p-k)} - \frac{m_a^2}{2p} - i\mathcal{C}_3(p,k,\boldsymbol{b}_\perp)\,, \tag{2.50}$$

where m_a, m_b, and m_c are the masses of the particles and $\mathcal{C}_3(x, \boldsymbol{b}_\perp)$ is a three-body amplitude that serves as a damping term in the associated path integral. It can be reduced to a combination of two-body amplitudes $C(b_\perp)$ up to next-to-next-to-leading order (NNLO) corrections in g^2 and additional suppressions by the number of colors $1/N$ via [29]

$$\mathcal{C}_3(p,k,\boldsymbol{b}_\perp) = \frac{C_b + C_c - C_a}{2C_a} C(\boldsymbol{b}_\perp) + \frac{C_a + C_c - C_b}{2C_b} C\left(\frac{k}{p}\boldsymbol{b}_\perp\right) + \frac{C_a + C_b - C_c}{2C_c} C\left(\frac{p-k}{p}\boldsymbol{b}_\perp\right)\,, \tag{2.51}$$

with C_a, C_b, and C_c being the respective Casimir operators.

The defining Schrödinger-like equation for $\mathcal{K}(t, \boldsymbol{x}_\perp; t', \boldsymbol{y}_\perp; p, k)$ reads

$$(i\partial_t - H(\boldsymbol{b}_\perp))\,\mathcal{K}(t, \boldsymbol{x}_\perp; t', \boldsymbol{y}_\perp; p, k) = i\,\delta(t-t')\,\delta^{(2)}(\boldsymbol{x}_\perp - \boldsymbol{y}_\perp)\,, \tag{2.52}$$

in the case of a homogeneous medium. A generalization to a non-homogeneous medium can be (formally) easily made by assuming a dependence of the Hamilton operator on the times / longitudinal coordinates t and t' of the two points.

Eventually, we saw that $C(b_\perp)$ contributes to the damping term in (2.50) via (2.51), which is a crucial ingredient for the propagator defined in (2.52) that finally goes into the actual splitting probability (2.48). This probability is the final observable and can be measured in heavy-ion collision experiments [58–61], and also goes into theoretical transport descriptions like the AMY framework that was briefly introduced in the previous subsection. Let us stress again that so far in this subsection, we have only made use of quantum mechanics. We shall see that all necessary applications of quantum field theory boil down to determining $C(b_\perp)$.

Using the definition of $C(b_\perp)$, it is a quite common approximation to expand $C(b_\perp)$ for small transversal separations $b_\perp$

$$C(b_\perp) = \frac{\hat{q}}{4} {b_\perp}^2 + \mathcal{O}({b_\perp}^3)\,. \tag{2.53}$$

With that, the equation for the propagator (2.52) turns into a standard Schrödinger equation for a harmonic oscillator and is consequently analytically solvable, which is very convenient.

Loosely speaking, it is the main goal of this thesis to improve on that very widespread, but sometimes also very crude approximation. Why an improvement is necessary will be discussed in Subsec 3.1.2.

3. Recent developments in jet broadening

In the following, we will review three key research efforts which prepared the ground for the progress the present thesis achieved. The publications that we discuss here are far more comprehensive than what we outline here, we focus on the aspects that are of particular relevance for our work.

3.1. $\mathcal{O}(g)$ plasma effects in jet quenching

As elaborated on in Sec. 2.5, high-energy jets are dominantly modified by infrared physics of the plasma, which is hard to tackle strictly perturbatively, as demonstrated in Sec. 2.3. Simon Caron-Huot has worked out in 2007 [29] how to deal with these jet modifications properly. In the following, we will first explain the strategy for this computation and then show the perturbative results that were computed.

3.1.1. Euclidean correlators for $C(q_\perp)$

It has been found by Casalderrey-Solana and Teaney [28] that the central quantity for jet-modification by the medium, $C(b_\perp)$, the position-space version of $C(q_\perp)$, can be computed as a light-cone Wilson loop in real-time full QCD, see Fig. 3.1.

The Wilson loop in the full theory reads

$$W(L,0,\boldsymbol{b}_\perp) = \mathrm{P}\,\exp\left(\int_0^L (-iA_-(L,0,0))\mathrm{d}x_+ + \int_0^{\boldsymbol{b}_\perp} (-iA_\perp(L,0,x_\perp))\mathrm{d}x_\perp \right.$$
$$\left. + \int_L^0 (-iA_-(L,0,\boldsymbol{b}_\perp))\mathrm{d}x_+ + \int_{\boldsymbol{b}_\perp}^0 (+iA_\perp(0,0,x_\perp))\mathrm{d}x_\perp \right), \quad (3.1)$$

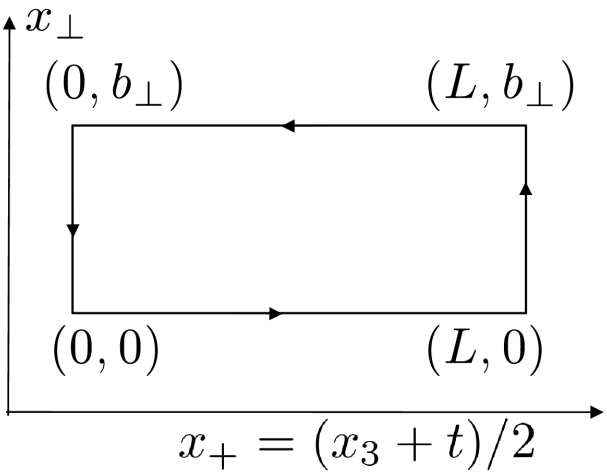

Figure 3.1.: Wilson loop for the determination of $C(b_\perp)$. The edges along the light cone coordinate $x_+ = \frac{1}{2}(x_3 + t)$ are the long edges with length L, the short edges along $x_\perp$ have transversal extent $\boldsymbol{b}_\perp$. Coordinates in the figure are given in the convention $(x_+, x_\perp)$.

where coordinates are given as $(x_+, x_-, \boldsymbol{x}_\perp)$. We see that the x_- coordinate does not play a role, since the jets are moving with (almost) the speed of light, $x_- = 0$ throughout the whole calculation, another hint to the three-dimensional nature of the problem.

The value of the Wilson loop can be related to $C(b_\perp)$ through

$$C(b_\perp) = -\lim_{L\to\infty} \frac{1}{L} \ln W(L, 0, \boldsymbol{b}_\perp)\,. \tag{3.2}$$

Unfortunately, calculations in real time are in general very hard. The main merit of [29] was to relate this Wilson loop to a modified version in Euclidean-time, three-dimensional EQCD

$$\begin{aligned}\tilde{W}(L, 0, \boldsymbol{b}_\perp) = \mathrm{P}\ \exp\Bigg(&\int_0^L \Big[-iA_z(z, 0) + \Phi(z, 0)\Big]\mathrm{d}z + \int_0^{\boldsymbol{b}_\perp} (-iA_\perp(L, x_\perp))\mathrm{d}x_\perp \\ &+ \int_L^0 \Big[+iA_z(z, \boldsymbol{b}_\perp) - \Phi(z, \boldsymbol{b}_\perp)\Big]\mathrm{d}z + \int_{\boldsymbol{b}_\perp}^0 (+iA_\perp(0, x_\perp))\mathrm{d}x_\perp\Bigg)\,.\end{aligned} \tag{3.3}$$

Just as for $C(b_\perp)$, we can make the rotational symmetry in the transversal plane as well as the eikonal propagation along the lightcone explicit and write $\tilde{W}(L, 0, \boldsymbol{b}_\perp) = \tilde{W}(L, b_\perp)$.

We recapitulate Caron-Huot's argument for the Euclideanization in (3.3) here, along the lines of App. B.1 in [33].

In the Minkowski-time many particle formalism, there are essentially three types of two-point functions: $G^{>}, G^{<}$ and the statistical propagator G^{F} [96], whereas in the Euclidean time formalism, there is only one correlator: G^{E}. The strategy is to consider the system along hyperplanes with $x^0 = \tilde{v}x^3$, where $\tilde{v} \leq 1$ holds for causally connected operators *in* the lightcone.

With G_{ij}, we will from now on denote the correlator of two operators $\mathcal{O}_i$ and $\mathcal{O}_j$. For now, we take the separation of the two operators $\mathcal{O}_i$ and $\mathcal{O}_j$ to be space-like, in particular $|x^3| > |x^0|$. At first sight, this fundamentally contradicts our assumption of time- or light-like separation from above and we will focus on that crucial aspect soon. For now, let us just take this fact for granted. All operators at space-like separations do commute, and therefore all different kinds of propagators, $G^{>}_{ij}$, $G^{<}_{ij}$ and G^{F}_{ij} are equal.

The ordering-averaged propagator $G^{\mathrm{rr}} = (G^{>} + G^{<})/2$ reads

$$G^{\mathrm{rr}}_{ij}(x^0, \boldsymbol{x}) = \int \mathrm{d}\omega \int \mathrm{d}q^3 \int \mathrm{d}^2 q_\perp \mathrm{e}^{i(x^3 q^3 + \boldsymbol{x}_\perp \cdot \boldsymbol{q}_\perp - \omega x^0)} G^{\mathrm{rr}}_{ij}(\omega, q^3, q_\perp) \,,$$

in Fourier space. We use the fluctuation-dissipation relation

$$G^{\mathrm{rr}}_{ij}(\omega, q) = \left(n_{\mathrm{B}}(\omega) + \frac{1}{2} \right) \rho_{ij}(\omega, q) = \left(n_{\mathrm{B}}(\omega) + \frac{1}{2} \right) \left(G^{\mathrm{R}}_{ij}(\omega, q) - G^{\mathrm{A}}_{ij}(\omega, q) \right) \,,$$

where n_{B} is the Bose-Einstein distribution function and $\rho_{ij}(\omega, q)$ is the expectation value of the commutator of the operators $\mathcal{O}_i$ and $\mathcal{O}_j$ (if they are fermionic the anti-commutator), along with the definition $\tilde{q}^3 = q^3 - (x^0/x^3)\,\omega$ to write

$$G^{\mathrm{rr}}_{ij}(x^0, \boldsymbol{x}) = \int \mathrm{d}\omega \int \mathrm{d}\tilde{q}^3 \int \mathrm{d}^2 q_\perp \, \mathrm{e}^{i(x^3 \tilde{q}^3 + \boldsymbol{x}_\perp \cdot \boldsymbol{q}_\perp)} \left(n_{\mathrm{B}}(\omega) + \frac{1}{2} \right) \rho_{ij} \left(\omega, \tilde{q}^3 + \omega \tfrac{x^0}{x^3}, q_\perp \right) \,.$$

As the next step, we would like to perform the integration over ω. To this end, we use contour integration, which relates $G^{\mathrm{R}}(\omega, q) = -iG^{\mathrm{E}}_{ij}(i\omega, q)$ via an analytic continuation. As elaborated on in App. B.1 of [33], there are no poles crossed under given circumstances, and similarly for the equivalent relation for G^{A}_{ij}. Only the poles of $n_{\mathrm{BE}}(\omega) + 1/2$ at $\omega = 2\pi i n T \,, \;\; n \in \mathbb{Z}$ with residues T have to be accounted for in closing the contour. We rename $\tilde{q}^3 \to q^3$ and find eventually

$$G^{\mathrm{rr}}_{ij}(x^0, x^3, x_\perp) = T \sum_n \int \frac{\mathrm{d}^3 p}{(2\pi)^3} \, \mathrm{e}^{i(x^3 q^3 + \boldsymbol{x}_\perp \cdot \boldsymbol{q}_\perp)} G^{\mathrm{E}}_{ij}(\omega_n, q^3 + i\omega_n \tfrac{x^0}{x^3}, q^3) \,, \tag{3.4}$$

with the standard Matsubara frequencies $\omega_n = 2\pi n T$.

Therefore, we have found a way to express correlation functions on the light-cone $x^0 = x^3$ through Euclidean correlation functions. Intuitively, what happens is that one exchanges the (physical) limit $\frac{x^0}{x^3} \to 1^-$ with $\frac{x^0}{x^3} \to 1^+$, where ϵ is a small, positive real number that controls the limit. In general, these limits do not agree. For the IR-dominated, essentially classical plasma modifications, however, it does not matter if one assumes the speed of light to be 1 or a tiny little bit larger since they are anyway slower by many orders of magnitude and the speed of light does not play a dedicated role in classical physics. Note that only the interface between the plasma and the jet is a classical one. The internal dynamics of the plasma still requires full quantum physics.

As usually in thermal field theory, one has to treat the 0-mode in 3.4 separately. Following Caron-Huot's argument in Sec. 3.2 of [29], the $n \neq 0$ contributions to (3.4) do not couple to the $n = 0$-sector directly and can be incorporated perturbatively. In fact, at small impact parameters $b_\perp$ or conversely at large transverse momentum $q_\perp$, they play an important role, as the author of this thesis and his co-author confirmed in Sec. 5. The $n = 0$ contributions, in turn, have correlation functions $G^{\mathrm{E}}_{ij}(0, q^3, q_\perp)$, which are precisely the correlation functions of EQCD, the effective theory for hot QCD that we introduced in Sec. 2.3. Instead of real-time, four-dimensional, full QCD perturbation theory, one can calculate $C(q_\perp)$ in three-dimensional, Euclidean, EQCD perturbation theory, which is much more feasible.

3.1.2. Perturbative determination of $C(q_\perp)$

Apart from the crucial theoretical development of using EQCD correlators instead of 4D, full QCD ones, Caron-Huot explicitly computed $C(q_\perp)$ to next-to-leading order (NLO) in the coupling g. The leading order (LO) was already computed by Aurenche, Zaraket and Gelis [110] and extended by Arnold and Xiao [27]

$$C^{\mathrm{LO}}(q_\perp) = C_{\mathrm{R}} \frac{g^2 T m_{\mathrm{D}}^2}{q_\perp^2 (q_\perp^2 + m_{\mathrm{D}}^2)}\,, \tag{3.5}$$

with C_{R} the Casimir of the representation R of the jet. If the jet consists of gluons, $C_{\mathrm{R}} = C_{\mathrm{A}} = 3$, if it consists of quarks, we have $C_{\mathrm{R}} = C_{\mathrm{F}} = 4/3$.

The NLO result from [29] reads

$$\begin{aligned}\frac{C^{\mathrm{NLO}}(q_\perp)}{g^4T^2C_{\mathrm{R}}\frac{4}{3}} =& \frac{7}{32q_\perp^3} - \frac{m_{\mathrm{D}} + 2\frac{q_\perp^2-m_{\mathrm{D}}^2}{q_\perp}\arctan\frac{q_\perp}{m_{\mathrm{D}}}}{4\pi(q_\perp^2+m_{\mathrm{D}}^2)^2} + \frac{m_{\mathrm{D}} - \frac{q_\perp^2+4m_{\mathrm{D}}^2}{2q_\perp}\arctan\frac{q_\perp}{2m_{\mathrm{D}}}}{8\pi q_\perp^4} \\ & - \frac{\arctan\frac{q_\perp}{m_{\mathrm{D}}}}{2\pi q_\perp(q_\perp^2 m_{\mathrm{D}}^2)} + \frac{\arctan\frac{q_\perp}{2m_{\mathrm{D}}}}{2\pi q_\perp^3} \\ & + \frac{m_{\mathrm{D}}}{4\pi(q_\perp^2 m_{\mathrm{D}}^2)}\left[\frac{3}{q_\perp^2+4m_{\mathrm{D}}^2} - \frac{2}{q_\perp^2+m_{\mathrm{D}}^2} - \frac{1}{q_\perp^2}\right]. \end{aligned} \tag{3.6}$$

Let us stress that both Fig. 3.5 and Fig. 3.6 are results for the dominant, soft jet modifications. Plots for two different α_{s} can be found in Fig. 3.2. We see that the NLO result (which is actually $C^{\mathrm{LO}}(q_\perp) + C^{\mathrm{NLO}}(q_\perp)$) is about a factor of 4 bigger at $\alpha_{\mathrm{S}} = 0.3$ and even at $\alpha_{\mathrm{S}} = 0.1$ still exceeds the leading order prediction by roughly a factor of 2. These are clear hints that convergence of the perturbative series is at least not maintained within the calculable range of the loop expansion. However, since our correlations of interest are now of Euclidean nature, we can evaluate the EQCD version of the Wilson loop in Fig. 3.1 on the lattice.

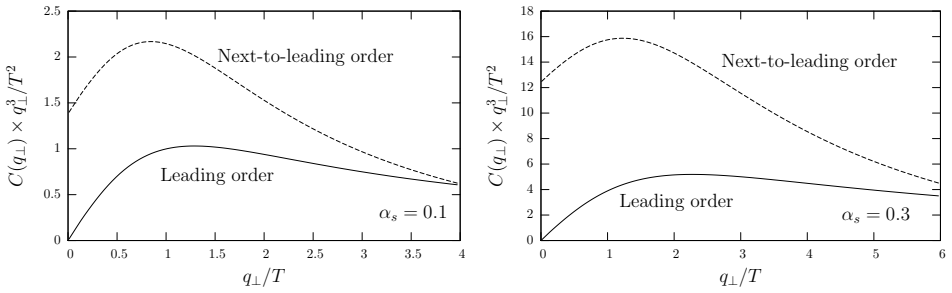

(a) $\alpha_{\mathrm{s}} = 0.1$ (b) $\alpha_{\mathrm{s}} = 0.3$

Figure 3.2.: Plot of (3.5) + (3.6) at two different, physically plausible α_{s}. Plots taken from [29], publication authorized by copyright holder.

However, (3.5) and (3.6) both just capture the physics up to the scale gT. The jet-broadening coefficient $\hat{q}$ (2.47), in turn, is sensitive to physics at all scales up to a process-dependent cutoff q_{max}, constituting the necessity of a matching of soft and hard physics. According to Caron-Huot, this transition should happen at some intermediate scale q^*

$$\hat{q} = \int_0^{q^*} \frac{\mathrm{d}^2q_\perp}{(2\pi)^2}\, q_\perp^2 C^{\mathrm{soft}}(q_\perp) + \int_{q^*}^{q_{\mathrm{max}}} \frac{\mathrm{d}^2q_\perp}{(2\pi)^2}\, q_\perp^2 C^{\mathrm{hard}}(q_\perp)\,. \tag{3.7}$$

The hard part $C^{\mathrm{hard}}(q_\perp)$ can also be computed in the framework presented in subsection 3.1.1, just not restricting to $n = 0$. The leading order contribution is just a bare gluon propagator connecting the two long edges of Fig. 3.1. In Feynman gauge, the propagator is $\propto \eta^{\mu\nu}$. Due to both lines being A_+ lines, this would correspond to η^{++}, which is 0. Therefore, the leading order vanishes.

Explicitly for $SU(3)$, the NLO result yields

$$C^{\mathrm{hard}}(q_\perp) = \frac{g^4 C_{\mathrm{R}}}{{q_\perp}^4} \int \frac{\mathrm{d}^3 p}{(2\pi)^3} \frac{p - p_3}{p} \left[6 n_{\mathrm{B}}(p)(1 + n_{\mathrm{B}}(p)) + 2 N_{\mathrm{f}} n_{\mathrm{F}}(p)(1 - n_{\mathrm{F}}(p')) \right] , \quad (3.8)$$

where N_{f} is the number of massless dynamical fermion flavors, $n_{\mathrm{F}}(p)$ is the Fermi-Dirac distribution and $p' = p + \frac{q_\perp^2 + 2 q_\perp \cdot p}{2(p - p_3)}$.

3.2. The jet quenching parameter from the lattice

Following that suggestion, Marco Panero, Kari Rummukainen, and Andreas Schäfer set up an exploratory lattice study [30]. To this end, the necessary developments are: discretizing EQCD on the lattice, discretizing our observable, the Wilson loop (3.3) on the lattice, and extrapolating the length of the loop to infinity $L \to \infty$. In order to obtain quantitative results, one would like to extrapolate $C(b_\perp)$ point-wise to the continuum. However, [30] was only planned as an exploratory study and not set up for this purpose.

Adapted to the conventions that are used throughout this thesis (c.f. [111]), the EQCD continuum action (2.37) can be implemented on the lattice as

$$\begin{aligned} S_{\mathrm{EQCD,L}} = & \frac{6}{Z_{\mathrm{g}} g_{\mathrm{3d}}^2 a} \sum_{x, i>j} \left(1 - \frac{1}{3} \mathrm{Tr}\, \square_{x,ij} \right) \\ & + 2 Z_\Phi \sum_{x,i} \mathrm{Tr} \left({\Phi_{\mathrm{L}}}^2(x) - \Phi_{\mathrm{L}}(x) U_i(x) \Phi_{\mathrm{L}}(x + \hat{i} a) U_i^\dagger(x) \right) \\ & + \sum_x \left[Z_2(y + \delta y) \mathrm{Tr}\, \Phi_{\mathrm{L}}^2 + Z_4 \left(\mathrm{Tr}\, \Phi_{\mathrm{L}}^2 \right)^2 \right] , \end{aligned} \quad (3.9)$$

$$\square_{x,ij} \equiv U_i(x) U_j(x + \hat{i} a) U_i^\dagger(x + \hat{j} a) U_j^\dagger(x) , \quad (3.10)$$

where Φ_{L} is the lattice version of the adjoint scalar field Φ, rescaled with $\sqrt{a}$, $\square_{ij}$ is the three-dimensional version of the plaquette in the $i-j$-plane, the Z factors are multiplicative

renormalization constants and the δ's stand for additive counterterm renormalizations, which we will discuss in greater detail in Sec. 3.3. The (dimensionless) versions of the EQCD parameters are

$$\beta \equiv \frac{6}{Z_{\mathrm{g}} g_{3\mathrm{d}}^2 a}\,, \qquad y \equiv \frac{m_{\mathrm{D}}^2\left[\mu_{\overline{\mathrm{MS}}} = g_{3\mathrm{d}}^2\right]}{g_{3\mathrm{d}}^4}\,, \qquad x \equiv \frac{\lambda}{g_{3\mathrm{d}}^2}\,, \tag{3.11}$$

where we used the dimensionful coupling $g_{3\mathrm{d}}^2$ to set the scale.

The most straight-forward and obvious choice of the Z's and δ's in (3.9) would be all Z's set to 1 and all δ's set to 0. For reasons that will become evident in the following section, this is not the neatest choice. The authors of [30] decided to choose

$$\begin{aligned}
Z_\phi =& \frac{6}{\beta}\,, \qquad Z_2 = \left(\frac{6}{\beta}\right)^3\,, \qquad Z_4 = \left(\frac{6}{\beta}\right)^3 \\
\delta x =& \frac{0.328432 - 0.835282x + 1.167759x^2}{\beta} \\
\delta y =& -\frac{3.175911535625\,(3+5x)\beta}{12\pi} \\
& - \frac{1}{(4\pi)^2}\left[20x(3-x)\left(\ln\beta + 0.08849\right) + 34.768x + 36.130\right]\,.
\end{aligned} \tag{3.12}$$

Their lattice version of (3.3) reads

$$\tilde{W}(L, b_\perp) = \mathrm{Tr}\left(\tilde{U}_{(0,0);(L,0)} U_{(L,0);(L,b_\perp)} \tilde{U}^{-1}_{(0,b_\perp);(L,b_\perp)} U^\dagger_{(0,0);(0,b_\perp)}\right) \tag{3.13}$$

$$\tilde{U}_{x;x+(L,0)} = \prod_{n=0}^{n_{\mathrm{L}}-1} U_3\left(x + an\boldsymbol{e}_z\right) \exp\left(-Z\,\Phi(x + a(n+1)\boldsymbol{e}_z)\right)$$

$$U_{x;x+(0,\boldsymbol{a})} = \prod_{n=0}^{n_{\boldsymbol{a}}-1} U_1\left(x + an\boldsymbol{e}_x\right)\,,$$

where U_i is the standard gauge link in the i-direction, Z is the renormalization factor for our observable, which they set to $Z = \frac{6}{\beta}$ and the transversal direction was chosen without loss of generality to be the x-direction. The longitudinal extent of the Wilson loop in lattice units is n_{L}, the transversal extent is $n_{\boldsymbol{a}}$.

After carrying out the full QCD-EQCD matching, they end up with the two EQCD parameter sets in Tab. 3.1.

T	n_f	x	y
$398\,\mathrm{MeV}$	2	0.1	0.448306
$2\,\mathrm{GeV}$	2	0.06	0.710991

Table 3.1.: 3D EQCD parameters in [30].

Computing $C(b_\perp)$ on the lattice according to (3.2) involves an extrapolation of $\mathrm{L} \to \infty$. In practice this turns out to be a hard task for various reasons, one of them is that the signal-to-noise ratio gets worse as one increases the enclosed area of the loop, i.e. the relative error of the results grows. Panero *et. al.* decided to ameliorate that problem by using the multilevel algorithm, a technique that reduces the noise for large Wilson loops by pre-averaging parts of the loop [112, 113]. We will discuss the multilevel algorithm in greater detail in Sec. 5. The authors of [30] do not comment on how precisely they carry out the $\mathrm{L} \to \infty$ limit, supposedly they just look for a finite length L, at which the error that is introduced by the finite length is subdominant compared to the Monte Carlo error. It does not harm too much since there are still finite lattice spacing systematic errors in the calculation, anyway.

Despite these minor technical issues, important and impressive results were obtained in [30], most notably the first determination of $C(b_\perp)$ on the lattice at two different temperatures, displayed in Fig. 3.3. The results displayed in Fig. 3.3 do not seem to suffer from big finite lattice spacing corrections, the results at different values of β lie on top of each other up to a fairly good accuracy. An extrapolation of $C(b_\perp)$ to the continuum seems to be feasible, and would be additionally facilitated by the completion of the $\mathcal{O}(a)$ lattice improvement (see Sec. 3.3 and Chap. 5).

At very small spatial separations $g_\mathrm{3d}^2 b_\perp$, we expect EQCD perturbation theory to work. Indeed, we can estimate that close to $g_\mathrm{3d}^2 b_\perp = 0$, both curves in Fig. 3.3 are well described by a perturbative series, on whose shape we will elaborate further in Sec. 5. One important feature of this perturbative series is that there is no intercept, which we recognize in both scenarios in Fig. 3.3. Apart from that, both curves look qualitatively the same, just that the larger temperature tends to marginally larger values of $C(b_\perp)$.

Panero, Rummukainen and Schäfer also extracted a guess for $\hat{q}$ from their results. Because it lacks a proper continuum extrapolation and the hard contribution of (3.7), it should merely be seen as a landmark than as a strict quantitative result with reliable error bars.

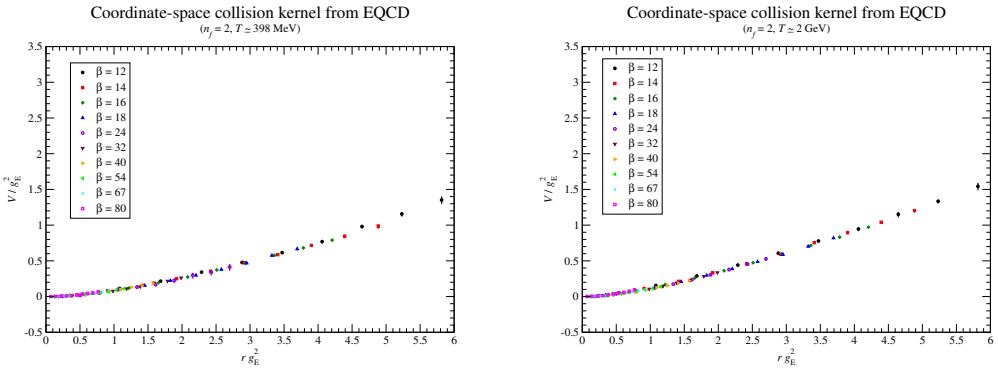

(a) $T \approx 398$ MeV (b) $T \approx 2$ GeV

Figure 3.3.: Exploratory lattice results for $C(b_\perp)$, here called $V(r)$, divided by the dimensionful EQCD gauge coupling g_E^2, in our notation g_{3d}^2. The transversal separation, which we call $g_{3d}^2 b_\perp$, is denoted with $r g_E^2$. Figures taken from [30], publication authorized by the copyright holder.

3.3. $\mathcal{O}(a)$ improvements in lattice EQCD

We now discuss how one can further improve compared to [30] and the non-obvious choices for the multiplicative and additive renormalization constants in (3.9).

All three parameters of continuum EQCD, g_{3d}, m_D^2 and λ receive loop corrections as usual in quantum field theory. Since both couplings are dimensionful but power series have to be in terms of dimensionless quantities, they both have to be balanced by a power of the only other scale in our theory, the UV lattice cutoff a. Thus, a fictitious parameter p would receive the corrections

$$p = p_{\text{bare}} + g_{3d}^2 a \, p_{1-\text{loop}}^{\text{gauge}} + \lambda a \, p_{1-\text{loop}}^{\text{scalar}} \tag{3.14}$$

at one loop and analogously for the higher orders, where also mixed terms with powers of both g_{3d}^2 and λ can occur. In a scenario, where perturbation theory is supposed to work, we can therefore compute the leading order corrections in the power expansion in the lattice spacing and subtract. This brings us closer to the desired continuum limit. Despite the perturbative expansion does not work for the infrared parts of our problem, as we have seen in Fig. 3.2, it does so very well in the ultraviolet regime. Since the scale of the lattice-continuum matching is UV cutoff scale, the lattice spacing a, our perturbative

lattice-continuum matching takes place around a momentum scale that is so deep in the UV that the use of perturbative methods is uncritical.

By an expansion in both EQCD lattice perturbation theory and continuum EQCD perturbation theory, almost all of the renormalization coefficients in (3.9) were determined analytically [114]. We make the application of these results to $SU(3)$ explicit and repeat the results for convenience, starting with the multiplicative renormalization factors

$$\frac{Z_4}{Z_\Phi^2} = g_{3\mathrm{d}}^2 a \left(1 - g_{3\mathrm{d}}^2 a \left[\frac{\Sigma}{4\pi} + 18\frac{\xi}{4\pi}\right]\right) , \tag{3.15}$$

$$\frac{Z_2}{Z_\Phi} = g_{3\mathrm{d}}^4 a^2 \left(1 + g_{3\mathrm{d}}^2 a \left[-\frac{\Sigma}{8\pi} + (-9+10x)\frac{\xi}{4\pi}\right]\right) , \tag{3.16}$$

$$\frac{1}{Z_\mathrm{g}} = 1 + g_{3\mathrm{d}}^2 a \left(\frac{1}{8}\frac{\Sigma}{4\pi} + \frac{7}{9} + \frac{37}{2}\frac{\xi}{4\pi}\right) \tag{3.17}$$

and continuing with the additive renormalization

$$\delta x = g_{3\mathrm{d}}^2 a \left(3 + 18x^2\right) \frac{\xi}{4\pi} , \tag{3.18}$$

$$\delta y_{1-\mathrm{loop}} = -\frac{1}{g_{3\mathrm{d}}^2 a} \left(6 + 10x\right) \frac{\Sigma}{4\pi} , \tag{3.19}$$

$$\begin{aligned} \delta y_{2-\mathrm{loop}} = -\frac{1}{(4\pi)^2} \Bigg(& 10x \left[\frac{3\Sigma^2}{2} + 3\Sigma\xi - 6\delta\right] \\ & + 9 \left[\frac{7\Sigma^2}{8} - \frac{\Sigma\pi}{6} + \frac{31\Sigma\xi}{6} + 2\kappa_1 - \kappa_4 - 4\rho - 4\delta\right] \\ & + 20x(3-x) \left[\ln\frac{6}{g_{3\mathrm{d}}^2 a} + \zeta - 3\Sigma\xi\right]\Bigg) , \end{aligned} \tag{3.20}$$

where we encounter some numbers that result from standard integrals in EQCD lattice-continuum matching defined in [115], $\Sigma = 3.17591153562522$, $\xi = 0.152859324966101$, $\zeta = 0.08849$, $\delta = 1.942130$ and $2\kappa_1 - \kappa_4 - 4\rho = 1.968325$. This improvement compensates all discretization errors at $\mathcal{O}(a)$ except from the one in y. About the linear-in-a-improvement for y, we know from App. A of [111] that it kicks in at three-loop order, preventing an analytic calculation due to sheer complexity, and that it has the parametric form

$$\delta y_{3-\mathrm{loop}} = g_{3\mathrm{d}}^2 a \, \left(C_0 + C_1\, x + C_2\, x^2 + C_3\, x^3\right) . \tag{3.21}$$

Beyond that, the renormalization Z of the observable itself, the modified Wilson loop

(3.13), has been determined also analytically [111]

$$\frac{Z^2}{Z_\Phi\, g_{3\mathrm{d}}^2 a} = 1 + g_{3\mathrm{d}}^2 a \left(\frac{\Sigma}{4\pi} - 12 \frac{\xi}{4\pi} \right) \tag{3.22}$$

At this point, let us take some time to understand how this setup compares to the one in (3.12). The most notable difference is that instead of $g_{3\mathrm{d}}^2 a$, Panero et.al. express their lattice spacing dependence in inverse powers of β which is equivalent in outcome but requires some slight modifications of matching constants along the way. Furthermore, they only use the leading order expressions for the multiplicative renormalization factors Z_4, Z_2 and Z, giving rise to other errors of $\mathcal{O}(a)$. Since there is the missing three-loop y-counterterm generating $\mathcal{O}(a)$ discretization errors, still, no improvement scheme that lacks this contribution can be rigorously called superior, even if drops other, known $\mathcal{O}(a)$ contributions. The results in [30] are not extrapolated to the continuum and at finite lattice spacing $g_{3\mathrm{d}}^2 a$ or β, they will look differently even though they were obtained at the same values of x and y. The non-uniqueness of discretizations is a common phenomenon in numerics and should not be worrying as long as the continuum values agree.

4. Full $\mathcal{O}(a)$ improvement in lattice EQCD

This chapter will review [116], in which the author of this thesis and his co-author undertook the necessary technical development of determining the $\mathcal{O}(a)$ correction in the lattice-continuum matching of 3D EQCD theory. The direct diagrammatic evaluation appears too difficult to pursue; so we will use an alternative method to extract the corrections. Since the $m_{\rm D}$-renormalization is the only missing $\mathcal{O}(a)$-contribution, it can be determined by fitting to a line of constant physics. EQCD features a phase transition, which we will utilize to obtain such a line.[1]

In the remainder of this chapter, we present our investigation of the matching problem. Section 4.1 sets the theoretical stage. Section 4.2 presents our approach to determining the 3-loop mass renormalization indirectly from lines of constant physics, leading to results we present in Section 4.3. A few odds and ends appear in the two appendices A.1 and A.2.

For the impatient reader, here is a very short summary. EQCD has two parameters, the mass-squared y and scalar self-coupling x (the gauge coupling just sets a scale). For a given value of the self-coupling x, there is a critical y-value where a phase transition occurs. We find this point at several lattice spacings, and extrapolate to the continuum behavior; the slope of the fit at $a = 0$ is precisely the $\mathcal{O}(a)$ mass correction which must be compensated. Perturbative arguments show that the resulting slope should depend on x as a third-order polynomial. Determining this at several x-values allows us to fit all polynomial coefficients, which are presented with their covariance matrix in Eq. (4.11) and Table 4.3.

This chapter and the appendices A.1 and A.2 are based on work published in Physical Review D [116]. In order to respect the formulation of the precise arguments and

[1] Note that the phase transition in EQCD is unphysical in the sense that it is not related to any phase transition in 4D thermal QCD. Indeed, 4D QCD with physical quark masses has a crossover at zero quark chemical potential [83, 84]; the pure-glue theory at high temperature has a Z_3-breaking phase structure which is related to the EQCD phase transition in a 1-loop analysis [76], but because EQCD lacks a true Z_3 symmetry, this is essentially a coincidence (see however Ref. [117]).

their interpretation originally made, parts of this chapter are adopted from the original publication or slightly paraphrased to fit better in the context of this thesis. The author of this thesis was involved at all stages of this project. The concluding section of the original publication was omitted since the plans we phrased there coincided with what was done in Chap. 5.

4.1. Theoretical setup

EQCD has been extensively introduced in Sec 2.3, in particular its continuum action (2.37) and its lattice discretization (3.9). We use the parameter convention of (3.9) together with all known improvements at $\mathcal{O}(a)$: (3.15), (3.18), and (3.22).

Our update algorithm will not be presented in full detail, since the bigger picture was already given in Sec. 2.2 and the actual algorithm is almost identical to [118]. We use the standard Wilson gauge action and nearest-neighbor scalar gradient or "hopping" term given in (3.9). The only crucial difference to the presented $SU(2)$ + fundamental scalar-case concerns the treatment of the hopping term in the gauge field update. It arises from the scalar kinetic term, which translates into

$$\int \mathrm{d}^3x \,\mathrm{Tr}\, D^i\Phi D^i\Phi \to 2Z_\Phi \sum_{\boldsymbol{x},i} \mathrm{Tr}\, \Big(\Phi_\mathrm{L}^2(\boldsymbol{x}) - \Phi_\mathrm{L}(\boldsymbol{x})U_i(\boldsymbol{x})\Phi_\mathrm{L}(\boldsymbol{x}+a\hat{i})U_i^\dagger(\boldsymbol{x})\Big) \tag{4.1}$$

in the lattice formulation, where Φ_L is the rescaled, dimensionless lattice version of the adjoint scalar field, Z_Φ is a field renormalization factor, and $U_i(\boldsymbol{x})$ is the standard gauge link at lattice site $\boldsymbol{x}$ in direction i. In contrast to the fundamental scalar case treated in [118], the present hopping term is non-linear in the link. Therefore, it has to be incorporated into the link update via a Metropolis step. Our scalar update, on the other hand, is a mixture of heatbath updates with the $x\mathrm{Tr}\,\Phi^4$ term included by Metropolis accept/reject, and the overrelaxation update introduced in Ref. [118]. We update sites in checkerboard order. Our code was modified from the OpenQCD-1.6 package [119].

Now we return to the parameters of the continuum and lattice actions. For this choice of parameters, 1-loop relations between the lattice gauge and scalar couplings and their continuum values, and two-loop relations for the scalar mass, are known: (3.15), (3.18), and (3.22).[2] The matching between the lattice and continuum is such that we know the

[2]The paper is written for general gauge groups, where there are two independent scalar self-couplings. These are equivalent in $SU(3)$, so we take $x_2 = 0$ in their notation. Note that in the lattice action in [111],

lattice x and $g_{3\mathrm{d}}^2$ parameters up to $\mathcal{O}(g_{3\mathrm{d}}^4 a^2)$ corrections. Effects from higher-dimension operators (present in the Wilson action and nearest-neighbor hopping term) are also of $\mathcal{O}(a^2)$. We also know the multiplicative rescaling between y and y_{latt} to the same precision, and we know the $\mathcal{O}(1/a)$ and $\mathcal{O}(1, \ln(a))$ additive contributions to y. Only the (3-loop) $\mathcal{O}(a)$ additive contribution to y is unknown. Therefore any $\mathcal{O}(a)$ difference in a physical result between lattice treatments at different lattice spacings must arise due to this additive contribution.

The phase structure of EQCD was extensively examined in the 90's, for example in [120]. The theory has a $\mathbb{Z}_3$ symmetry which is broken if $\mathrm{Tr}\Phi^3$ takes a nonvanishing value. There is a line of phase transitions separating a large-y region, where $\mathbb{Z}_3$ symmetry is preserved, from a small-y region where $\mathbb{Z}_3$ symmetry is spontaneously broken. Unlike the transition in $SU(2)$ fundamental [118] or adjoint [76] theories, this transition line extends over all x values, since the phases are distinguished by a global discrete symmetry breaking. At small x values the transition is first order; there is a tricritical point, and for large x values it is second order [120]. Values of x corresponding to dimensional reduction from physical temperatures and quark numbers all land in a region where the transition is first order; they also lie below the critical value y_{crit}, so physical QCD corresponds to metastable points in the EQCD phase diagram. (We emphasize again that the phase transition in EQCD is not related to any thermal phase transitions which may or may not occur in 4D QCD.)

Our methodology will consist of determining, for a given x value, the value y_{crit} where the phase transition occurs. Doing so at a series of lattice spacings provides a lattice determination of the lattice spacing a dependence of y_{crit}. Since the only $\mathcal{O}(a)$ error remaining in our lattice implementation of the theory is an additive shift to y, the slope of $y_{\mathrm{crit}}(a)$ when we extrapolate the lattice spacing $a \to 0$ determines the unknown linear-in-a correction to y at each given x value.

Formally, we know that the $\mathcal{O}(a)$ lattice-continuum additive δy contribution arises from 3-loop scalar self-energy diagrams in lattice perturbation theory [114]. Even without computing these graphs, we can see that they involve 0, 1, 2, and 3 factors of the scalar self-coupling. Therefore, making $N = 3$ in the expression from [111] explicit, we repeat the lattice mass-squared in terms of the continuum y value in (3.9) from (3.15) and

x_1 and x_2 actually have to be interchanged for consistency with the rest of that paper. Also, since the normalization of the lattice scalar field is arbitrary, we have chosen $Z_\Phi = 1$, that is, we normalize our hopping term to have unit norm.

(3.18),

$$S_{\mathrm{EQCD,L}} = \ldots + \sum_x Z_2(y+\delta y)\mathrm{Tr}\,\Phi_{\mathrm{L}}^2\,, \tag{4.2}$$

$$Z_2 = g_{3\mathrm{d}}^4 a^2 \left(1 + g_{3\mathrm{d}}^2 a\left[-\frac{\Sigma}{8\pi} + (-9+10x)\frac{\xi}{4\pi}\right]\right) \tag{4.3}$$

$$\begin{aligned}\delta y = &-\frac{1}{g_{3\mathrm{d}}^2 a}\frac{\Sigma}{4\pi}(6+10x) + \delta y_{3\mathrm{loop}} \\ &-\frac{1}{16\pi^2}\left[10x\left(\frac{3}{2}\Sigma^2 + 3\Sigma\xi - 6\delta\right) + \left(\ln\left(\frac{6}{g_{3\mathrm{d}}^2 a}\right) + \zeta - 3\Sigma\xi\right)(60x - 20x^2)\right. \\ &\left. +9\left(\frac{7}{8}\Sigma^2 - \frac{\Sigma\pi}{6} + \frac{31\Sigma\xi}{6} + 2\kappa_1 - \kappa_4 + 4\rho - 4\delta\right)\right]\,,\end{aligned} \tag{4.4}$$

where $\zeta = 0.08849$, $\delta = 1.942130$ and $4\rho - 2\kappa_1 + \kappa_4 = -1.968325$. The undetermined $\mathcal{O}(a)$ additive contribution must be parametrically of form

$$\delta y_{3\mathrm{loop}} = g_{3\mathrm{d}}^2 a\Big(C_0 + C_1 x + C_2 x^2 + C_3 x^3\Big). \tag{4.5}$$

With results at enough x values, we can perform a polynomial fit to extract these coefficients, and use it to determine the correction at any x value.

Eventually we want to apply EQCD to study QCD. Dimensional reduction at a specific temperature (hence gauge coupling) and number of light fermions leads to a specific x and y value. The 2-loop reduction formulae between high-temperature 3+1 dimensional full QCD and EQCD were worked out by Kajantie *et. al.* [76,77] and we use a nonperturbative value of $\Lambda_{\overline{\mathrm{MS}}}$ from [54]. These lead to the specific x and y values, which we will later investigate for $C(q_\perp)$ behavior, shown in Table 4.1 and depicted in Figure 4.1. To minimize errors in a future investigation, we will examine the mass renormalization at the x-values indicated, except the smallest value where our method will prove ineffective. We will also study larger values of x which do not correspond to any physical QCD regime.

T	n_{f}	x	y
250 MeV	3	0.08896	0.452423
500 MeV	3	0.0677528	0.586204
1 GeV	4	0.0463597	0.823449
100 GeV	5	0.0178626	1.64668

Table 4.1.: 3D EQCD parameters for four typical scenarios.

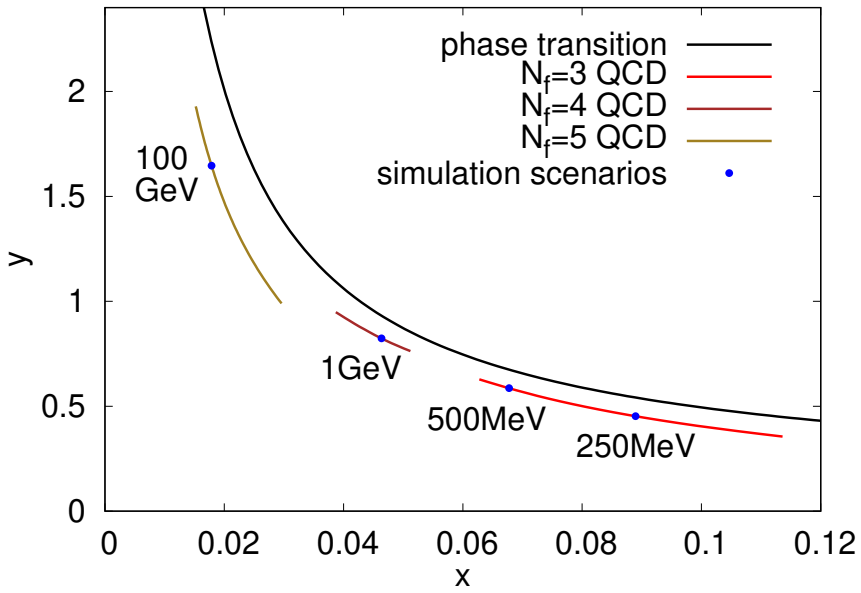

Figure 4.1.: xy phase diagram of EQCD with the lines on which EQCD matches full QCD at Temperature T and N_f quark flavors. The phase transition if of first order in the physically interesting region [120], and the physically relevant points lie in the supercooled "high-temperature" symmetric phase below the transition line. The blue points mark our scenarios of interest from Table 4.1.

The determination of $y_{\rm crit}$ faces the usual challenges of supercritical slowing down, associated with determining a first order phase transition point numerically. In the next section we present a methodology for evading this problem.

4.2. Our method

The standard way of determining $y_{\rm crit}$ would be by applying multicanonical reweighting in order to enforce tunneling between the two phases [120]. This is rather inefficient, so we develop another approach to efficiently determine the transition temperature of a first-order phase transition on the lattice.

The main idea is to prepare a lattice configuration where the two phases coexist and are permanently compared to each other at the phase boundaries. If we miraculously guessed the exact value of $y_{\rm crit}$, the symmetric phase volume would change only via Brownian motion. If our value for y were close to but not exactly $y_{\rm crit}$, the phase boundaries would feel a small net pressure, and would tend to allow the preferred phase to expand at the expense of the other. This leaves us with two questions:

- How do we prepare such configurations?
- How can we tune the mass to its critical value and balance the Brownian motion of the phase boundaries?

The true order parameter of EQCD is $\mathrm{Tr}\,\Phi^3$, which indicates whether the $\mathbb{Z}_3$-symmetry of Φ is present or broken. However, the phase transition can also be spotted in $\mathrm{Tr}\,\Phi^2$ (see Fig. 4.2), which has smaller fluctuations and leads to a more stable phase discriminator; so we use it in the following. Our approach begins by bounding $y_{\rm crit}$ by performing a simulation in a modest-sized cubic box, starting from a quite positive y value and decreasing it after each update sweep. At some value, $\mathrm{Tr}\,\Phi^2$ abruptly jumps. Then one steadily increases y until the value abruptly falls. This determines upper and lower *spinodal* y-values; $y_{\rm crit}$ must lie between, typically close to the upper value.

Next we estimate $\mathrm{Tr}\,\Phi^2_{\rm symm}$ and $\mathrm{Tr}\,\Phi^2_{\rm brok}$, the values of $\mathrm{Tr}\,\Phi^2_{\rm L}$ in each of these phases at a mass close to the transition temperature, which we do in separate simulations which are initialized with either vanishing or large constant Φ values. The method will be rather insensitive to the exact values of these quantities, so it is not important if the determinations are from somewhat incorrect y values.

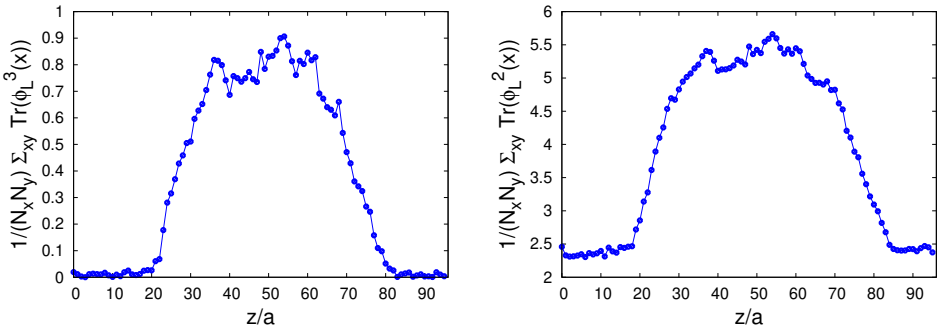

(a) $\frac{1}{N_x N_y}\sum_{x,y}\mathrm{Tr}\,\left(\Phi_{\mathrm{L}}^3(\boldsymbol{x})\right)$ (b) $\frac{1}{N_x N_y}\sum_{x,y}\mathrm{Tr}\,\left(\Phi_{\mathrm{L}}^2(\boldsymbol{x})\right)$

Figure 4.2.: $\mathrm{Tr}\,\Phi^3$ and $\mathrm{Tr}\,\Phi^2$, integrated over transverse directions, as a function of the z direction in a $36^3\times 96$ box at $g_{3\mathrm{d}}^2 a=\frac{1}{3}$, $x=0.08896$ and $y=0.47232$. There is a region near 0 (periodically identified with 96) which is in the symmetric phase, and a region near 50 which is in the broken phase, as well as two phase boundaries. The phases are visible in either order parameter but the fluctuations in $\mathrm{Tr}\,\Phi^2$ are smaller.

Next we set up our mass tuning algorithm. We work in a rectangular periodic lattice with one long (L_z) direction and two equal shorter ($L_x=L_y$) directions. Initially we make the y (Lagrangian) value z-coordinate dependent,

$$y(z)=y_{\mathrm{crit,est}}+\Delta y\cos(2\pi z/L_z)\,, \tag{4.6}$$

with Δy chosen initially to be large enough that $y_{\mathrm{crit,est}}\pm\Delta y$ are above/below the spinodal values. After a series of update sweeps, the field will find the symmetric phase where y is large and the broken phase where y is small, generating our configuration with both phases and two phase boundaries. Then the magnitude of Δy is gradually lowered over a series of update sweeps; if one phase starts to win out over the other, the estimated critical value is adjusted.

With our starting two-phase configuration and estimated y_{crit} in hand, we proceed to the more accurate determination of y_{crit}. We continue to evolve with a space-uniform y value, but we adjust it after each lattice site-update according to

$$y_{\mathrm{L,\,new}}=y_{\mathrm{L,\,old}}+c_{\mathrm{B}}\cdot\left(\frac{\frac{1}{V}\sum_{\boldsymbol{x}}\mathrm{Tr}\,\Phi^2-\mathrm{Tr}\,\Phi^2_{\mathrm{symm}}}{\mathrm{Tr}\,\Phi^2_{\mathrm{brok}}-\mathrm{Tr}\,\Phi^2_{\mathrm{symm}}}-0.5\right)\,, \tag{4.7}$$

where $y_L\equiv Z_3(y+\delta y_{2\mathrm{loop}})$ and c_{B} is a small coefficient that controls the strength of the adjustment. The quantity in brackets here is an estimate for the fraction of the volume

which lies in the broken phase, based on the known (approximate) values of $\mathrm{Tr}\,\Phi^2$ in each phase. Therefore, the adjustment term shifts y upwards (making the symmetric phase more preferred) when more volume is in the broken phase, and downwards (making the broken phase more preferred) if more of the volume is symmetric.

The coefficient c_{B} is small, $\mathcal{O}\left(\frac{1}{N_{\mathrm{x}}N_{\mathrm{y}}N_{\mathrm{z}}}\right)$, such that the evolution of y is as mild as possible, consistent with enough restorative force to prevent either phase from "winning." Specifically, whenever y deviates from y_{crit}, there is a net force on the interface, equal to the surface area times ΔF the free energy difference between phases. At $y = y_{\mathrm{crit}}$, $\Delta F = 0$ and there is no net force on the interface. Away from $y = y_{\mathrm{crit}}$, we can expand ΔF in a Taylor series in $y - y_{\mathrm{crit}}$. At leading order in small $y - y_{\mathrm{crit}}$, the free energy difference will be linear in $y - y_{\mathrm{crit}}$, and the central value of y which maintains coexistence will equal y_{crit}. At quadratic order, $\mathrm{d}^2F/\mathrm{d}y^2 \neq 0$ means that the restorative force is slightly biased, and we will obtain an incorrect value for y_{crit}. We test for such a distortion by performing a second evolution where c_{B} is twice as large, to confirm that the central value of y is the same within errors (which it is in all cases we considered).

4.3. Results

We use the procedure described in the previous section to determine the critical value $y_{\mathrm{crit}}(x, a)$ for several values of the scalar self-coupling x, each at several lattice spacings. The exact list of lattices considered is given in Table A.2. Because our procedure leads to relatively long autocorrelation in the estimated y_{crit} value, the errors must be determined via the jackknife method using relatively wide jackknife bins; we vary the bin widths until the error estimates stabilize. We then subtract the known 1- and 2-loop contributions and apply the known multiplicative rescalings [114] from the results and convert $y_{\mathrm{L,\,crit}} \to y_{\mathrm{2loop,\,crit}}$. For each x value, we must extrapolate this quantity to zero lattice spacing; the intercept is the continuum critical y value and the slope at the intercept is the desired $\mathcal{O}(a)$ additive correction to the scalar mass.

Because our $y_{\mathrm{crit}}(x, a)$ results are quite precise but the a values are not extremely small, we anticipate that $y_{\mathrm{crit}}(x, a)$ contains corrections beyond linear order in a. In principle, we could straightforwardly fit a polynomial of order N_{poly} in $g_{\mathrm{3d}}^2 a$ as

$$y_{\mathrm{crit}}\left(g_{\mathrm{3d}}^2 a\right) = \sum_{j=0}^{N_{\mathrm{poly}}} y_j (g_{\mathrm{3d}}^2 a)^j \,. \tag{4.8}$$

However, as often occurs, ever-higher order coefficients are ever less certain, and including too many coefficients tends to overfit the data and artificially inflates the final fitting errors. In order to extract these coefficients as efficiently as possible from the data, we would like to build in our knowledge about the convergence of the perturbative series to the fit. A useful tool to implement this is constrained curve fitting [121, 122]. Motivated by a rough estimate of the radius of convergence $(g_{\rm 3d}^2 a)_{\rm conv} \approx 0.5$, we make the a priori-guess

$$|y_i| \leq \frac{y_0}{2^i}\,, \tag{4.9}$$

having obtained y_0 from a standard, unconstrained fit. We then use this estimate to choose the size of a zero-centered chisquare prior on each fitting parameter. The procedure has almost no impact on the determined values of y_0 and y_1, where the data is far more constraining than the prior. In practice, a quadratic polynomial is sufficient to give a good fit with a reasonable χ^2. The results of these fits are given in Table 4.2 and the fits themselves are displayed in Fig. 4.3. We also confirmed by varying the volume that any finite-volume effects are smaller than our statistical error bars.

x	$y_{\rm crit,\,cont}$	$\delta y_{\rm 3loop}/g_{\rm 3d}^2 a$
0.0463596	0.9293(13)	−0.467(19)
0.0677528	0.67627(85)	−0.298(10)
0.08896	0.54092(76)	−0.1750(74)
0.13	0.4043(18)	−0.037(18)
0.2	0.2961(15)	0.004(15)

Table 4.2.: Results of our five EQCD simulation sets.

We caution the reader that, while y_0 and y_1 can be interpreted as the continuum critical point and the 3-loop $\mathcal{O}(a)$ additive mass renormalization coefficient, we cannot interpret y_2 as a 4-loop mass renormalization or use it to further improve the lattice-continuum matching. That is because there are many uncontrolled $\mathcal{O}(a^2)$ corrections which influence y_2. For instance, there are unknown 2-loop $\mathcal{O}(a^2)$ lattice-continuum corrections to x, which influence the critical value via $(dy_{\rm crit}/dx)\delta x$. Similarly, tree-level $\mathcal{O}(a^2)$ high-dimension operators and $\mathcal{O}(a^2)$ corrections to g^2 (which we could interpret as uncertainties in the scale setting) also lead to $\mathcal{O}(a^2)$ effects in the $y_{\rm crit}$ value. Because $(dy_{\rm crit}/dx) \sim x^{-2}$, the $\mathcal{O}(a^2)$ and other higher-order effects will become severe as we go towards small x values. Therefore small x requires the use of very fine lattices. Furthermore, when x is small, there becomes a hierarchy of mass scales in the problem; $m_{A,\rm brok} \gg m_\Phi \gg m_{A,\rm symm}$. Both effects make the accurate extraction of y_1 at small x very numerically demanding. Therefore we did not treat the smallest x value shown in Table 4.1. Instead, we add two

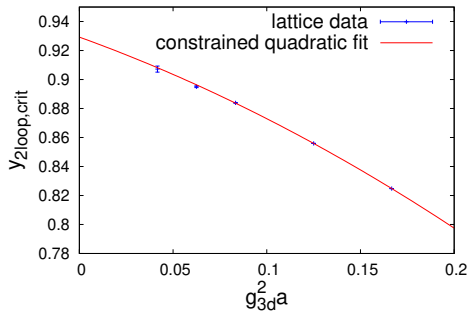

(a) $x = 0.0463597$

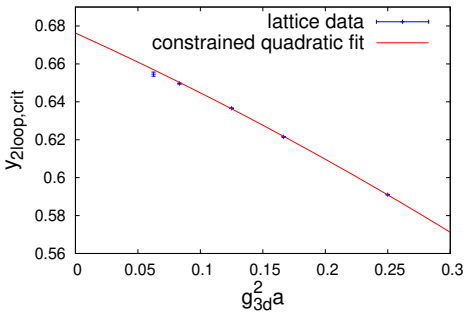

(b) $x = 0.0677528$

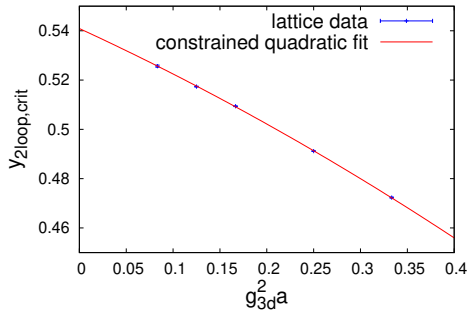

(c) $x = 0.08896$

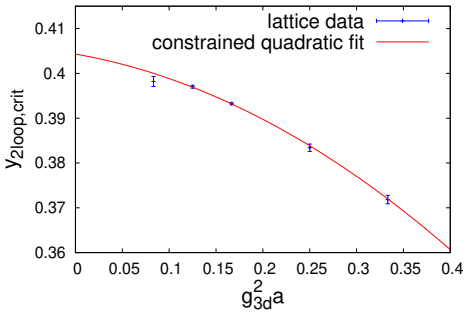

(d) $x = 0.13$

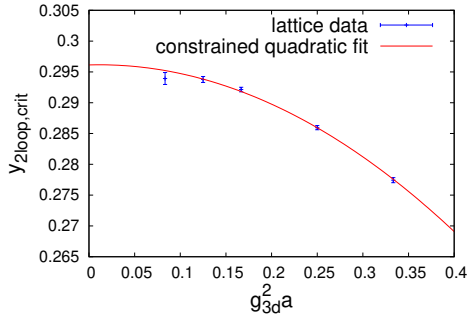

(e) $x = 0.2$

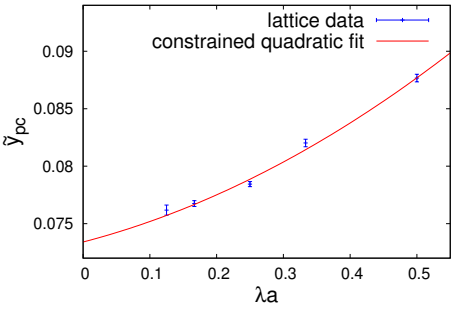

(f) pure scalar

Figure 4.3.: Fits of $\mathcal{O}(g_{3\mathrm{d}}^2 a)$ behavior for different x.

larger values of x, $x = 0.13$ and $x = 0.20$, which are still within the domain where the transition is first order, but which give us a broader x range over which to fit y_1 as a function of x.

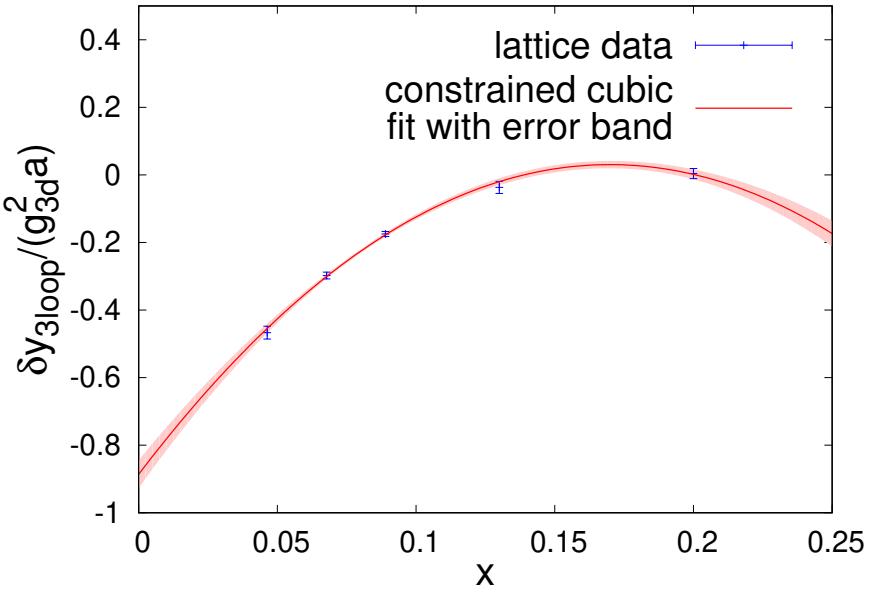

Figure 4.4.: Grand fit of $\frac{\delta y_{3\mathrm{loop}}}{g_{3\mathrm{d}}^2 a}(x)$ with error band.

Next we use our results for $y_1(x)$ to fit its overall x dependence. The parametric form of the $\mathcal{O}(g_{3\mathrm{d}}^2 a)$-correction [111] was given in (4.5). The x^3 coefficient corresponds to 3-loop diagrams containing only scalar lines. It is therefore equal to the $\mathcal{O}(a)$ mass renormalization term in the theory in the $g_{3\mathrm{d}}^2 \to 0$ limit, which is a scalar theory. We explain our (different) procedure to treat this scalar theory in App. A.1; our analysis leads to the result

$$C_3 = \frac{\delta\tilde{y}_{3\mathrm{loop}}}{\lambda a} = 0.0151(55)\,. \tag{4.10}$$

Here $\tilde{y} \equiv m^2(\mu = \lambda)/\lambda^2$ is the scalar mass, made dimensionless using the scale λ rather than the scale $g_{3\mathrm{d}}^2$; it equals y/x^2 up to the effect of the different renormalization scale. We incorporate this result as a prior in fitting a cubic polynomial to the results of Table 4.2. The resulting fit,

$$\frac{\delta y_{3\mathrm{loop}}}{g_{3\mathrm{d}}^2 a}(x) = 0.0151(55)\,x^3 - 31.8(28)\,x^2 + 10.80(74)\,x - 0.886(41)\,, \tag{4.11}$$

$\mathrm{cov}(C_i, C_j)$	C_0	C_1	C_2	C_3
C_0	0.001700	-0.02997	0.1101	$-3.563 \cdot 10^{-8}$
C_1	-0.02997	0.5451	-2.046	$1.129 \cdot 10^{-6}$
C_2	0.1101	-2.046	7.899	$-1.079 \cdot 10^{-5}$
C_3	$-3.563 \cdot 10^{-8}$	$1.129 \cdot 10^{-6}$	$-1.079 \cdot 10^{-5}$	$3.025 \cdot 10^{-5}$

Table 4.3.: Covariance matrix of the grand fit.

is displayed in Fig. 4.4. We report the full error covariance matrix in Table 4.3. This fit constitutes our main result.

As a corollary, we provide an updated version of the EQCD phase diagram. The version from [120] does not include continuum-extrapolated critical masses. The intercept of our EQCD fits delivers these critical masses. Additionally, the $x \to 0$ limit

$$xy_{\mathrm{crit}} = \frac{3}{8\pi^2} \tag{4.12}$$

is known perturbatively [120]. We present our data, and this limiting value, in Fig. 4.5. In addition, to guide the eye[3], we include a cubic fit of xy_{crit} as a function of x, displayed by a dashed line. There is quantitative agreement with the phase diagram in [120] at small x, but at large x we find that the prominent bending down of the xy_{crit} curve found by [120] arose because they failed to take a continuum limit.

Kajantie *et. al.* [120] found that the tricritical point occurs at $x = 0.25$, beyond which the phase transition becomes of second order. We have not studied x values larger than $x = 0.2$, so we cannot make any statement about the location of the tricritical point.

As a byproduct our study also produces values for the discontinuity in $\mathrm{Tr}\,\Phi^2$ across the phase transition point, and for the $\mathcal{O}(a)$ additive correction to the $\mathrm{Tr}\,\Phi^2$ operator, which was also not previously known. We postpone these secondary results to Appendix A.2.

[3] In fact we expect nonanalytical behavior as $x \to 0$, due for instance to the two-loop $\Phi^2 \ln(\Phi^2/\mu)$ terms in the effective potential [123] which give rise to $xy_{\mathrm{crit}} - 3/8\pi^2 \sim x \ln(x)$ corrections to Eq. (4.12).

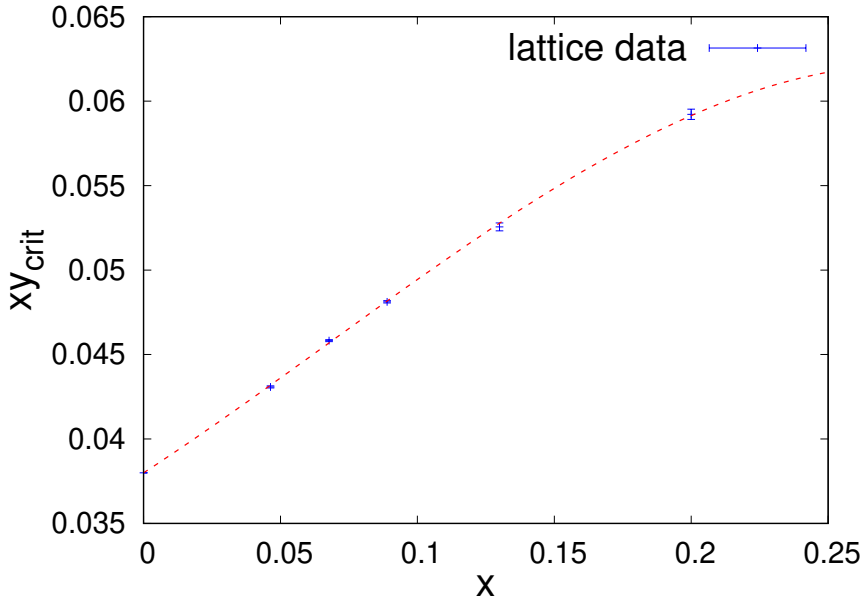

Figure 4.5.: Updated version of the phase diagram of EQCD. The phase below the data points is the $\mathbb{Z}_3$-broken phase, the one above is $\mathbb{Z}_3$-symmetric. The dashed line is a fit to the data points, to help guide the eye.

5. Transverse momentum broadening from lattice EQCD

The lattice-continuum matching in EQCD at $\mathcal{O}(a)$ was completed in the previous chapter. This allows to revisit the exploratory lattice EQCD study of Panero *et. al.* [30], and conduct an extrapolation of $C(b_\perp)$ to the continuum. Since discretization errors occur now only at $\mathcal{O}(a^2)$, this extrapolation is drastically facilitated. Beyond applying the now-complete $\mathcal{O}(a)$-improvement, we develop a systematic fitting procedure to extract $C(b_\perp)$ from fits with advanced fitting techniques.

In Section 5.1, we describe how the Wilson line operator that finally yields $C(b_\perp)$ is implemented on the lattice, making the connection to Section 3.2 and repeating some of the main results presented in that Section for convenience. Moreover, a detailed description of our extrapolation procedure for the length of the Wilson loop to infinity is given in Section 5.1. Section 5.2 presents our continuum extrapolated results for $C(b_\perp)$. Before doing so, the known behavior of $C(b_\perp)$ in two limiting cases is discussed: the area-law for large $b_\perp$ and the perturbative limit for small $b_\perp$. A concluding Section 5.3 preliminarily summarizes the progress made in this and the previous chapter and highlights some details for future investigation, before the actual, overarching discussion takes place in Chap. 6.

This chapter and its appendix A.3 are based on work published in Physical Review D [124]. In order to respect the formulation of the precise arguments and their interpretation originally made, parts of this chapter are adopted from the original publication or slightly paraphrased to fit better in the context of this thesis. The author of this thesis was involved at all stages of this project.

5.1. Computational details

5.1.1. Lattice implementation

The EQCD continuum action was discretized on a three-dimensional spatial lattice, including the now-complete $\mathcal{O}(a)$ corrections to the lattice parameters. The lattice fields are updated using a mixture of heatbath and overrelaxation updates. One full update consists of a sweep over all sites of one heatbath update to each scalar and link, followed by four sweeps in which each scalar and link is updated with over-relaxation. The presence of an adjoint scalar requires an additional accept-reject step be added to the gauge boson updates. Our code involves custom modifications of the openQCD-1.6 codebase [119]. For more details of our lattice implementation, we refer to [116].

The modified Wilson loop (3.2) on the lattice is a local observable which suffers from significantly higher noise levels than volume-averaged observables such as the scalar condensate $\frac{1}{V}\sum_{\boldsymbol{x}} \operatorname{Tr}\Phi^2(\boldsymbol{x})$. This effect is especially strong for loops that enclose large areas, which automatically applies in our case since we would like to extract an observable that requires an extrapolation of $L \to \infty$. An algorithm that was designed to overcome that problem is the multilevel algorithm proposed by Lüscher and Weisz in 2001 [112, 113]. It relies on freezing one or multiple surfaces perpendicular to the Wilson loop and updating the subvolumes separately. This allows to average over the subvolumes independently and measuring the final observable as a correlation of multiple, pre-averaged quantities, which reduces the noise drastically. Originally, this algorithm was designed for pure SU(3) Yang-Mills theory, but it found an application to EQCD, too [30]. We split our lattices along the largest extend N_z in 4 sublattices, on which we perform 80 update sweeps separately before an update sweep through the complete volume is conducted.

Following Panero, Schäfer and Rummukainen [30], the lattice implementation of the modified Wilson loop reads

$$\begin{aligned}
\tilde{W}(L, b_\perp) &= \operatorname{Tr}\left(\tilde{U}_{(0,0);(L,0)} U_{(L,0);(L,b_\perp)} \tilde{U}^{-1}_{(0,b_\perp);(L,b_\perp)} U^\dagger_{(0,0);(0,b_\perp)}\right) \qquad (5.1)\\
\tilde{U}_{x;x+(L,0)} &= \prod_{n=0}^{n_\mathrm{L}-1} U_3\left(x + an\boldsymbol{e}_z\right) \exp\left(-Z\,\Phi(x + a(n+1)\boldsymbol{e}_z)\right)\\
U_{x;x+(0,\boldsymbol{a})} &= \prod_{n=0}^{n_{\boldsymbol{a}}-1} U_1\left(x + an\boldsymbol{e}_x\right)\,,
\end{aligned}$$

where U_i is the standard gauge link in i-direction, the transverse separation is assumed to be $n_{\boldsymbol{b}}$ lattice spacings a in the x-direction $\boldsymbol{b} = n_{\boldsymbol{b}} a \boldsymbol{e}_x$ and Z is the renormalization factor of the Null Wilson line. This quantity was analytically computed to $\mathcal{O}(a)$ in [111]. We repeat their main result for SU(3) explicitly for convenience:

$$\frac{Z^2}{Z_\Phi g_{3\mathrm{d}}^2 a} = 1 + g_{3\mathrm{d}}^2 a \left(\frac{\Sigma}{4\pi} - \frac{3\xi}{\pi} \right) , \tag{5.2}$$

where $g_{3\mathrm{d}}^2 a$ is the dimensionless lattice spacing, Z_Φ is the overall normalization factor of the scalar Φ, which we set $Z_\Phi = 1$ without loss of generality, and $\Sigma = 3.17591153562522$ and $\xi = 0.152859324966$ are standard integrals in the lattice-continuum-matching of EQCD.

When computing a Wilson loop it is often possible to replace each link with its heat-bath average in computing the Wilson loop's value. This is possible so long as no term in the lattice action contains more than one link which appears in the Wilson loop. Therefore we cannot apply this method here, because the scalar field appears in an action term containing the link variable and it also appears in the modified Wilson loop. Similarly, we have not found an efficient way to average over scalar fields, because each scalar field depends on the neighboring scalar fields and because of the quartic term in the action. Therefore the multilevel procedure is the only noise reduction technique we have applied.

5.1.2. Extracting $C(b_\perp)$

The previous section explains how we obtain data for $\tilde{W}(L, b_\perp)$ at multiple lengths L, transverse distances $b_\perp$, and lattice spacings $g_{3\mathrm{d}}^2 a$, each at four "temperatures" (x, y choices). Here we explain how we use this data to extract $C(b_\perp)$. There are three different limits that have to be taken into account properly:

1. infinite volume limit $V \to \infty$
2. infinite length limit $L \to \infty$
3. continuum limit $a \to 0$

Since EQCD possesses a mass gap, the first limit can be easily reached by choosing sufficiently large volumes [125]. The continuum limit is performed by a standard polynomial extrapolation of $g_{3\mathrm{d}}^2 a \to 0$, where the linear term was eliminated by the full $\mathcal{O}(a)$ improvement. So the remaining limit to be treated is the infinite length limit, which we will discuss in the next few paragraphs.

Unfortunately, the information about $C(b_\perp)$ in $\tilde{W}(L, b_\perp)$ is contaminated by (in principle infinitely many) higher states' energies [48]

$$\tilde{W}(L, b_\perp) = c_0 e^{-L\,C(b_\perp)} + \sum_{n=1}^{\infty} c_n e^{-L\,E_n(b_\perp)}\,, \tag{5.3}$$

where c_i are prefactors resulting from the geometry of the Wilson loop and lattice artifacts and are not important for our purpose. Fitting a large number of exponential functions is in general a very hard problem, which gets even worse if the decay constants are numerically close to each other. What saves the day is that the energies are increasingly ordered in n, ie. their exponential decay happens faster at large L as n increases and we are only interested in the lowest energy $C(b_\perp)$. Conversely, the relative error of a Wilson loop $\tilde{W}(L, b_\perp)$ scales inversely with the enclosed area, so small loops feature good statistics. It is crucial to find a regime in which the balance between sufficiently small Monte Carlo errors and sufficiently large L for small contamination is maintained. In our case, $g_{3\mathrm{d}}^2 L \geq 1.0$ fulfilled that requirement such that it is sufficient to consider only one higher state. Thus, the fit function for the $L \to \infty$ extrapolation reads

$$\tilde{W}(L, b_\perp) = c_0 e^{-L\,C(b_\perp)} + c_1 e^{-L\,E_1(b_\perp)}\,. \tag{5.4}$$

Exponential fits of this form are in general very unstable. There are a few techniques one can apply to improve that, however. Firstly, one can estimate starting values close to the final fit values, for which a procedure was outlined in [126]. The second method we apply is the so-called variable projection [127]. Roughly speaking, one gives up on determining the c_i's and finds the minimum of χ^2 in the reduced parameter space, only. In our case, this is an appropriate procedure since we are not interested in the values of the c_i's, anyway.

As a last obstacle, we determine our data for all $\tilde{W}(L, b_\perp)$ at a given lattice spacing from the same ensemble, which means that our data is highly correlated, not only along the Monte Carlo time axis, but also for the different L and $b_\perp$. The correlation along the Monte Carlo time axis can be eliminated by binning the data; the bin size has to be varied until a plateau for the errors is reached. The correlation of different lengths is taken care of by performing correlated, variable-projected fits [70, 127]. Last but not least, the correlation for the final, continuum-extrapolated different $b_\perp$ is less severe than the one for the different lengths since multiple lattice spacings (ensembles) contribute to the continuum-extrapolated points of $C(b_\perp)$. Nevertheless, we report the covariance matrices for all $C(b_\perp)$ at our four temperatures in App. A.3.

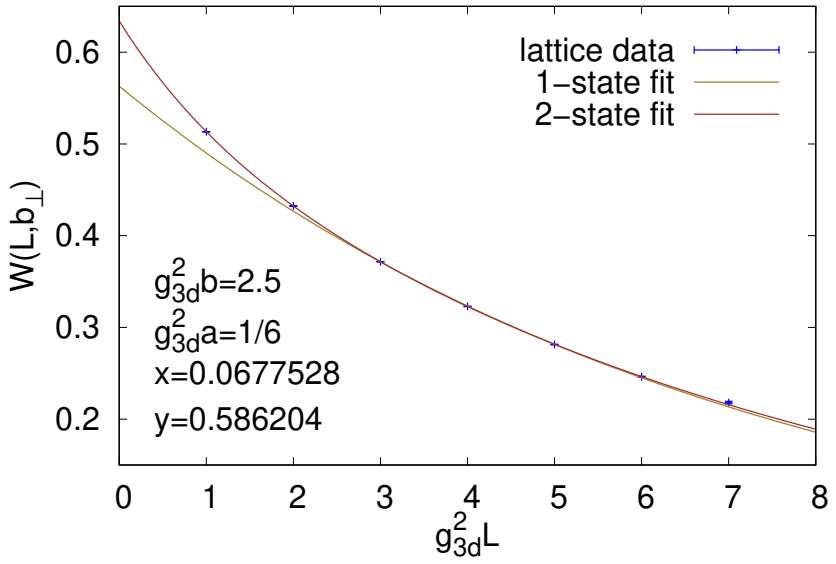

Figure 5.1.: Genuine $L \to \infty$ fit for $g_{3\mathrm{d}}^2 b_\perp = 2.5$ at $g_{3\mathrm{d}}^2 a = 1/6$ and $x = 0.0677528$. Note that this figure only illustrates the initial guess finding. The actual values extracted from the data by the variable projection cannot be displayed, since this procedure does not give values for the c_i's. However, we found that the final results from the variable projection were very close to the initial ones determined as in the plot.

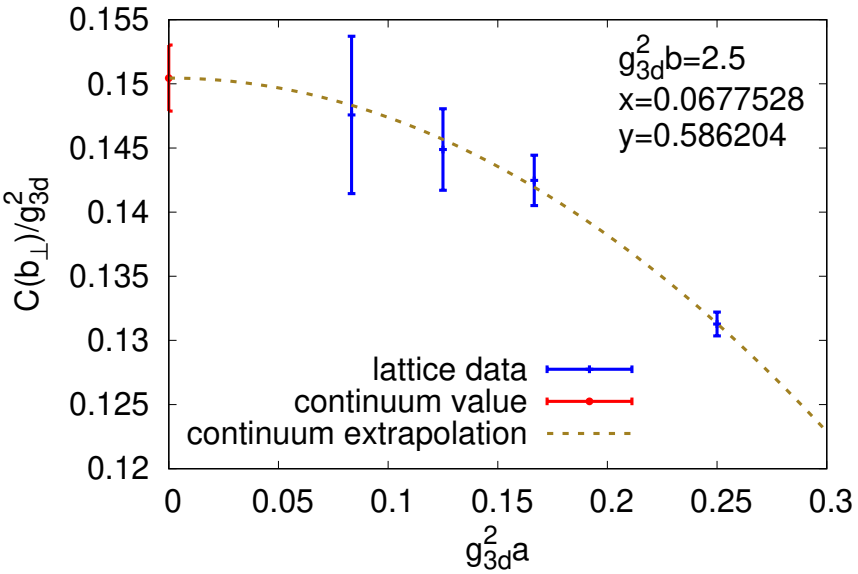

Figure 5.2.: Genuine continuum extrapolation for $g_{3\mathrm{d}}^2 b_\perp = 2.5$ at $x = 0.0677528$.

This data can now be extracted at various lattice spacings and extrapolated to the continuum, cf. Fig. 5.2. We choose the lattice spacings such that a quadratic interpolation is sufficient. Since the linear term is eliminated by the full $\mathcal{O}(a)$ improvement, all continuum extrapolations are fits with only two free parameters, improving the error of the extrapolated value drastically. The shape of the extrapolation fit in Fig. 5.2 is clearly quadratic, confirming that our improvement procedure succeeded in eliminating all linear-in-a renormalizations and rescalings.

5.2. Results

5.2.1. Analytical expectations: small $b_\perp$

Before presenting numerical results, we should start by asking, what answers do we expect? Of course we don't know what the behavior of $C(b_\perp)$ should be, otherwise there

would be no need to measure it nonperturbatively on the lattice. But in limiting regimes, namely $g_{3\mathrm{d}}^2 b_\perp \ll 1$ and $g_{3\mathrm{d}}^2 b_\perp \gg 1$, we might expect simpler behavior.

Let us start with $g_{3\mathrm{d}}^2 b_\perp \ll 1$. First note that $C(b_\perp)$ has the same units as energy. To see this note that the log trace of a Wilson loop is dimensionless, so Eq. (3.2) shows that $C(b_\perp)$ has units of inverse length or energy. Alternately, $C(q_\perp)$ describes a probability per unit length and momentum-squared, and so has units of inverse energy. Fourier transforming $\int \mathrm{d}^2 q_\perp$ introduces two factors of energy, making $C(b_\perp)$ linear in energy. Next, note that both $g_{3\mathrm{d}}^2$ and m_D have units of energy. Perturbation theory is an expansion in $g_{3\mathrm{d}}^2$, but since this quantity is dimensionful it should be balanced by powers of something else with dimensions; hence we have an expansion in $g_{3\mathrm{d}}^2 b_\perp$ and/or in $g_{3\mathrm{d}}^2/m_\mathrm{D}$. Therefore we formally expect that the small-$b_\perp$ expansion, as an expansion in loop order, is of form

$$\begin{array}{lllll} C(b_\perp) \sim & g_{3\mathrm{d}}^2 & + g_{3\mathrm{d}}^2 b_\perp m_\mathrm{D} & + g_{3\mathrm{d}}^2 b_\perp^2 m_\mathrm{D}^2 & + \mathcal{O}(b_\perp^3) \quad \text{LO} \\ & & + g_{3\mathrm{d}}^4 b_\perp & + g_{3\mathrm{d}}^4 b_\perp^2 m_\mathrm{D} & + \mathcal{O}(b_\perp^3) \quad \text{NLO} \\ & & & + g_{3\mathrm{d}}^6 b_\perp^2 & + \mathcal{O}(b_\perp^3) \quad \text{NNLO}\,. \end{array} \tag{5.5}$$

If we were computing the standard Wilson loop, the first two leading-order terms might arise; but for the structure we do consider, there are cancellations at leading order between A_z and Φ contributions, precisely because Φ couples in an antihermitian way. Since the Φ field is heavy, the cancellation is incomplete and the $g_{3\mathrm{d}}^2 b_\perp^2 m_\mathrm{D}^2$ term is present, but the $g_{3\mathrm{d}}^2$ and $g_{3\mathrm{d}}^2 b_\perp m_\mathrm{D}$ terms are absent. In particular, the leading short-distance contribution is [110]

$$C(b_\perp)_\mathrm{LO} = \frac{g_{3\mathrm{d}}^2}{6\pi}\left(1 - \gamma_\mathrm{E} + \ln(2) - \ln(b_\perp m_\mathrm{D})\right) m_\mathrm{D}^2 b_\perp^2 + \mathcal{O}(b_\perp^4 \ln(b_\perp))\,, \tag{5.6}$$

which as expected scales as $g_{3\mathrm{d}}^2 m_\mathrm{D}^2 b_\perp^2$. Note that a quadratic term in $C(b_\perp)$ can be understood, using Eq. (2.47), as $C(b_\perp) \simeq \frac{\hat{q}}{4} b_\perp^2$ (see [33] Appendix C). Therefore the logarithmic term here represents a log UV divergence in the Coulombic value of $\hat{q}$, which is well known. Also note that the dominant momentum region giving rise to Eq. (5.6) is $q_\perp \sim m_\mathrm{D}$, since this is the momentum region where the cancellation between A_z and Φ first breaks down. The momentum region $q_\perp \sim g_{3\mathrm{d}}^2$ gives rise to an $\mathcal{O}(g_{3\mathrm{d}}^6 b_\perp^2)$ contribution, which therefore indicates the order where nonperturbative physics will enter.

At NLO the full $b_\perp m_\mathrm{D}$ dependence has been worked out in Ref. [33], based on $q_\perp$-space results from [29]. They find

$$C(b_\perp)_\mathrm{NLO} = C(b_\perp)_\mathrm{LO} - \frac{g_{3\mathrm{d}}^4 b_\perp}{8\pi} + \frac{3\pi^2 + 10 - 4\ln 2}{32\pi^2} g_{3\mathrm{d}}^4 m_\mathrm{D} b_\perp^2 + \mathcal{O}(g_{3\mathrm{d}}^4 {m_\mathrm{D}}^2 b_\perp^3)\,. \tag{5.7}$$

The linear term is the only term linear in $b_\perp$ which will arise, and is therefore a clean prediction of perturbation theory. The second term is formally suppressed relative to the LO expression by a factor $\sim g_{\rm 3d}^2/m_{\rm D}$, indicating that in this region, perturbation theory is an expansion in $(g_{\rm 3d}^2/m_{\rm D}) \sim y^{-1/2}$. Similarly, the unknown NNLO contribution is of order $g_{\rm 3d}^6 b_\perp^2$. Unfortunately a 2-loop calculation would not be sufficient to determine this term, since as we already discussed, this is the order where perturbation theory for this quantity breaks down due to IR divergences; all higher loop orders also contribute at this order, so the $g_{\rm 3d}^6 b_\perp^2$ coefficient is nonperturbative. This unknown nonperturbative entry is suppressed, with respect to the leading-order result, by a factor of y^{-1}. Therefore, the highest-temperature case we consider, with $y = 1.65$, should show reasonable convergence and the two known perturbative terms should be relatively close to determining the true linear plus quadratic behavior at small $b_\perp$. But for the other values we consider, perturbative results for the $b_\perp^2$ coefficient will not be useful and this coefficient (and therefore $\hat{q}$) has to be fitted. However the $b_\perp$ and $b_\perp^2 \ln(b_\perp m_{\rm D})$ terms are clean predictions of perturbation theory.

5.2.2. Analytical expectations: large $b_\perp$

The large $b_\perp$ region has been discussed by [30], who argue that $g_{\rm 3d}^2 b_\perp \gg 1$ corresponds to the region where Wilson loops display area-law behavior. The Φ field correlator essentially vanishes between opposite edges of the Wilson line and does not contribute to the $b_\perp$ dependence in this regime; therefore we expect

$$C(b_\perp) \simeq \sigma_{\rm EQCD}\, b_\perp \,, \tag{5.8}$$

where $\sigma_{\rm EQCD} \propto g_{\rm 3d}^4$ is the EQCD string tension. The EQCD string tension was predicted in [77], continuing the continuum-extrapolated result of three-dimensional pure gauge theory [128], ie. magnetostatic QCD (MQCD) to EQCD

$$\frac{\sqrt{\sigma_{\rm EQCD}}}{g_{\rm 3d}^2} = \left[1 - \frac{1}{48}\frac{3}{\pi\sqrt{y}} - \frac{17}{4608}\left(\frac{3}{\pi\sqrt{y}}\right)^2\right] \times 0.553(1)\,, \tag{5.9}$$

applying the 2-loop perturbative matching between EQCD and MQCD from [129]. However, this calculation relies on a perturbative matching of the MQCD coupling to its EQCD equivalent, which is again a formal expansion in $1/\sqrt{y}$ which may not show good convergence.

5.2.3. Numerical results

Subsection 5.1.2 has already described how we extract $W(L, b_\perp)$ values at each lattice spacing, and how we extrapolate these to the large L and small $g_{3\mathrm{d}}^2 a$ limits. Doing so, we find the results tabulated in Table 5.1 and displayed in Fig. 5.3. These represent our principal findings.

$g_{3\mathrm{d}}^2 b_\perp$	$x_{\mathrm{cont}} = 0.08896$ $y_{\mathrm{cont}} = 0.452423$ $\frac{C(b_\perp)}{g_{3\mathrm{d}}^2}\Big\vert_{250\ \mathrm{MeV}}^{N_\mathrm{f}=3}$	$x_{\mathrm{cont}} = 0.0677528$ $y_{\mathrm{cont}} = 0.586204$ $\frac{C(b_\perp)}{g_{3\mathrm{d}}^2}\Big\vert_{500\ \mathrm{MeV}}^{N_\mathrm{f}=3}$	$x_{\mathrm{cont}} = 0.0463597$ $y_{\mathrm{cont}} = 0.823449$ $\frac{C(b_\perp)}{g_{3\mathrm{d}}^2}\Big\vert_{1\ \mathrm{GeV}}^{N_\mathrm{f}=4}$	$x_{\mathrm{cont}} = 0.0178626$ $y_{\mathrm{cont}} = 1.64668$ $\frac{C(b_\perp)}{g_{3\mathrm{d}}^2}\Big\vert_{100\ \mathrm{GeV}}^{N_\mathrm{f}=5}$
0.125	$-0.0058(44)$	-	-	$-0.005(19)$
0.25	$-0.0091(36)$	$-0.0130(36)$	$-0.0094(34)$	$0.003(32)$
0.5	$-0.01154(63)$	$-0.00394(87)$	$0.00599(58)$	$0.03166(49)$
0.75	$0.0000(11)$	$0.0128(17)$	$0.0337(10)$	$0.07904(81)$
1.0	$0.00623(82)$	$0.03313(61)$	$0.06366(36)$	$0.12649(33)$
1.5	$0.0606(17)$	$0.1055(11)$	$0.15803(94)$	$0.25599(62)$
2.0	$0.1269(33)$	$0.2002(28)$	$0.2712(18)$	$0.3986(12)$
2.5	$0.2150(41)$	$0.3009(51)$	$0.3947(32)$	$0.5518(22)$
3.0	$0.3114(86)$	$0.4164(46)$	$0.5234(67)$	$0.7048(45)$
4.0	$0.435(42)$	$0.643(33)$	$0.790(28)$	$1.053(17)$
5.0	$0.726(94)$	$0.941(96)$	$1.02(10)$	$1.314(13)$
6.0	$1.21(11)$	$1.35(10)$	$1.60(15)$	$1.700(36)$
$\hat{q}/g_{3\mathrm{d}}^6$	$0.1847(78)$	$0.230(10)$	$0.3637(60)$	$0.6424(47)$
$\sigma_{\mathrm{EQCD}}/g_{3\mathrm{d}}^4$	$0.2836(10)$	$0.2867(10)$	$0.2901(11)$	$0.2952(11)$

Table 5.1.: Results for $C(b_\perp)$ for four temperatures and a range of transverse separations. All data points are continuum extrapolated, with errors representing all statistical and systematic errors associated with the data extraction and extrapolations, except for the first (smallest $g_{3\mathrm{d}}^2 b_\perp$) entry in each column; see text. We also quote the extracted value of $\hat{q}$ and the string tension as determined in [77], see text.[1]

Note that every result in Table 5.1 is based on data from at least three lattice spacings, extrapolated to the continuum – *except* for the first (smallest-separation) data point in each column, see Table A.5 in the appendix. This point is based on a single lattice spacing. Analyzing the lattice-spacing dependence of the points where we can perform a continuum extrapolation, we find that the a^2 coefficient is fairly constant for small $b_\perp$; so we assume that the same a^2 extrapolation coefficient applies for this smallest-$b_\perp$ point

[1] In an earlier version of this paper, a numerical mistake in our fitting procedure caused our results to be too small by a factor of $1/2$.

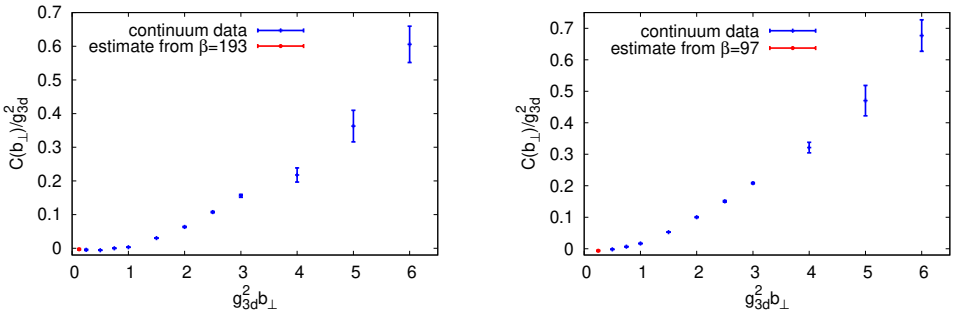

(a) $x = 0.08896$

(b) $x = 0.0677528$

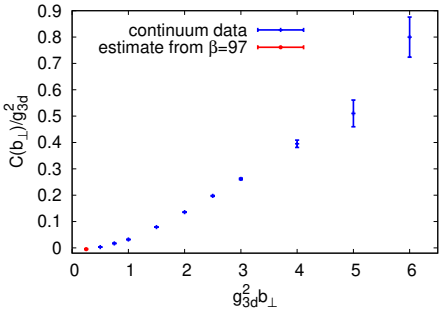

(c) $x = 0.0463597$

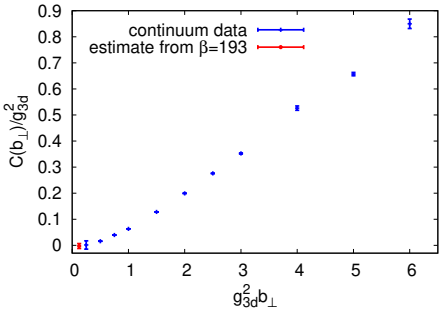

(d) $x = 0.0178626$

Figure 5.3.: $C(b_\perp)$ for different x. The blue points are based on continuum extrapolations; the red points are from a single lattice spacing, as described in the text.

as for the next-smallest $b_\perp$ data, and assign 100% systematic errors to this estimate. We then combine this (systematic) error with the statistical error in quadrature.

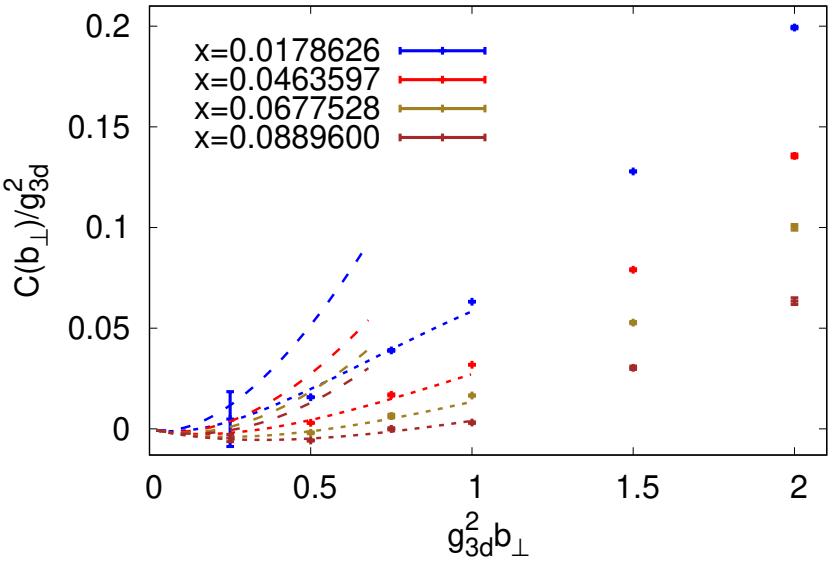

Figure 5.4.: Comparison of $C(b_\perp)$ for different x at small $g_{3\mathrm{d}}^2 b_\perp$. The long dashed lines mark the perturbative results for $C(b_\perp)$ at NLO, Eq. (5.7). The short dashed lines mark a quadratic fit to the datapoints satisfying $g_{3\mathrm{d}}^2 b_\perp \leq 0.75$, see text.

Let us examine the small $b_\perp$ region in more detail. As we saw in Subsection 5.2.1, we expect that $C(b_\perp)$ scales, for small $b_\perp$, as

$$g_{3\mathrm{d}}^2 b_\perp \ll 1 \text{ limit of } C(b_\perp) = -\frac{g_{3\mathrm{d}}^4}{8\pi} b_\perp - \frac{g_{3\mathrm{d}}^2}{6\pi} \ln(b_\perp m_{\mathrm{D}}) m_{\mathrm{D}}^2 b_\perp^2 + \frac{\hat{q}}{4} b_\perp^2 + \mathcal{O}(b_\perp^3). \quad (5.10)$$

Figure 5.4 plots the small $b_\perp$ data with two fits. The long-dashed curves are based on assuming that $\hat{q}$ is determined by the NLO expression presented in Eq. (5.7) – that is, neglecting the (nonperturbative) $g_{3\mathrm{d}}^6$ corrections. The dashed curves represent a fit of the data, using all data points with $g_{3\mathrm{d}}^2 b_\perp \leq 0.75$, to the functional form shown in Eq. (5.10), treating $\hat{q}$ as a free fitting coefficient and neglecting $\mathcal{O}(b_\perp^3)$ effects (a one-parameter fit). The resulting value for $\hat{q}$ (which, note, is corrected by the $\ln(b_\perp m_{\mathrm{D}})$ term), appears as an added line of Table 5.1. For the smallest three temperatures, this result is about a factor of 2 smaller than the NLO result, indicating that in these cases the next correction is not small. However, the deviation at the largest temperature shrinks to a factor of 1.3.

Recall that this was the only scenario in which $y \gg 1$ is actually fulfilled and convergence of the perturbative series in $1/\sqrt{y}$ is not hopeless. Even better agreement is expected at larger temperatures, where the first few orders in the perturbative expansion should show convergent behavior.

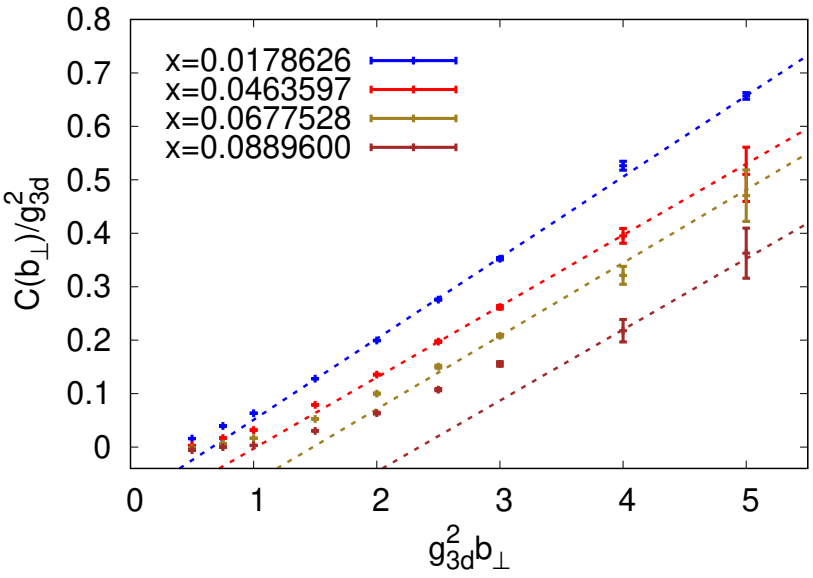

Figure 5.5.: Large $b_\perp$ behavior of $C(b_\perp)$, compared to straight-line asymptotics based on the string tension (see text).

Finally, we consider the large $b_\perp$ asymptotics. As discussed, one expects $C(b_\perp)$ at large $b_\perp$ to rise linearly, with a coefficient which equals the string tension. We list the string tension of EQCD in the last separated line of Tab 5.1, determined by Laine and Schröder by perturbatively promoting the MQCD results of Teper [128] to full EQCD [77]. Just as in the small $g_{3\mathrm{d}}^2 b_\perp$-region, a series expansion in $1/\sqrt{y}$ is involved, although this particular one seems to be a little bit more robust than the one for $\hat{q}$.[2] The figure shows that the large-$b_\perp$ asymptotics are indeed well described by the string tension in EQCD. The range over which this linear behavior holds is larger for the high-temperature (small-x, large-y) case, where the scalar decouples over a shorter distance. For our highest-temperature

[2] It is perhaps not surprising that the perturbative series in $\sqrt{y}$ works better for the string tension than for $\hat{q}$. First, the string tension is determined solely by the gauge (magnetic) degrees of freedom, while $\hat{q}$ involves both electric and magnetic fields. Second, there is already nonperturbative input in σ, from solving the gauge sector, while our information about $\hat{q}$ is only the short-distance perturbative contribution.

case we find nearly linear behavior already close to $g_{3\mathrm{d}}^2 b_\perp \simeq 1$. For the lowest temperature, on the other hand, the scalar is very light and its effects persist to larger distances; here it takes until approximately $g_{3\mathrm{d}}^2 b_\perp \simeq 4$ before the asymptotic behavior sets in. Due to the late set-in at the smallest temperature and the large statistical errors of the corresponding data points, we cannot really confirm the prediction of Eq. (5.9) here, even though the qualitative behavior, namely a linear asymptotic form, is nevertheless displayed by our data. For the three higher temperatures, we find that the predicted value for the string tension fits our data very well.

5.3. Conclusion and outlook

The collision kernel $C(b_\perp)$ contains essential information about how a thermal medium transverse-broadens, and therefore damps, high energy particles. Its perturbatively ill-behaved infrared contributions can be computed within the effective theory EQCD by formulating the collision kernel in terms of EQCD variables [29] and computing them on the lattice [30]. We have presented the first such lattice analysis of $C(b_\perp)$ which is complete in the sense that it uses all lattice-continuum improvements and makes a complete extrapolation to the continuum limit. Our approach profited from the use of the multilevel algorithm for noise reduction and the variable projection method for fitting to the long Wilson-loop limit. The use of fully improved lattice-continuum matching and operator definitions accelerated the continuum limit, leading to high precision continuum-extrapolated results.

Our results indicate a rather large downward correction in the value of $\hat{q}$ relative to the NLO result at temperatures which are in the region of a few hundred MeV to several GeV; indeed, we find a $\hat{q}$ value which is closer to the leading-order result. This has implications for jet quenching and for transport coefficients, which are also sensitive to $\hat{q}$. However we want to emphasize here that the reader should not dwell on the value of $\hat{q}$ itself, which is a crude fit to a few small-$b_\perp$ points. Rather, interested practitioners should directly use $C(b_\perp)$, which is the potential, in the transverse plane, which is relevant for driving decoherence within Zakharov's spacetime picture of jet quenching [23–25, 130].

Another interesting feature of our result is that the value of the kernel $C(b_\perp)$ is actually negative for sufficiently small $g_{3\mathrm{d}}^2 b_\perp$ values. This behavior is both expected and confusing. In Ref. [33] it is shown that $C(b_\perp)$ should have a small-$b_\perp$ expansion displaying a leading negative, linear-in-$b_\perp$ behavior. A negative value of $C(b_\perp)$ does not have a sensible probabilistic interpretation; but this negative linear term can only dominate the result

for $b_\perp \sim g_{3\mathrm{d}}^2/m_{\mathrm{D}}^2$, which is formally $\mathcal{O}(1/T)$. This is exactly the short-distance regime where EQCD breaks down as an effective description of thermal QCD. Unfortunately, short distance, which corresponds to high transverse momentum, is relevant for the highest-energy splitting processes, which may be physically important in the medium-modification of high energy jets. Therefore our results need to be supplemented with a matching calculation between the value of $C(b_\perp)$ in EQCD and in full QCD. Most of the steps in this matching procedure have already been taken [27, 29, 131]. A complete leading-order matching will allow our results to be correctly incorporated into jet-quenching calculations. A higher-order analysis would shed more light into the role of collinear effects, which are expected to enter at the NNLO level but should be enhanced by double logarithms [132] and may involve more complex structures than the Wilson loop considered here [133, 134]. We leave this, and an application of our results to the computation of jet modification, for future work.

6. Conclusion

A major effort in modern physics has been put into theoretically describing the strong nuclear force. To the best of our knowledge, this description is Quantum Chromodynamics, a theory dealing with quarks and gluons as fundamental degrees of freedom. Usually, neither quarks nor gluons can be observed separately due to confinement. In the Quark-Gluon-Plasma, confinement is overcome and one can investigate how the strong nuclear force acts over comparatively large length scales. Large theoretical efforts have been put in predicting material properties of the QGP, for instance the shear viscosity or the thermal photon emission rate. Another property of the QGP to probe is its interaction with traversing high-energy particles, encoded into the transverse collision kernel $C(b_\perp)$.

Calculations of $C(b_\perp)$ have been predominantly perturbative to date. An efficient way of organizing such calculations was shown by Caron-Huot: Quantizing the system along the light cone allows the separation of treating hard contributions in standard perturbation theory and the soft contributions in Electrostatic QCD, a high-temperature effective field theory of QCD. Even though Caron-Huot also demonstrated that purely perturbative predictions for the soft $C(b_\perp)$ cannot be trusted up to next-to-leading order in the strong coupling g^2, these results keep being used in practice in jet phenomenology. A way out was stated by Panero *et. al.*; a computation of $C(b_\perp)$ in EQCD discretized on a spatial lattice was proven to be possible and likely to deliver meaningful theoretical results. However, the authors of this study were not able to extrapolate away the systematic discretization error introduced by a finite lattice spacing a.

The present thesis completed this journey; after entirely removing discretization errors at $\mathcal{O}(a)$, see Chap. 4, a comprehensive calculation of $C(b_\perp)$, see Chap. 5, on the lattice was undertaken, and an extrapolation of the lattice spacing to 0 ensured the absence discretization effects.

The lattice-continuum matching at $\mathcal{O}(a)$ has been known for EQCD since 1997, except the $\mathcal{O}(a)$-correction for the lattice-version of the EQCD screening mass y. An analytical

calculation of the $\mathcal{O}(a)$ errors in y would have required the evaluation of three-loop-diagrams in lattice perturbation theory, and was therefore prohibited by sheer complexity. However, the authors found a way to circumvent this analytical computation by fitting the otherwise-fully-$\mathcal{O}(a)$-improved masses on lattices with different spacings to a line of constant physics. This line of constant physics was provided by the critical masses of the EQCD phase transition. Repeating this procedure at multiple different values of the EQCD self-coupling x allowed a grand fit of the missing $\mathcal{O}(a)$ correction to y to its known functional form, a cubic polynomial in x. Having completed the elimination of $\mathcal{O}(a)$-errors in lattice EQCD, continuum extrapolations did not need to contain a term linear in a any more, the precision at constant numerical effort improved drastically.

This brought us considerably closer to our original goal, the computation of the soft part of $C(b_\perp)$ on the lattice and its extrapolation to the continuum. To this end, a rigorous scheme of extracting $C(b_\perp)$ from modified Wilson loops was developed for the first time. In this scheme the coefficient of the lowest lying state in a tower of exponential excitations was determined via correlated, variable-projected fits. The signal-to-noise ratio of the simulation data was improved beforehand using the multilevel algorithm. Eventually, continuum-extrapolated results for $C(b_\perp)$ were obtained, corresponding to full QCD at four different temperatures. Our results connected to the two analytically known limiting cases. A linear growth in $b_\perp$, as predicted by the EQCD area law, set in at large $b_\perp$, its string tension matched previously predicted results. At small $b_\perp$, we found agreement with perturbative EQCD results, the predicted negative linear slope could be observed, making $C(b_\perp)$ negative at very small $b_\perp$. Despite the agreement of the linear terms, fitting a quadratic in $b_\perp$ delivered a value for the jet-broadening coefficient $\hat{q}$ that was substantially lower than the NLO perturbative prediction, where the deviation shrank with increasing temperature. This deviation originated from intrinsically non-perturbative corrections to $\hat{q}$ at next-to-next-to-leading-order which were not sufficiently suppressed at the investigated temperatures. The window of $b_\perp$-values outside these two limiting ranges diminished as we went to higher temperatures, until at $T = 100\ \mathrm{GeV}$, it almost vanished.

Interpreting $C(b_\perp)$ as a rate naturally prohibits seemingly negative results as observed for very small $b_\perp$. What saves the day is that , especially at small $b_\perp$, our EQCD lattice-version has to be supplied with the perturbatively known hard contributions in (3.8) as proposed by Ghiglieri and HyungJoo in [131]. From these arises a linear term with precisely the opposite sign that cancels the negative linear term in our $C(b_\perp)$. Other than executing a potentially numerical Fourier transform, this matching calculation should not pose problems. Our new $C(b_\perp)$, supplied with the hard contribution, is the first coherent determination of this quantity. Persisting errors are due to the perturbative matching to EQCD in the soft sector and due to the truncation of the perturbative series in the

hard sector. The strict power counting in g is common to both cases, therefore a rigorous estimation of the error is possible. A calculation of jet splitting rates using (2.48) could serve as a benchmark of the new state-of-the-art-$C(b_\perp)$. We expect our result to help achieving a drastic improvement in the theoretical prediction of these rates.

Another interesting direction of future research is the determination of asymptotic jet masses from EQCD. The jet-medium-interaction induces a contribution that can be treated as an effective mass of the jet [135]. These can be calculated non-perturbatively from the EQCD correlators specified in App. B of [33]. Eventually, the correlators have to be integrated over $\int_0^\infty \mathrm{d}z\, z \ldots$. Methodologically, this project resembles the extraction of $C(b_\perp)$ from Wilson loops a lot, also, the lattice implementation is similar to a very high extent. Asymptotic masses are the other source of non-perturbative effects in jet-medium interactions.

Further in the future, the non-perturbative information in $C(b_\perp)$ can be used to supply existing perturbative calculations of QGP shear viscosity, quark diffusion rate, or thermal photon emission rate [32, 33] and hopefully increase the convergence of these, such that meaningful results can be obtained also at temperatures accessible at today's collider facilities.

A. Appendix

A.1. Algorithm for pure scalar case

The large-x limit of EQCD is the same as the $g_{3\mathrm{d}}^2 \to 0$ limit (provided we work in terms of $\tilde{y} \equiv y/x^2 = m^2/\lambda^2$ and track the lattice spacing in terms of $\lambda a = g_{3\mathrm{d}}^2 a\, x$). In this limit, we have an 8 (real) component scalar theory with an $\mathcal{O}(8)$ symmetry and a second-order phase transition where this symmetry is spontaneously broken to $\mathcal{O}(7)$. The x^3 term in the scalar mass renormalization of EQCD arises purely from scalar diagrams which are identical to those in this theory; therefore we can determine this coefficient by studying the $\mathcal{O}(\lambda a)$ corrections to $\tilde{y}$ in this scalar field theory.

A natural approach would be to use, as a line of constant physics, the 2'nd order phase transition point. However this would face the usual problems of critical slowing down and the inaccuracy of establishing the exact transition point. So we choose instead to compare $\tilde{y}$ between different lattice spacings by finding the *pseudo*critical value where the theory in a specific physical volume encounters a specific pseudocritical criterion. We choose the volume to be $\lambda L = 8$ and select as the pseudocritical condition that the 4th order Binder cumulant [136]

$$\mathcal{B} \equiv \frac{\left\langle \left(\mathrm{Tr}\, \bar{\Phi}^2\right)^2 \right\rangle}{\langle \mathrm{Tr}\, \bar{\Phi}^2 \rangle^2}\,, \tag{A.1}$$

where $\bar{\Phi} \equiv \frac{1}{N^3} \sum_{\boldsymbol{x}} \Phi_{\mathrm{L}}(\boldsymbol{x})$, takes the value $\mathcal{B}_{\mathrm{pc}} = 1.073$. Because the Binder cumulant is dominated by infrared physics and is insensitive to the lattice spacing up to subleading corrections and renormalization effects (which are what we want to study), this should occur at the same *physical* y value at every lattice spacing up to $\mathcal{O}(a^2)$ or higher corrections. Our set of simulation parameters can be found in Table A.1. The results already appeared in the last panel of Fig. 4.3.

λa	$N_\mathrm{x} N_\mathrm{y} N_\mathrm{z}$	total statistics
$1/2$	16^3	402900
$1/3$	24^3	1490120
$1/4$	32^3	2487440
$1/6$	48^3	2931750
$1/8$	64^3	2513280

Table A.1.: Simulation parameters for the pure scalar simulation.

A.2. EQCD simulation parameters and phase transition properties

A.2.1. Parameters and table

In Table A.2, we provide parameters and direct results of our EQCD simulations as well as values for $\mathrm{Tr}\,\Phi^2$ in both phases at criticality. We converted $\mathrm{Tr}\,\Phi^2_{\mathrm{L,crit}} \to \frac{\mathrm{Tr}\,\Phi^2_{\mathrm{crit,cont}}}{g^2_{\mathrm{3d}}}$, where we display the latter in the table, via all known contributions up to $\mathcal{O}(g^2_{\mathrm{3d}}a)$ in Eq. (A.4) [114]. For the sake of readability, we will refer to $\frac{\mathrm{Tr}\,\Phi^2_{\mathrm{crit,cont}}}{g^2_{\mathrm{3d}}}$ as $\frac{\mathrm{Tr}\,\Phi^2}{g^2_{\mathrm{3d}}}$ in the following. The raw data was obtained in separate simulations with $V = N_\mathrm{x}^3$. We ensured that the Monte-Carlo error of the separate simulations dominates the overall error of $\frac{\mathrm{Tr}\,\Phi^2}{g^2_{\mathrm{3d}}}$, not the uncertainty of y_{crit}. The slightly negative values of $\frac{\mathrm{Tr}\,\Phi^2_{\mathrm{symm}}}{g^2_{\mathrm{3d}}}$ for small x are expected and arise because the positive mass-squared at the transition point suppresses IR fluctuations, while the renormalization involves subtracting off large positive counterterms (including the massless, free-theory fluctuations).

A.2.2. Transition strength

With the critical values of $\frac{\mathrm{Tr}\,\Phi^2}{g^2_{\mathrm{3d}}}$ in both phases from Table A.2 in hand, we can infer further interesting features of the first order phase transition. Having several values of $\frac{\mathrm{Tr}\,\Phi^2}{g^2_{\mathrm{3d}}}$ at the same physical x and different lattice spacings $g^2_{\mathrm{3d}}a$, we extrapolate both the difference between phases $\frac{\Delta\mathrm{Tr}\,\Phi^2}{g^2_{\mathrm{3d}}}$ and the symmetric phase value $\frac{\mathrm{Tr}\,\Phi^2_{\mathrm{symm}}}{g^2_{\mathrm{3d}}}$ to the continuum. We

$g_{3d}^2 a$	x_{cont}	$N_x N_y N_z$	$y_{crit,cont}$	statistics y_{crit}	$\mathrm{Tr}\,\Phi^2_{brok}/g^2_{3d}$	$\mathrm{Tr}\,\Phi^2_{symm}/g^2_{3d}$
1/6	0.0463597	$72^2 \times 192$	0.824773(45)	300690	14.0477(40)	−0.22234(28)
1/8	0.0463597	$96^2 \times 256$	0.855935(85)	373030	15.4237(89)	−0.23064(43)
1/12	0.0463597	$144^2 \times 384$	0.88387(28)	37170	17.716(12)	−0.23390(77)
1/16	0.0463597	$192^2 \times 512$	0.89504(62)	1300	17.714(14)	−0.23748(74)
1/24	0.0463597	$192^2 \times 512$	0.9072(21)	1430	17.585(57)	−0.2355(17) [1]
1/4	0.0677528	$48^2 \times 128$	0.59100(19)	13110	6.7502(59)	−0.11392(62)
1/6	0.0677528	$72^2 \times 192$	0.62149(12)	150000	7.6155(72)	−0.12043(55)
1/8	0.0677528	$96^2 \times 256$	0.63661(11)	200000	7.960(14)	−0.12101(78)
1/12	0.0677528	$144^2 \times 384$	0.64963(29)	38990	8.287(15)	−0.12400(80)
1/16	0.0677528	$192^2 \times 512$	0.6546(11)	1910	8.4103(61)	−0.1228(12)
1/3	0.08896	$36^2 \times 96$	0.47232(24)	10000	4.0728(22)	−0.03277(47)
1/4	0.08896	$48^2 \times 128$	0.49119(14)	100000	4.4343(53)	−0.03489(59)
1/6	0.08896	$72^2 \times 192$	0.50940(15)	150000	4.7728(35)	−0.0344(10)
1/8	0.08896	$96^2 \times 256$	0.51736(20)	97500	4.9249(58)	−0.0336(11)
1/12	0.08896	$144^2 \times 384$	0.52565(45)	44530	5.052(10)	−0.0321(13)
1/3	0.13	$36^2 \times 96$	0.37184(94)	10000	2.3337(64)	0.1112(15)
1/4	0.13	$48^2 \times 128$	0.38341(83)	100000	2.3899(64)	0.1126(19)
1/6	0.13	$72^2 \times 192$	0.39323(21)	150000	2.4703(75)	0.1190(38)
1/8	0.13	$96^2 \times 256$	0.39702(31)	109230	2.5371(82)	0.1246(39)
1/12	0.13	$144^2 \times 384$	0.3982(11)	120600	2.618(13)	0.1332(65)
1/3	0.2	$36^2 \times 96$	0.27743(41)	12340	1.3115(74)	0.578(32)
1/4	0.2	$48^2 \times 128$	0.28595(34)	21030	1.283(13)	0.630(34)
1/6	0.2	$72^2 \times 192$	0.29214(37)	66160	1.2850(81)	0.650(24)
1/8	0.2	$96^2 \times 256$	0.29377(48)	122080	1.323(11)	0.713(37)
1/12	0.2	$144^2 \times 384$	0.29393(97)	3330	1.390(14)	0.707(26)

Table A.2.: Parameters and results of EQCD simulations.

provide the former in Fig. A.1 and the latter in Fig. A.2. The continuum limits, and the linear coefficient in the fit for the case of $\frac{\mathrm{Tr}\,\Phi^2_{\mathrm{symm}}}{g^2_{3\mathrm{d}}}$, are provided in Table A.3.

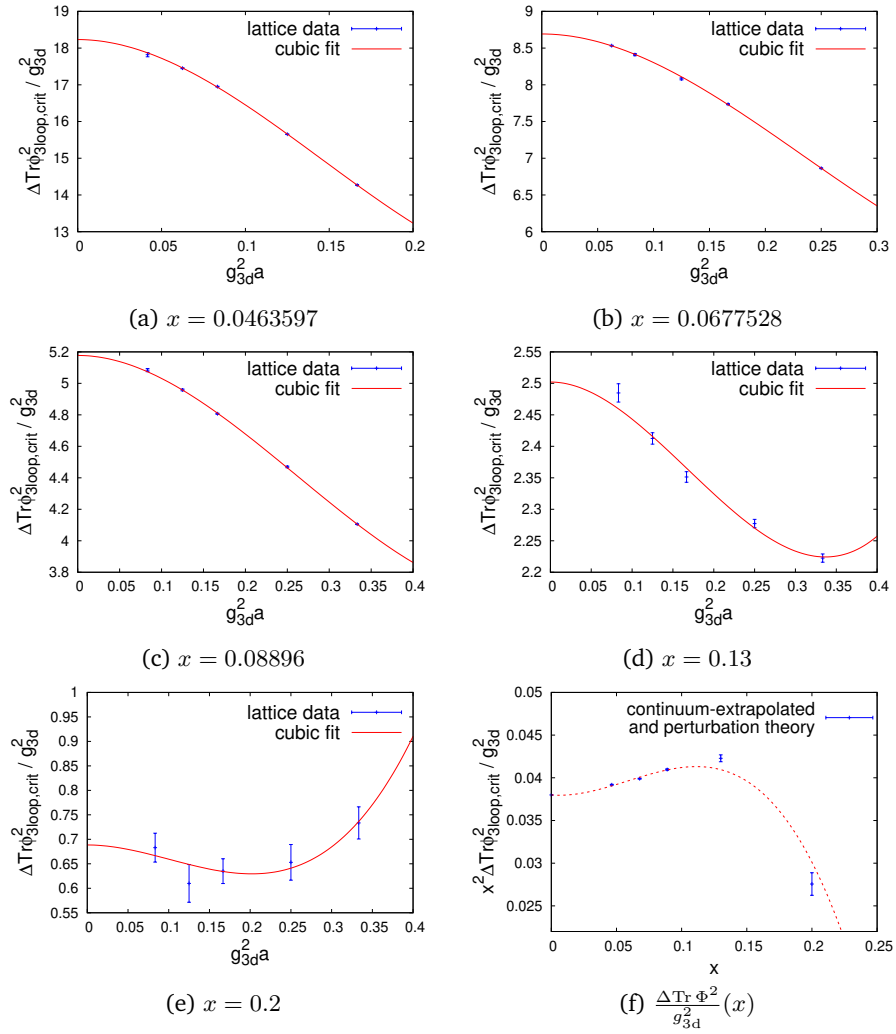

(a) $x = 0.0463597$ (b) $x = 0.0677528$

(c) $x = 0.08896$ (d) $x = 0.13$

(e) $x = 0.2$ (f) $\frac{\Delta \mathrm{Tr}\,\Phi^2}{g^2_{3\mathrm{d}}}(x)$

Figure A.1.: Continuum extrapolation of $\frac{\Delta \mathrm{Tr}\,\Phi^2}{g^2_{3\mathrm{d}}}$, the difference of the broken and symmetric phase value of $\frac{\mathrm{Tr}\,\Phi^2}{g^2_{3\mathrm{d}}}$, at different x. The intercept in (f) was determined analytically in [120] and was incorporated into that plot.

The limiting values of the fits provide us with two interesting pieces of information about

x	$\mathrm{Tr}\,\Phi^2_{\mathrm{symm,cont}}/g^2_{\mathrm{3d}}$	$\delta\mathrm{Tr}\,\Phi^2_{\mathrm{3loop}}/g^4_{\mathrm{3d}}a$	$\Delta\mathrm{Tr}\,\Phi^2_{\mathrm{cont}}/g^2_{\mathrm{3d}}$
0.0463597	$-0.2350(24)$	$-0.081(44)$	$18.232(27)$
0.0677528	$-0.1231(22)$	$-0.019(30)$	$8.692(13)$
0.08896	$-0.0272(27)$	$-0.072(25)$	$5.177(11)$
0.13	$0.151(11)$	$-0.256(70)$	$2.502(24)$
0.2	$0.763(76)$	$-0.66(85)$	$0.689(33)$

Table A.3.: Continuum-extrapolated $\frac{\mathrm{Tr}\,\Phi^2}{g^2_{\mathrm{3d}}}$ in the symmetric phase at criticality, $\mathcal{O}(a)$ operator improvement of $\frac{\mathrm{Tr}\,\Phi^2}{g^2_{\mathrm{3d}}}$ and continuum- extrapolated difference of $\frac{\mathrm{Tr}\,\Phi^2}{g^2_{\mathrm{3d}}}$ in the two phases at criticality.

the phase transition in this theory. The most interesting is $\frac{\Delta\mathrm{Tr}\,\Phi^2}{g^2_{\mathrm{3d}}}$, which measures the strength of the phase transition. For small x we can predict this strength perturbatively; the limiting behavior is [120] $\frac{\Delta\mathrm{Tr}\,\Phi^2}{g^2_{\mathrm{3d}}} = 3/(8\pi^2x^2)$, which we also include in the last frame of Fig. A.1. We have provided a cubic fit to guide the eye, but it should not be taken seriously; the strength of the phase transition is a nonperturbative quantity and there is no reason to expect it to take such a simple form. In fact, we know that $\frac{\Delta\mathrm{Tr}\,\Phi^2}{g^2_{\mathrm{3d}}} \to 0$ as $x \to x_{\mathrm{triple}}$, with a nontrivial critical exponent. Note that in the fit for the a dependence of $\frac{\Delta\mathrm{Tr}\,\Phi^2}{g^2_{\mathrm{3d}}}$, we have fitted to a polynomial without a linear term; this is because the known $\mathcal{O}(a)$ corrections are sufficient to eliminate such a linear correction in the *difference* between phases of $\frac{\mathrm{Tr}\,\Phi^2}{g^2_{\mathrm{3d}}}$.

A.2.3. Additive operator improvement

On the other hand, the value of either $\frac{\mathrm{Tr}\,\Phi^2_{\mathrm{symm}}}{g^2_{\mathrm{3d}}}$ or $\frac{\mathrm{Tr}\,\Phi^2_{\mathrm{brok}}}{g^2_{\mathrm{3d}}}$, by themselves, still contain $\mathcal{O}(a)$ errors, since there is an unknown additive renormalization to the operator $\mathrm{Tr}\,\Phi^2$ which arises at 3 loops. Since the correction is additive and both phases were explored at the same y value, these effects cancel in the difference. We took advantage of this cancellation in the last subsection. But now our goal is to use this linear behavior to extract the unknown $\mathcal{O}(a)$ additive corrections to the Φ^2 operator. These arise at 3 loops in a perturbative lattice-continuum matching calculation, which is prohibitive; so we will again try to extract them from the data.

Because we are working to 3 loops, we must specify quite carefully how 1-loop multiplicative effects will be implemented, since they can multiply one and two loop additive effects to give 3-loop level contributions, which then differ depending on our exact procedure.

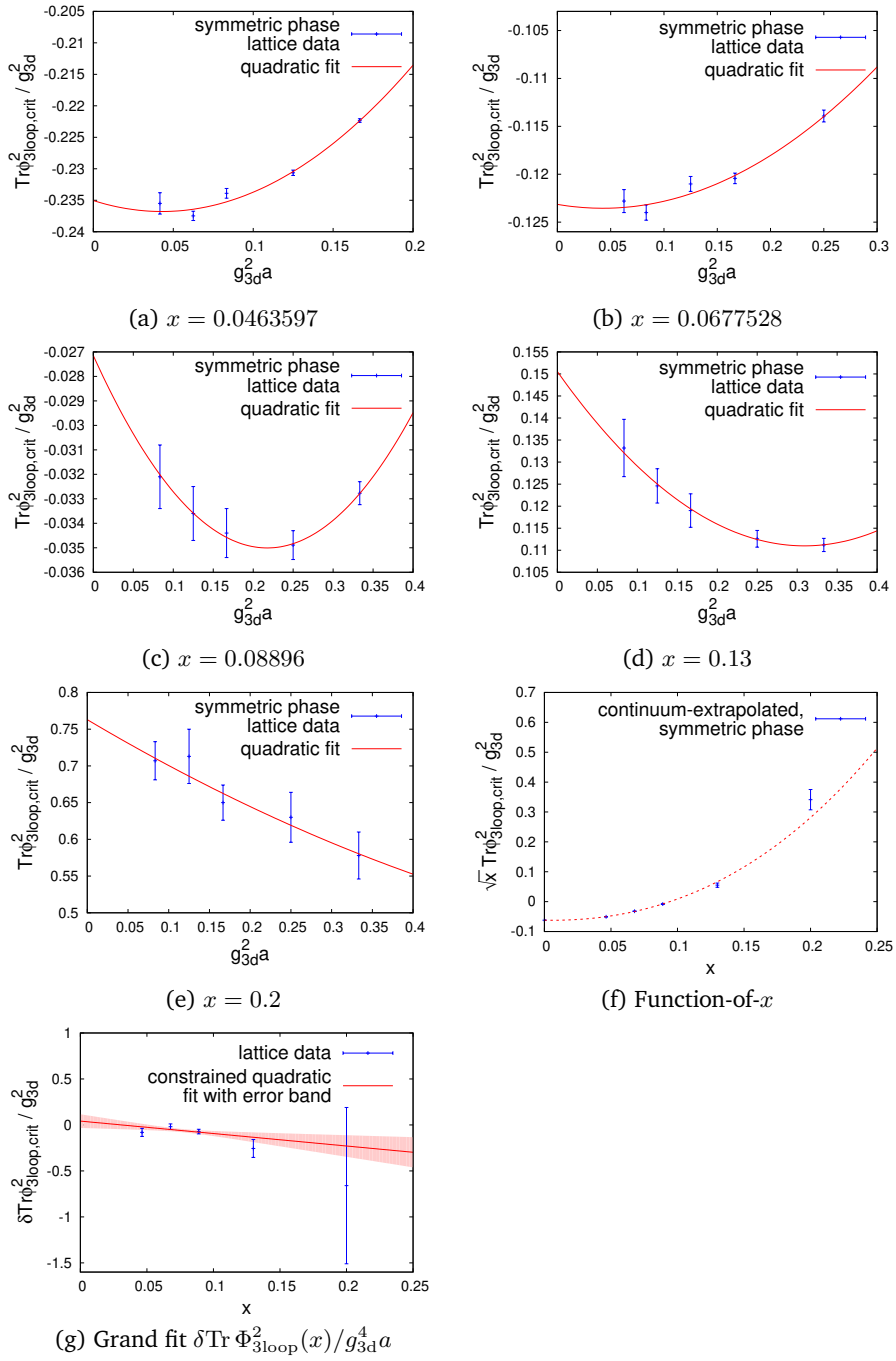

(a) $x = 0.0463597$

(b) $x = 0.0677528$

(c) $x = 0.08896$

(d) $x = 0.13$

(e) $x = 0.2$

(f) Function-of-x

(g) Grand fit $\delta\mathrm{Tr}\,\Phi^2_{3\mathrm{loop}}(x)/g^4_{3\mathrm{d}}a$

Figure A.2.: Fits of $\frac{\mathrm{Tr}\,\Phi^2}{g^2_{3\mathrm{d}}}(g^2_{3\mathrm{d}}a)$ at different x and grand fit.

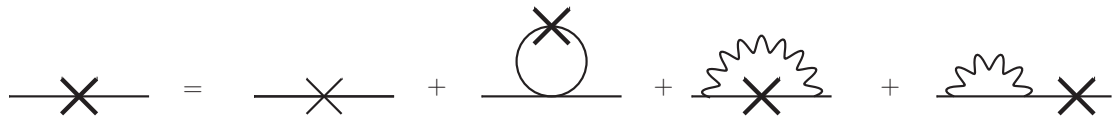

Figure A.3.: Diagrams generating Z_m the multiplicative $\mathrm{Tr}\,\Phi^2$ operator renormalization. Heavy crosses are the renormalized operator (with Z_m factor), while light crosses are the bare operator.

Here we will depart slightly from the procedure of Refs [111, 114, 137]. We write the continuum expectation value as

$$\frac{\mathrm{Tr}\,\Phi^2_{\mathrm{cont}}}{g^2_{3\mathrm{d}}} = Z_m \left(Z_\Phi \mathrm{Tr}\,\Phi^2_{\mathrm{L}} - \frac{\delta\Phi^2}{g^2_{3\mathrm{d}}} \right) , \tag{A.2}$$

where Z_m is the 1-loop multiplicative renormalization factor of the $\mathrm{Tr}\,\Phi^2$ operator, and Z_Φ accounts for our choice of scalar field normalization on the lattice (see Eq. (4.1)). Examining the 3-loop diagrams, we find that certain 3-loop effects are absorbed if we define Z_m, *resumming* the Dyson series. That is, in Figure A.3, we take the operator inserted on the 1-loop diagrams to be the resummed, rather than the bare, operator, which will sum the Dyson series, leading to an expression for Z_m^{-1}. Slightly rearranging Eq.(32,33) of Ref. [114], we find

$$Z_m^{-1} = 1 + \frac{g^2_{3\mathrm{d}} a}{4\pi} \left(3N\xi + \frac{N\Sigma}{6} - (N^2+1)\xi x \right) . \tag{A.3}$$

Here $\xi = 0.152859324966$ and $\Sigma = 3.17591153562522$ are standard integrals encountered in the 1-loop lattice-continuum matching. We are also writing the number of colors $N = 3$ explicitly, to show the detailed dependence on the number of colors. With this definition, the two-loop and partially 3-loop result for $\delta\Phi^2$ is

$$\begin{aligned} \frac{\delta\Phi^2}{g^2_{3\mathrm{d}}} \;=\; & \frac{N^2-1}{2g^2_{3\mathrm{d}}a} \left[\frac{\Sigma}{4\pi} - \frac{\xi y g^4_{3\mathrm{d}} a^2}{4\pi} + \frac{N g^2_{3\mathrm{d}} a}{(4\pi)^2} Z_m^{-1} \left(2\ln\frac{6}{g^2_{3\mathrm{d}}a} + 2\zeta - 2\delta + \frac{\Sigma^2}{2} \right) \right. \\ & \left. + \frac{g^4_{3\mathrm{d}} a^2}{(4\pi)^3} \Big(2\xi(N^2+1)(x^2-Nx)\ln(g^2_{3\mathrm{d}}a) + C_{\Phi a} + C_{\Phi b}x + C_{\Phi c}x^2 \Big) \right] \end{aligned} \tag{A.4}$$

The unknown coefficients $C_{\Phi a}$, $C_{\Phi b}$ and $C_{\Phi c}$ capture the remaining $\mathcal{O}(a)$ corrections from 3-loop diagrams which are not iterations of simpler 1 and 2 loop diagrams. Note that Eq. (A.4) contains several terms proportional to $\ln(g^2_{3\mathrm{d}}a)$. These arise from logarithmic divergences in the continuum theory, regulated at our choice of renormalization point $\mu = g^2_{3\mathrm{d}}$ but then cut off on the lattice at the scale $1/a$. The term next to $\zeta - \delta$ is the

explicit μ^2 dependence of $\Phi^2/g_{3\mathrm{d}}^2$ and is therefore expected; the coefficient Z_m^{-1} ensures that it enters Eq. (A.2) with precisely the right continuum normalization. The log terms proportional to ξ in the last line cancel the μ dependence of the mass squared (y) in the mass-dependent $\mathcal{O}(a)$ shift in the first line.

It remains to determine the three coefficients in the last line. In fact, we only need to fit two of these coefficients; one of them, $C_{\Phi c}$, represents pure-scalar corrections, which can be extracted from Ref. [137]. The reference performs the calculation for an improved hopping term, but repeating the calculation for the nearest-neighbor hopping term we use here[2], we find that

$$C_{\Phi c} = 2(N^2+1)C_4\,, \qquad C_4 = 0.5630(4)\,, \tag{A.5}$$

which differs from the result in the reference, $C_{4,\mathrm{Ref}} = 0.2817$, because of the different scalar dispersion between the nearest-neighbor hopping term used here and the improved hopping term used there.[3]

After performing these subtractions, we can fit the residual linear a-dependence of $\mathrm{Tr}\,\Phi_{\mathrm{L}}^2$ for each x value we consider, and extract the coefficients $C_{\Phi a}, C_{\Phi b}$ from a grand fit in complete analogy with the m^2 effects we consider in the main text. We find

$$C_{\Phi a} = (-21 \pm 37) \tag{A.6}$$

$$C_{\Phi b} = (6.7 \pm 4.7) \times 10^2\,, \tag{A.7}$$

again by constrained curve fitting. The grand fit is displayed in the seventh frame of Fig. A.2. Unfortunately, it appears that our results fail to constrain these coefficients very much. The full covariance matrix can be found in Tab. A.4. From the covariance matrix, we can also see that the error of $C_{\Phi c}$ is by far the smallest, so value and error of $C_{\Phi c}$ were not changed by the constrained fit.

[2] The rest of the $\mathcal{O}(a)$ corrections are not known for improved actions, which is why we do not attempt to use an improved action here. Using improved actions only really helps if one can complete the 2-loop $\mathcal{O}(a^2)$ matching calculation; this is feasible in a scalar theory, but does not appear practical in a gauge theory as we consider here.

[3] Specifically, in passing from the improved to the unimproved hopping term, Ref. [137] (B38) has $0.30837 \to 0.2268854$; (B40) has $.00031757 \to .000490546$, the value of ξ changes from $\xi = -.08365 \to +.1528593$, and (B41) changes from $.0985(6) \to .1063(4)$.

$\mathrm{cov}(C_i, C_j)$	$C_{\Phi a}$	$C_{\Phi b}$	$C_{\Phi c}$
$C_{\Phi a}$	21694	-267617	$5.3859 \cdot 10^{-6}$
$C_{\Phi b}$	-267617	$3.4914 \cdot 10^{6}$	$-1.432 \cdot 10^{-4}$
$C_{\Phi c}$	$5.3859 \cdot 10^{-6}$	$-1.432 \cdot 10^{-4}$	$9.0 \cdot 10^{-4}$

Table A.4.: Covariance matrix of the grand fit of the missing 3 loop $\frac{\delta\Phi^2}{g_{3\mathrm{d}}^2}$-contribution.

A.3. Simulation parameters and correlation matrices

For completeness, we provide a "data dump" of the details of our simulated boxes, statistics, and correlation matrices. Because the correlation matrices are symmetric and nearly band-diagonal, we will only list the entries 1 to 3 places to the right of the diagonal.

We also explain what at first sight is an odd choice of lattice volumes. The volume should be chosen such that $N_{x/y/z} \geq \beta$ in order to avoid finite volume effects [125]. Furthermore, it has to fulfill $N_{x/y} > 2\boldsymbol{b}_\perp{}^{\max}$ and $N_z > 2L^{\max}$ to suppress an (unphysical) correlation over the boundaries of the simulated box. Since not all $g_{3\mathrm{d}}^2 a$ lattices produce sensible information at all $g_{3\mathrm{d}}^2 b_\perp$ and only 3 lattices are required for a continuum limit, the choice of volumes seems a little odd at first sight.

$g_{3d}^2 a$	x_{cont}	y_{cont}	$N_x N_y N_z$	$b_\perp/a$	L/a	statistics
1/4	0.08896	0.452423	$52^2 \times 64$	4, 6, 8, 10, 12, 16, 20, 24	4, 8, 12, 16, 20, 24, 28	7840
1/6	0.08896	0.452423	$76^2 \times 96$	6, 9, 12, 15, 18, 24, 30, 36	6, 12, 18, 24, 30, 36, 42	5900
1/8	0.08896	0.452423	$100^2 \times 128$	4, 6, 8, 12, 16, 20, 24, 32, 40, 48	8, 16, 24, 32, 40, 48, 56	4760
1/12	0.08896	0.452423	$72^2 \times 192$	6, 9, 12, 18, 24, 30	12, 24, 36, 48, 60, 72, 84	4000
1/16	0.08896	0.452423	$96^2 \times 256$	4, 8, 12, 16, 24	16, 32, 48, 64, 80, 96, 112	5480
1/24	0.08896	0.452423	$144^2 \times 384$	6, 12	24, 48, 72, 96, 120, 144, 168	240
1/32	0.08896	0.452423	$192^2 \times 512$	4, 8, 16	32, 64, 96, 128, 160, 192, 224	60
1/4	0.0677528	0.586204	$52^2 \times 64$	4, 6, 8, 10, 12, 16, 20, 24	4, 8, 12, 16, 20, 24, 28	8740
1/6	0.0677528	0.586204	$76^2 \times 96$	6, 9, 12, 15, 18, 24, 30, 36	6, 12, 18, 24, 30, 36, 42	5700
1/8	0.0677528	0.586204	$100^2 \times 128$	4, 6, 8, 12, 16, 20, 24, 32, 40, 48	8, 16, 24, 32, 40, 48, 56	2800
1/12	0.0677528	0.586204	$72^2 \times 192$	6, 9, 12, 18, 24, 30	12, 24, 36, 48, 60, 72, 84	4560
1/16	0.0677528	0.586204	$96^2 \times 256$	4, 8, 12, 16, 24	16, 32, 48, 64, 80, 96, 112	5540
1/4	0.0463597	0.823449	$52^2 \times 64$	4, 6, 8, 10, 12, 16, 20, 24	4, 8, 12, 16, 20, 24, 28	8600
1/6	0.0463597	0.823449	$76^2 \times 96$	6, 9, 12, 15, 18, 24, 30, 36	6, 12, 18, 24, 30, 36, 42	4660
1/8	0.0463597	0.823449	$100^2 \times 128$	4, 6, 8, 12, 16, 20, 24, 32, 40, 48	8, 16, 24, 32, 40, 48, 56	3790
1/12	0.0463597	0.823449	$72^2 \times 192$	6, 9, 12, 18, 24, 30	12, 24, 36, 48, 60, 72, 84	4600
1/16	0.0463597	0.823449	$96^2 \times 256$	4, 8, 12, 16, 24	16, 32, 48, 64, 80, 96, 112	5820
1/4	0.0178626	1.64668	$52^2 \times 64$	4, 6, 8, 10, 12, 16, 20, 24	4, 8, 12, 16, 20, 24, 28	7760
1/6	0.0178626	1.64668	$76^2 \times 96$	6, 9, 12, 15, 18, 24, 30, 36	6, 12, 18, 24, 30, 36, 42	6500
1/8	0.0178626	1.64668	$100^2 \times 128$	4, 6, 8, 12, 16, 20, 24, 32, 40, 48	8, 16, 24, 32, 40, 48, 56	4780
1/12	0.0178626	1.64668	$72^2 \times 192$	6, 9, 12, 18, 24, 30	12, 24, 36, 48, 60, 72, 84	2920
1/16	0.0178626	1.64668	$96^2 \times 256$	4, 8, 12, 16, 24	16, 32, 48, 64, 80, 96, 112	4080
1/24	0.0178626	1.64668	$144^2 \times 384$	6, 12	24, 48, 72, 96, 120, 144, 168	240
1/32	0.0178626	1.64668	$192^2 \times 512$	4, 8, 16	32, 64, 96, 128, 160, 192, 224	60

Table A.5.: Parameters for all EQCD multi-level simulations.

$g_{3d}^2 b_\perp$	nearest neighbor	next	next
0.25	0.29	0.012	0.0033
0.5	0.0095	0.016	0.0036
0.75	0.73	0.17	0.19
1.0	0.32	0.31	0.22
1.5	0.24	0.47	0.63
2.0	0.47	0.13	0.014
2.5	0.094	0.060	0.048
3.0	0.48	0.28	−0.18
4.0	0.38	−0.049	-
5.0	−0.13	-	-

Table A.6.: Correlation matrix for $x = 0.08896$ case.

$g_{3d}^2 b_\perp$	nearest neighbor	next	next
0.5	0.60	0.65	0.58
0.75	0.72	0.91	0.36
1.0	0.47	0.46	0.46
1.5	0.27	0.37	0.12
2.0	0.31	0.13	0.24
2.5	0.30	0.03	0.036
3.0	0.036	0.09	0.088
4.0	−0.029	−0.011	-
5.0	−0.0041	-	-

Table A.7.: Correlation matrix for $x = 0.0677528$ case.

$g_{3d}^2 b_\perp$	nearest neighbor	next	next
0.5	043	0.66	0.26
0.75	0.64	0.53	0.55
1.0	0.32	0.15	0.26
1.5	0.61	0.46	0.13
2.0	0.54	0.13	0.0082
2.5	0.13	−0.066	0.039
3.0	0.03	0.094	−0.21
4.0	0.17	−0.035	-
5.0	−0.071	-	-

Table A.8.: Correlation matrix for $x = 0.0463597$ case.

$g_{3d}^2 b_\perp$	nearest neighbor	next	next
0.25	0.17	−0.26	−0.53
0.5	0.027	0.032	0.023
0.75	0.82	0.34	0.65
1.0	0.39	0.20	0.015
1.5	0.66	0.037	0.04
2.0	0.13	−0.0037	0.096
2.5	−0.0017	0.02	0.0054
3.0	0.037	0.0066	0.0013
4.0	0.034	−0.18	-
5.0	0.032	-	-

Table A.9.: Correlation matrix for $x = 0.0178626$ case.

Bibliography

[1] J. Dalton. *A New System of Chemical Philosophy*. S. Russell, 1808.

[2] D. Bernoulli. *Hydrodynamica*. 1738.

[3] E. Rutherford. The scattering of alpha and beta particles by matter and the structure of the atom. *Phil. Mag. Ser. 6*, 21:669–688, 1911.

[4] N. Bohr. On the Constitution of Atoms and Molecules. *Phil. Mag. Ser. 6*, 26:1–24, 1913.

[5] S.L. Glashow. Partial Symmetries of Weak Interactions. *Nucl. Phys.*, 22:579–588, 1961.

[6] Steven Weinberg. A Model of Leptons. *Phys. Rev. Lett.*, 19:1264–1266, 1967.

[7] Abdus Salam. Gauge Unification of Fundamental Forces. *Rev. Mod. Phys.*, 52:525–538, 1980.

[8] K. Abe et al. Search for proton decay via $p \to e^+\pi^0$ and $p \to \mu^+\pi^0$ in 0.31 megaton·years exposure of the Super-Kamiokande water Cherenkov detector. *Phys. Rev.*, D95(1):012004, 2017.

[9] Kenneth G. Wilson. Renormalization group and critical phenomena. 1. Renormalization group and the Kadanoff scaling picture. *Phys. Rev. B*, 4:3174–3183, 1971.

[10] Brian C. Odom, D. Hanneke, B. D'Urso, and G. Gabrielse. New Measurement of the Electron Magnetic Moment Using a One-Electron Quantum Cyclotron. *Phys. Rev. Lett.*, 97:030801, 2006.

[11] T. Aoyama, M. Hayakawa, T. Kinoshita, and Makiko Nio. Automated calculation scheme for alpha**n contributions of QED to lepton g-2: New treatment of infrared divergence for diagrams without lepton loops. *Nucl. Phys. B*, 796:184–210, 2008.

[12] Serguei Chatrchyan et al. Observation of a New Boson at a Mass of 125 GeV with the CMS Experiment at the LHC. *Phys. Lett.*, B716:30–61, 2012.

[13] S. S. Adler et al. Elliptic flow of identified hadrons in Au+Au collisions at s(NN)**(1/2) = 200-GeV. *Phys. Rev. Lett.*, 91:182301, 2003.

[14] J. Adams et al. Azimuthal anisotropy in Au+Au collisions at s(NN)**(1/2) = 200-GeV. *Phys. Rev.*, C72:014904, 2005.

[15] A. Adare et al. Enhanced production of direct photons in Au+Au collisions at $\sqrt{s_{NN}} = 200$ GeV and implications for the initial temperature. *Phys. Rev. Lett.*, 104:132301, 2010.

[16] A. Adare et al. Detailed measurement of the e^+e^- pair continuum in $p+p$ and Au+Au collisions at $\sqrt{s_{NN}} = 200$ GeV and implications for direct photon production. *Phys. Rev. C*, 81:034911, 2010.

[17] A. Adare et al. J/ψ Production vs Centrality, Transverse Momentum, and Rapidity in Au+Au Collisions at $\sqrt{s_{NN}} = 200$ GeV. *Phys. Rev. Lett.*, 98:232301, 2007.

[18] K. Aamodt et al. Higher harmonic anisotropic flow measurements of charged particles in Pb-Pb collisions at $\sqrt{s_{NN}}$=2.76 TeV. *Phys. Rev. Lett.*, 107:032301, 2011.

[19] Serguei Chatrchyan et al. Multiplicity and Transverse Momentum Dependence of Two- and Four-Particle Correlations in pPb and PbPb Collisions. *Phys. Lett.*, B724:213–240, 2013.

[20] Georges Aad et al. Measurement of event-plane correlations in $\sqrt{s_{NN}} = 2.76$ TeV lead-lead collisions with the ATLAS detector. *Phys. Rev.*, C90(2):024905, 2014.

[21] Jaroslav Adam et al. Correlated event-by-event fluctuations of flow harmonics in Pb-Pb collisions at $\sqrt{s_{\rm NN}} = 2.76$ TeV. *Phys. Rev. Lett.*, 117:182301, 2016.

[22] J.D. Bjorken. Energy Loss of Energetic Partons in Quark - Gluon Plasma: Possible Extinction of High p(t) Jets in Hadron - Hadron Collisions. 8 1982.

[23] B. G. Zakharov. Fully quantum treatment of the Landau-Pomeranchuk-Migdal effect in QED and QCD. *JETP Lett.*, 63:952–957, 1996.

[24] B. G. Zakharov. Radiative energy loss of high-energy quarks in finite size nuclear matter and quark - gluon plasma. *JETP Lett.*, 65:615–620, 1997.

[25] B. G. Zakharov. Light cone path integral approach to the Landau-Pomeranchuk-Migdal effect. *Phys. Atom. Nucl.*, 61:838–854, 1998. [Yad. Fiz.61,924(1998)].

[26] P. Aurenche, F. Gelis, and H. Zaraket. A Simple sum rule for the thermal gluon spectral function and applications. *JHEP*, 05:043, 2002.

[27] Peter Brockway Arnold and Wei Xiao. High-energy jet quenching in weakly-coupled quark-gluon plasmas. *Phys. Rev.*, D78:125008, 2008.

[28] Jorge Casalderrey-Solana and Derek Teaney. Transverse Momentum Broadening of a Fast Quark in a N=4 Yang Mills Plasma. *JHEP*, 04:039, 2007.

[29] Simon Caron-Huot. O(g) plasma effects in jet quenching. *Phys. Rev.*, D79:065039, 2009.

[30] Marco Panero, Kari Rummukainen, and Andreas Schäfer. Lattice Study of the Jet Quenching Parameter. *Phys. Rev. Lett.*, 112(16):162001, 2014.

[31] Morad Aaboud et al. Dijet azimuthal correlations and conditional yields in pp and p+Pb collisions at sNN=5.02TeV with the ATLAS detector. *Phys. Rev. C*, 100(3):034903, 2019.

[32] Jacopo Ghiglieri, Guy D. Moore, and Derek Teaney. QCD Shear Viscosity at (almost) NLO. *JHEP*, 03:179, 2018.

[33] Jacopo Ghiglieri, Juhee Hong, Aleksi Kurkela, Egang Lu, Guy D. Moore, and Derek Teaney. Next-to-leading order thermal photon production in a weakly coupled quark-gluon plasma. *JHEP*, 05:010, 2013.

[34] C. P. Burgess and G. D. Moore. *The standard model: A primer*. Cambridge University Press, 2006.

[35] W. Greiner, S. Schramm, and E. Stein. *Quantum chromodynamics*. 2002.

[36] Murray Gell-Mann. The Eightfold Way: A Theory of strong interaction symmetry. 1961.

[37] G. Zweig. An SU(3) model for strong interaction symmetry and its breaking. Version 2. In D.B. Lichtenberg and Simon Peter Rosen, editors, *Developments in the Quark Theory of Hadrons*, pages 22–101. 1964.

[38] `https://de.wikipedia.org/wiki/Eightfold_Way`.

[39] Elliott D. Bloom et al. High-Energy Inelastic e p Scattering at 6-Degrees and 10-Degrees. *Phys. Rev. Lett.*, 23:930–934, 1969.

[40] Martin Breidenbach, Jerome I. Friedman, Henry W. Kendall, Elliott D. Bloom, D. H. Coward, H. C. DeStaebler, J. Drees, Luke W. Mo, and Richard E. Taylor. Observed Behavior of Highly Inelastic electron-Proton Scattering. *Phys. Rev. Lett.*, 23:935–939, 1969.

[41] J. D. Bjorken. Asymptotic Sum Rules at Infinite Momentum. *Phys. Rev.*, 179:1547–1553, 1969.

[42] H. Fritzsch, Murray Gell-Mann, and H. Leutwyler. Advantages of the Color Octet Gluon Picture. *Phys. Lett.*, 47B:365–368, 1973.

[43] Chen-Ning Yang and R. L. Mills. Isotopic spin conservation and a generalized gauge invariance. *Phys. Rev.*, 96:191, 1954.

[44] R. Brandelik et al. Evidence for Planar Events in e+ e- Annihilation at High-Energies. *Phys. Lett.*, 86B:243–249, 1979.

[45] R. Brandelik et al. Evidence for a Spin One Gluon in Three Jet Events. *Phys. Lett.*, 97B:453–458, 1980.

[46] J. Fuchs and C. Schweigert. *Symmetries, Lie algebras and representations: A graduate course for physicists*. Cambridge University Press, 2003.

[47] P. Pascual and R. Tarrach. QCD: Renormalization for the Practitioner. *Lect. Notes Phys.*, 194:1–277, 1984.

[48] Christof Gattringer and Christian B. Lang. Quantum chromodynamics on the lattice. *Lect. Notes Phys.*, 788:1–343, 2010.

[49] D. Binosi, J. Collins, C. Kaufhold, and L. Theussl. JaxoDraw: A Graphical user interface for drawing Feynman diagrams. Version 2.0 release notes. *Comput. Phys. Commun.*, 180:1709–1715, 2009.

[50] Kenneth G. Wilson. Confinement of quarks. *Phys. Rev. D*, 10:2445–2459, Oct 1974.

[51] Marco Guagnelli, Rainer Sommer, and Hartmut Wittig. Precision computation of a low-energy reference scale in quenched lattice QCD. *Nucl. Phys.*, B535:389–402, 1998.

[52] David J. Gross and Frank Wilczek. Ultraviolet behavior of non-abelian gauge theories. *Phys. Rev. Lett.*, 30:1343–1346, Jun 1973.

[53] H. David Politzer. Reliable perturbative results for strong interactions? *Phys. Rev. Lett.*, 30:1346–1349, Jun 1973.

[54] Mattia Bruno, Mattia Dalla Brida, Patrick Fritzsch, Tomasz Korzec, Alberto Ramos, Stefan Schaefer, Hubert Simma, Stefan Sint, and Rainer Sommer. QCD Coupling from a Nonperturbative Determination of the Three-Flavor Λ Parameter. *Phys. Rev. Lett.*, 119(10):102001, 2017.

[55] Gert Aarts. Introductory lectures on lattice QCD at nonzero baryon number. *J. Phys. Conf. Ser.*, 706(2):022004, 2016.

[56] J. C. Collins and M. J. Perry. Superdense matter: Neutrons or asymptotically free quarks? *Phys. Rev. Lett.*, 34:1353–1356, May 1975.

[57] Edward V. Shuryak. Theory of Hadronic Plasma. *Sov. Phys. JETP*, 47:212–219, 1978. [Zh. Eksp. Teor. Fiz.74,408(1978)].

[58] I. Arsene et al. Quark gluon plasma and color glass condensate at RHIC? The Perspective from the BRAHMS experiment. *Nucl. Phys.*, A757:1–27, 2005.

[59] B. B. Back et al. The PHOBOS perspective on discoveries at RHIC. *Nucl. Phys.*, A757:28–101, 2005.

[60] John Adams et al. Experimental and theoretical challenges in the search for the quark gluon plasma: The STAR Collaboration's critical assessment of the evidence from RHIC collisions. *Nucl. Phys.*, A757:102–183, 2005.

[61] K. Adcox et al. Formation of dense partonic matter in relativistic nucleus-nucleus collisions at RHIC: Experimental evaluation by the PHENIX collaboration. *Nucl. Phys.*, A757:184–283, 2005.

[62] P. Hasenfratz and F. Karsch. Chemical Potential on the Lattice. *Phys. Lett.*, 125B:308–310, 1983.

[63] H. J. Rothe. Lattice gauge theories: An Introduction. *World Sci. Lect. Notes Phys.*, 43:1–381, 1992. [World Sci. Lect. Notes Phys.82,1(2012)].

[64] F. J. Wegner. Duality in Generalized Ising Models and Phase Transitions Without Local Order Parameters. *J. Math. Phys.*, 12:2259–2272, 1971.

[65] N. Metropolis, A. W. Rosenbluth, M. N. Rosenbluth, A. H. Teller, and E. Teller. Equation of state calculations by fast computing machines. *J. Chem. Phys.*, 21:1087–1092, 1953.

[66] M. Creutz. Monte Carlo Study of Quantized SU(2) Gauge Theory. *Phys. Rev.*, D21:2308–2315, 1980.

[67] Stephen L. Adler. An Overrelaxation Method for the Monte Carlo Evaluation of the Partition Function for Multiquadratic Actions. *Phys. Rev.*, D23:2901, 1981. [,664(1981)].

[68] N. Cabibbo and E. Marinari. A New Method for Updating SU(N) Matrices in Computer Simulations of Gauge Theories. *Phys. Lett.*, 119B:387–390, 1982.

[69] Ulli Wolff. Monte Carlo errors with less errors. *Comput. Phys. Commun.*, 156:143–153, 2004. [Erratum: Comput. Phys. Commun.176,383(2007)].

[70] S. R. Beane, W. Detmold, K. Orginos, and M. J. Savage. Nuclear Physics from Lattice QCD. *Prog. Part. Nucl. Phys.*, 66:1–40, 2011.

[71] Thomas Appelquist and Robert D. Pisarski. High-Temperature Yang-Mills Theories and Three-Dimensional Quantum Chromodynamics. *Phys. Rev.*, D23:2305, 1981.

[72] Sudhir Nadkarni. Dimensional Reduction in Hot QCD. *Phys. Rev.*, D27:917, 1983.

[73] Eric Braaten and Agustin Nieto. Effective field theory approach to high temperature thermodynamics. *Phys. Rev.*, D51:6990–7006, 1995.

[74] Mikko Laine and Aleksi Vuorinen. Basics of Thermal Field Theory. *Lect. Notes Phys.*, 925:pp.1–281, 2016.

[75] Andrei D. Linde. Infrared Problem in Thermodynamics of the Yang-Mills Gas. *Phys. Lett.*, 96B:289–292, 1980.

[76] K. Kajantie, M. Laine, K. Rummukainen, and Mikhail E. Shaposhnikov. 3-D SU(N) + adjoint Higgs theory and finite temperature QCD. *Nucl. Phys.*, B503:357–384, 1997.

[77] M. Laine and Y. Schroder. Two-loop QCD gauge coupling at high temperatures. *JHEP*, 03:067, 2005.

[78] Murray Gell-Mann and M Levy. The axial vector current in beta decay. *Nuovo Cim.*, 16:705, 1960.

[79] K. Kajantie, M. Laine, K. Rummukainen, and Y. Schroder. The Pressure of hot QCD up to g6 ln(1/g). *Phys. Rev.*, D67:105008, 2003.

[80] M. Laine. What is the simplest effective approach to hot QCD thermodynamics? In *Proceedings, 5th Internationa Conference on Strong and Electroweak Matter (SEWM 2002): Heidelberg, Germany, October 2-5, 2002*, pages 137–146, 2003.

[81] Szabolcs Borsanyi, Zoltan Fodor, Jana N. Guenther, Ruben Kara, Sandor D. Katz, Paolo Parotto, Attila Pasztor, Claudia Ratti, and Kalman K. Szabo. The QCD crossover at finite chemical potential from lattice simulations. 2020.

[82] Ari Hietanen and Kari Rummukainen. The Diagonal and off-diagonal quark number susceptibility of high temperature and finite density QCD. *JHEP*, 04:078, 2008.

[83] A. Bazavov et al. Equation of state in (2+1)-flavor QCD. *Phys. Rev.*, D90:094503, 2014.

[84] Szabocls Borsanyi, Zoltan Fodor, Christian Hoelbling, Sandor D. Katz, Stefan Krieg, and Kalman K. Szabo. Full result for the QCD equation of state with 2+1 flavors. *Phys. Lett.*, B730:99–104, 2014.

[85] Hans-Thomas Elze and Ulrich W. Heinz. Quark - Gluon Transport Theory. *Phys. Rept.*, 183:81–135, 1989. [,117(1989)].

[86] Charles Gale, Sangyong Jeon, and Bjoern Schenke. Hydrodynamic Modeling of Heavy-Ion Collisions. *Int. J. Mod. Phys.*, A28:1340011, 2013.

[87] Harvey B. Meyer. Energy-momentum tensor correlators and spectral functions. *JHEP*, 08:031, 2008.

[88] Harvey B. Meyer. A Calculation of the shear viscosity in SU(3) gluodynamics. *Phys. Rev.*, D76:101701, 2007.

[89] Harvey B. Meyer. A Calculation of the bulk viscosity in SU(3) gluodynamics. *Phys. Rev. Lett.*, 100:162001, 2008.

[90] Marco Cè, Tim Harris, Harvey B. Meyer, Aman Steinberg, and Arianna Toniato. The rate of photon production in the quark-gluon plasma from lattice QCD. 2020.

[91] Peter Petreczky and Derek Teaney. Heavy quark diffusion from the lattice. *Phys. Rev.*, D73:014508, 2006.

[92] Harvey B. Meyer. The errant life of a heavy quark in the quark-gluon plasma. *New J. Phys.*, 13:035008, 2011.

[93] Gert Aarts, Chris Allton, Alessandro Amato, Pietro Giudice, Simon Hands, and Jon-Ivar Skullerud. Electrical conductivity and charge diffusion in thermal QCD from the lattice. *JHEP*, 02:186, 2015.

[94] Jorge Casalderrey-Solana and Carlos A. Salgado. Introductory lectures on jet quenching in heavy ion collisions. *Acta Phys. Polon.*, B38:3731–3794, 2007.

[95] Rolf Baier and Yacine Mehtar-Tani. Jet quenching and broadening: The Transport coefficient q-hat in an anisotropic plasma. *Phys. Rev.*, C78:064906, 2008.

[96] Jurgen Berges. Nonequilibrium Quantum Fields: From Cold Atoms to Cosmology. 2015.

[97] Jacopo Ghiglieri, Guy D. Moore, and Derek Teaney. Jet-Medium Interactions at NLO in a Weakly-Coupled Quark-Gluon Plasma. *JHEP*, 03:095, 2016.

[98] Zhe Xu and Carsten Greiner. Thermalization of gluons in ultrarelativistic heavy ion collisions by including three-body interactions in a parton cascade. *Phys. Rev.*, C71:064901, 2005.

[99] J. Weil et al. Particle production and equilibrium properties within a new hadron transport approach for heavy-ion collisions. *Phys. Rev.*, C94(5):054905, 2016.

[100] Peter Brockway Arnold, Guy D. Moore, and Laurence G. Yaffe. Transport coefficients in high temperature gauge theories. 1. Leading log results. *JHEP*, 11:001, 2000.

[101] Peter Brockway Arnold, Guy D. Moore, and Laurence G. Yaffe. Photon emission from ultrarelativistic plasmas. *JHEP*, 11:057, 2001.

[102] Peter Brockway Arnold, Guy D. Moore, and Laurence G. Yaffe. Photon emission from quark gluon plasma: Complete leading order results. *JHEP*, 12:009, 2001.

[103] Peter Brockway Arnold, Guy D. Moore, and Laurence G. Yaffe. Photon and gluon emission in relativistic plasmas. *JHEP*, 06:030, 2002.

[104] Peter Brockway Arnold, Guy D. Moore, and Laurence G. Yaffe. Effective kinetic theory for high temperature gauge theories. *JHEP*, 01:030, 2003.

[105] Peter Brockway Arnold, Guy D Moore, and Laurence G. Yaffe. Transport coefficients in high temperature gauge theories. 2. Beyond leading log. *JHEP*, 05:051, 2003.

[106] Bjoern Schenke, Charles Gale, and Sangyong Jeon. MARTINI: Monte Carlo simulation of jet evolution. *Acta Phys. Polon. Supp.*, 3:765–770, 2010.

[107] Simon Caron-Huot and Charles Gale. Finite-size effects on the radiative energy loss of a fast parton in hot and dense strongly interacting matter. *Phys. Rev.*, C82:064902, 2010.

[108] Yacine Mehtar-Tani and Konrad Tywoniuk. Improved opacity expansion for medium-induced parton splitting. 2019.

[109] Carlota Andres, Liliana Apolinário, and Fabio Dominguez. Medium-induced gluon radiation with full resummation of multiple scatterings for realistic parton-medium interactions. 2020.

[110] P. Aurenche, F. Gelis, G. D. Moore, and H. Zaraket. Landau-Pomeranchuk-Migdal resummation for dilepton production. *JHEP*, 12:006, 2002.

[111] Michela D'Onofrio, Aleksi Kurkela, and Guy D. Moore. Renormalization of Null Wilson Lines in EQCD. *JHEP*, 03:125, 2014.

[112] Martin Luscher and Peter Weisz. Locality and exponential error reduction in numerical lattice gauge theory. *JHEP*, 09:010, 2001.

[113] Harvey B. Meyer. Locality and statistical error reduction on correlation functions. *JHEP*, 01:048, 2003.

[114] Guy D. Moore. O(a) errors in 3-D SU(N) Higgs theories. *Nucl. Phys.*, B523:569–593, 1998.

[115] M. Laine. Exact relation of lattice and continuum parameters in three-dimensional SU(2) + Higgs theories. *Nucl. Phys.*, B451:484–504, 1995.

[116] Guy D. Moore and Niels Schlusser. Full O(a) improvement in electrostatic QCD. *Phys. Rev.*, D100(3):034510, 2019.

[117] A. Vuorinen and Laurence G. Yaffe. Z(3)-symmetric effective theory for SU(3) Yang-Mills theory at high temperature. *Phys. Rev.*, D74:025011, 2006.

[118] K. Kajantie, M. Laine, K. Rummukainen, and Mikhail E. Shaposhnikov. The Electroweak phase transition: A Nonperturbative analysis. *Nucl. Phys.*, B466:189–258, 1996.

[119] `http://luscher.web.cern.ch/luscher/openQCD/index.html`.

[120] K. Kajantie, M. Laine, A. Rajantie, K. Rummukainen, and M. Tsypin. The Phase diagram of three-dimensional SU(3) + adjoint Higgs theory. *JHEP*, 11:011, 1998.

[121] C. T. H. Davies, K. Hornbostel, A. Langnau, G. P. Lepage, A. Lidsey, J. Shigemitsu, and J. H. Sloan. Precision Upsilon spectroscopy from nonrelativistic lattice QCD. *Phys. Rev.*, D50:6963–6977, 1994.

[122] G. P. Lepage, B. Clark, C. T. H. Davies, K. Hornbostel, P. B. Mackenzie, C. Morningstar, and H. Trottier. Constrained curve fitting. *Nucl. Phys. Proc. Suppl.*, 106:12–20, 2002.

[123] Peter Brockway Arnold and Olivier Espinosa. The Effective potential and first order phase transitions: Beyond leading-order. *Phys. Rev.*, D47:3546, 1993. [Erratum: Phys. Rev.D50,6662(1994)].

[124] Guy D. Moore and Niels Schlusser. Transverse momentum broadening from the lattice. *Phys. Rev. D*, 101(1):014505, 2020. [Erratum: Phys.Rev.D 101, 059903 (2020)].

[125] A. Hietanen, K. Kajantie, M. Laine, K. Rummukainen, and Y. Schroder. Three-dimensional physics and the pressure of hot QCD. *Phys. Rev.*, D79:045018, 2009.

[126] Alexei Bazavov et al. Meson Screening Masses in (2+1)-Flavor QCD. 2019.

[127] Dianne P. O'Leary and Bert W. Rust. Variable projection for nonlinear least squares problems. *Computational Optimization and Applications*, 54(3):579–593, Apr 2013.

[128] Michael J. Teper. SU(N) gauge theories in (2+1)-dimensions. *Phys. Rev.*, D59:014512, 1999.

[129] P. Giovannangeli. Two loop renormalization of the magnetic coupling in hot QCD. *Phys. Lett.*, B585:144–148, 2004.

[130] R. Baier, D. Schiff, and B. G. Zakharov. Energy loss in perturbative QCD. *Ann. Rev. Nucl. Part. Sci.*, 50:37–69, 2000.

[131] Jacopo Ghiglieri and HyungJoo Kim. Transverse momentum broadening and collinear radiation at NLO in the $\mathcal{N} = 4$ SYM plasma. *JHEP*, 12:049, 2018.

[132] E. Iancu, J. D. Madrigal, A. H. Mueller, G. Soyez, and D. N. Triantafyllopoulos. Resumming double logarithms in the QCD evolution of color dipoles. *Phys. Lett.*, B744:293–302, 2015.

[133] Simon Caron-Huot. When does the gluon reggeize? *JHEP*, 05:093, 2015.

[134] Simon Caron-Huot. Resummation of non-global logarithms and the BFKL equation. *JHEP*, 03:036, 2018.

[135] Simon Caron-Huot. On supersymmetry at finite temperature. *Phys. Rev. D*, 79:125002, 2009.

[136] K. Binder. Finite size scaling analysis of Ising model block distribution functions. *Z. Phys.*, B43:119–140, 1981.

[137] Peter Brockway Arnold and Guy D. Moore. Monte Carlo simulation of O(2) phi**4 field theory in three-dimensions. *Phys. Rev.*, E64:066113, 2001. [Erratum: Phys. Rev.E68,049902(2003)].

Acknowledgments

I gratefully acknowledge the support of many people during the making of my thesis.

First of all, I would like to thank my supervisor, Guy D. Moore, for him giving insights into his special way of thinking about physics, teaching me the essentials of the research business, recommending me for the Giersch excellence grant, supporting me in finding a postdoc position, providing his group with fun facts on Friday afternoons and making this research endeavor possible at all.

Related to that, I acknowledge support by the Deutsche Forschungsgemeinschaft (DFG, German Research Foundation) through the CRC-TR 211 'Strong-interaction matter under extreme conditions'– project number 315477589 – TRR 211." Numerical calculations for this research were conducted on the Lichtenberg high performance computer of the TU Darmstadt. Moreveover, I am grateful for membership in the Helmholtz-Graduate School for Hadron and Ion Research (HGS-HIRe).

Furthermore, I thank Jens Braun for being the second referee of the present thesis, and Tetyana Galatyuk and Benno Liebchen for being in the examination committee.

Olaf Kaczmarek from Bielefeld was an important part of my semester-wise PhD committee. He shed light on scientific and non-scientific problems from another perspective which I experienced as very enriching.

Furthermore, I would like to thank the members of the QCD group. Daniel Robaina for teaching me the armamentarium of lattice QCD and statistics, Parikshit Junnarkar for pointing out precious statistical tools, Vincent Klaer for proofreading, rowing workouts, and garbage-TV evenings, Thomas Jahn also for numerous conversations about garbage-TV-shows and for showing me the world of the lattice-conferences, Max Eller for being my doctoral twin, proofreading and advice about the analytical aspects of my research. Jillur Rahman, Marc Barroso and Marwin Acker complete the group and make it an enjoyable working environment. I appreciate Martin Steil having been my office mate

for three years, he knows about (almost) all odds and ends of Mathematica and other IT stuff. Together with his colleague Deniz Nitt and his supervisor Michael Buballa, they established a Mensa-fraction in the daily lunch break.

Moreover, in place of all my friends, I thank Sven Böhler, Werner Labarre, Simon Hillig, and Sebastian Knapp for their friendship, I have always highly valued their advice and seen them as a steady source of inspiration. I thank my rowing coach Helge Biehal for having taught me an important lesson early on in my life: “No pain, no gain.” I thank numerous people with whom I played together in various orchestras for sharing the passion of music with me, and my music teachers, Rahel Tittel and Tobias Mahl, for introducing me to this world.

I am deeply indebted to my girlfriend Eva Zirbel, for her love, for enriching my life with her personality and for hosting me during the later stages of the writing process of this thesis due to the quarantine measures of the Covid-19 pandemic.

Last but not least, I would like to thank my family. My grandmother Doris Schlusser for being my greatest defender, for having sympathy for the youth, and for trying to engage in new things although she does not like that, and my mother Solveig Schlusser for having raised me to where I stand now, for supporting me in being a physicist although what I do is alien to her, and for her life-experienced advice.

Curriculum Vitæ

Name:	Niels Vincent Lucca Schlusser
Date of Birth:	*26.01.1994
Place of Birth:	Mannheim

Education and employment

11/2017 - present	**Research associate** Technische Universität Darmstadt Institut für Kernphysik
11/2017 - present	**Doctoral studies in Physics** Technische Universität Darmstadt *"Momentum broadening of high-energy partons from 3D lattice EQCD simulations"*
10/2015 - 10/2017	**Master of Science in Physics (grade 1.2 – *very good*)** Ruprecht-Karls-Universität Heidelberg Master's thesis (supervised by Jürgen Berges): *"Towards the inclusion of quantum corrections into classical-statistical simulations"*
10/2012 - 09/2015	**Bachelor of Science in Physics (grade 1.4 – *very good*)** Ruprecht-Karls-Universität Heidelberg Bachelor's thesis (supervised by Jan Pawlowski): *"Hydrodynamische Modellierung des Quark-Gluon-Plasmas"*
09/2004 - 07/2012	**Abitur (grade 1.0 – *very good*)** Peter-Petersen-Gynmasium Mannheim
09/2000 - 07/2004	**Primary school** Alfred-Delp-Grundschule Mannheim

Scholarships, graduate schools, and grants

12/2017 - present	Participant in the Helmholtz Graduate School for Hadron and Ion Research
11/2019	Giersch Excellence Grant (2500€)
12/2012 - 09/2017	German Academic Scholarship Foundation ("Studienstiftung des Deutschen Volkes")

Publications

11/2019	Transverse momentum broadening from the lattice, *Phys. Rev. D 101, 014505 (2020)*.
11/2019	Full $\mathcal{O}(a)$ improvement of EQCD, *Proceedings of Science (2019)*.
05/2019	Full $\mathcal{O}(a)$ improvement in electrostatic QCD, *Phys. Rev. D 100, 034510 (2019)*.

Conference contributions and invited talks

05/2020	*Jet broadening from the lattice* Invited talk at the University of Helsinki
08/2019	*Full $\mathcal{O}(a)$-improvement of EQCD* Poster at the 37th Annual International Symposium on Lattice Field Theory

Miscellaneous

09/2019 - 03/2020	Member of *DFG – CRC-TR 211* retreat organization committee